

https://dspace.org/

Synthesis and characterization of cellulose nanofibre for electrically conductive paper

Ngobese, Sibonelo S.J.

2017

https://hdl.handle.net/10539/24963

Ngobese, Sibonelo Sibusiso Justin (2017) Synthesis and characterization of cellulose nanofiber for electrically conductive paper, University of the Witwatersrand, Johannesburg, <http://hdl.handle.net/10539/24963>

Downloaded from a DSpace repository. https://dspace.org/



Synthesis and characterization of cellulose nanofibre for electrically conductive paper

Prepared by

Sibonelo S.J. Ngobese (668458)

Submitted to

School of Chemical and Metallurgical Engineering,

Faculty of Engineering and the Built Environment, University of the Witwatersrand, Johannesburg, South Africa

Supervisors: Prof. Sunny Iyuke and Dr. Diakanua Nkazi

June, 2017

Declaration

I declare that this study is my own unaided work. It is being submitted in partial fulfilment of the requirements of Master of Science degree in Engineering to the University of the Witwatersrand. The report has not been submitted before for any degree or examination in any other University.



Signature of S.S.J. Ngobese

Date: 6th June 2017

ABSTRACT

There is huge drive to identify sustainable, renewable, and environmentally friendly raw materials and right technologies to make or use them. These technologies should be applied in place of the conventional non-sustainable and non-environmentally friendly currently used materials. Nanotechnology involves the use of materials that have at least one side with dimension 10^{-9} m. There is considerable effort directed at the much abundant forest product such as cellulose which can be processed into cellulose nanofibrillated fibres (CNF) and cellulose nanocrystals (CNC). This study involved the synthesis and testing of an electrical conductive cellulose nanofibre made from microcrystalline eucalyptus grandis pulp. In this project, microcrystalline cellulose (MFC) from wood pulp was mechanically fibrillated using a Pilot Refiner to develop microfibrils. The microfibrilated pulp was oxidised with a mixture of 2,2,6,6-tetramethylpyradine-1-oxyl (TEMPO), sodium bromide (NaBr) and sodium hypochlorite (NaOCl) to produce CNF . The CNF was washed, sonicated and dried to produce translucent sheets. The oxidation process was able to achieve both CNF and CNC from wood pulp which was verified and characterized by Techpap, SEM, TEM, FTIR, Hounsfield Tensile Tester and Multimeter. The Techpap instrument indicated that the starting raw unfibrilated and mechanical fibrillated pulp fibre widths were 3.18 and 3.07 microns respectively. After oxidation process the FTIR Spectra produced an absorbance peak at approximately 1720 to 1740 cm^{-1} wavenumbers that is characteristic of the aldehyde carbonyl stretch which was not present on the unoxidised pulp. The average tensile strength of the paper strips were determined to be 4.51kN/m using the standard procedure of the experiment. From the TEM images it was observed that the CNF and CNC had dimensions ranging from 1.4nm to 594nm from pulp. The SEM images showed that on drying the CNF and CNC repolymerised into nanogel. The resistivity of the control CNF was in the infinity range. When the CNF was treated with the reduced Graphene Oxide (GO), the resistivity was determined to be 4400 Ω.m. This resistivity translates to an electrical conductivity of 2.27×10^{-4} $\Omega^{-1}.m^{-1}$ for a length of a paper strip that was 5mm long. The conductivity of the CNF material was significantly improved and fell within the range of semi-conductive materials. The overall research showed that the synthesized

cellulose nanofibre hold a semi-conductor behavior, which add value information in the explored research area.

ACKNOWLEDGEMENTS

The author would like to thank the leadership of the company; Dr Charlie Clarke (General Manager of the Technology Centre, Pretoria), and Brendon Palmer (Fibre Processing Manager) of the South African Pulp and Paper Industries (Sappi), Southern African Region for sponsoring the Research Project, funding of the tuition fees, and their support with raw materials and the use of their laboratory facilities and advanced equipment.

I also would like to thank the Academic Staff of the School of Chemical and Metallurgical Engineering at the University of Witwatersrand, Johannesburg especially the Project Supervisors, Professor S. Iyuke and Dr D. Nkazi for their guidance and allowing for the use of the institutional facilities, materials and advanced instrumentation. I would like to thank Dr Mercy Shuma-Iwisi from the Department of Electrical Engineering for her support and guidance especially with electrical resistance measurements. I would like to thank many individuals who contributed immensely with their time, support and knowledge especially Dr Sanet Minnaar, Cyprian Ngubane, Sabatha Maduna, Bonisile Mokoena, Lloyd Mudau, Ronnie Bothma, Rene Grant, Tumi Twala, Stephen Swart, Sibusiso Makhonjwa, Mathew Khumalo, Zininzi Monki, and Nomvula Maduna, and my sister Purity Mzotho for her contributions.

I would not forget my Dad Jaconiah Ngobese and my brothers and sisters with their wonderful spirit of encouragement that they have shown during execution of this project.

Finally, I would like to thank my family; my wife Thembi, my daughter Mbali and my son Dumo for allowing me to take most of their time while I was doing the research work after normal working hours.

S.S.J. Ngobese

TABLE OF CONTENTS

	PAGE
Declaration	i
Abstract	ii
Acknowledgements	iii
Table of Contents	iv
List of Figures	viii
List of tables	xiii
List of Abbreviations	xiv
Chapter 1: Background and motivation	**1**
1.1 Problem statement	2
1.2 Research objectives	2
1.3 Expected research outcomes and contributions	3
1.4 Significance of research project	3
Chapter 2: Literature review	**5**
2.1 Natural fibres	5
2.1.1 Introduction	5
2.1.2 Lignin	7
2.1.3 Hemicellulose	8
2.1.4 Cellulose	9

2.2: Chemical treatment of cellulose 10

2.2.1: Acid Hydrolysis 17

2.2.2: Alkaline hydrolysis 17

2.2.3: Oxidation agent 18

2.2.4: Organosolv 18

2.2.5: Ionic liquids 19

2.3: Native cellulose 19

2.3.1: Preparation of nanocellulose 20

2.4: Conductive polymers 21

2.4.1: Measuring resistance and resistivity of materials 23

2.4.2: Applications of conductive polymers 25

2.4.3: Graphene 27

2.4.4: Graphene oxide (GO) and reduced graphene oxide (rGO) 28

Chapter 3: Experimental procedures and analysis techniques 30

3.1 Raw materials and characterisation instruments 30

3.2 Synthesis of microfibrilated cellulose (MFC) 31

3.3 Synthesis of CNF and [CNF/Cu2+/rGO]n 31

3.4 Process flow diagrams of Pilot Refiner 32

3.5 Analytical techniques 35

3.5.1 Morphological Fibre Wall Thickness Analysis (Morfi MWT) 35

3.5.2 Scanning electron microscope (SEM) 37

3.5.3 Transmission electron microscope (TEM) 38

3.5.4 Fourier Transform Infrared (FTIR) Spectroscopy 39

3.5.5 Hounsfield Tensile Tester 40

Chapter 4: Results and discussion **43**

4.1 Characterisation of unrefined and refined pulp with Morfi MWT 43

4.2 Characterisation of un-oxidised cellulose pulp with SEM 45

4.3 SEM image of TEMPO-oxidised cellulose 47

4.4 Topographical image of oxidised CNF 51

4.5 Characterization of oxidized cellulose using TEM 52

4.6 Characterization of CNF using FTIR 55

4.7 Characterisation of the CNF with tensile tester 57

4.7.1 Statistical analysis of CNF tensiles with different NaOCl concentrations 58

4.7.2 Discussion of the results of varied NaOCl concentration 59

4.7.3 Discussion of the results of varied NaBr concentration 60

4.7.4 Electrical resistance tests of oxidized CNF and rGO paper 63

Chapter 5: Conclusions and recommendations **66**

5.1 Conclusions **66**

5.2 Recommendations **68**

References **69**

Appendix **73**

Appendix A: Tables **73**

Appendix B: Figures **82**

LIST OF FIGURES

FIGURE	PAGE
Figure 2.1: Structural components of lignocellulose biomass	6
Figure 2.2: Dominating structures in lignin	7
Figure 2.3:Chemical structures in hemicellulose	8
Figure 2.4: Chemical structures in cellulose	9
Figure 2.5: E*ucalyptus grandis* plant a source of celluloce fibre	11
Figure 2.6: SEM of cell walls in wood matrix	12
Figure 2.7: Internal hierarchy of wood structure	13
Figure 2.8: Deconstruction of lignocellulose	15
Figure 2.9: Strategy for lignocellulosic biomass fractionation	16
Figure 210: Nanocellulose synthesis process	21
Figure 2.11: Diagram of electrical circuit showing V, I and R	23
Figure 2.12:Diagram showing principle of resistance measurement	23
Figure 2.13: Mechanism of exfoliation of graphene flakes	28
Figure 2.14:Reduction mechanism of GO	29
Figure 3.1: Photograph of the Pilot refiner	33
Figure 3.2: Process flow diagram of the Pilot refiner	34
Figure 3.3: Rotor and stator disks of the Pilot refiner	35
Figure 3.4: Diagram illustrating the KEY components of Morfi MWT	36
Figure 3.5: Techpap instrument for measuring MWT	36

Figure 3.6: KEY components of SEM instrument 37

Figure 3.7: KEY components of TEM instrument 38

Figure 3.8: Schematic diagram of FTIR Spectroscopy 39

Figure 3.9: Hounsfield instrument for tensile strength 41

Figure 4.1: Graph showing MWT distribution of unrefined *E. grandis* . pulp 44

Figure 4.2: Graph showing MWT distribution of refined *E. grandis* pulp 44

Figure 4.3: SEM image of unrefined *E. grandis* pulp 46

Figure 4.4: SEM image of mechanically refined *E. grandis* pulp 47

Figure 4.5: SEM image of gelled TEMPO-oxidised CNF 48

Figure 4.6: SEM image showing the multilayers of the dried CNF 49

Figure 4.7: High resolution SEM image of single TEMPO-oxidised CNFfibre 50

Figure 4.8: Topographical image of the dried TEMPO-oxidised CNF 51

Figure 4.9: TEM image of the polymerising TEMPO-oxidised CNF 53

Figure 4.10: Aggregating “cloud” of CNF 54

Figure 4.11: FTIR spectrum of the unoxidised cellulose 56

Figure 4.12: FTIR spectrum of the oxidised cellulose for six hours 56

Figure 4.13: FTIR spectrum of the cellulose with NaOCl concentration halved 56

Figure 4.14: FTIR spectrum of the cellulose with NaBr halved 56

Figure 4.15: FTIR spectrum of the cellulose with NaOCl concentration doubled 56

Figure 4.16: FTIR spectrum of the cellulose with NaBr concentration doubled 56

Figure 4.17: Comparisons of CNF tensile with varied NaOCl concentration 58

Figure 4.18: Interval plot of CNF tensile with varied NaOCl concentration 58

Figure 4.19: SEM image of CNF produced from doubled NaOCl concentration 60

Figure 4.20: SEM image of CNF produced from halved NaOCl concentration 60

Figure 4.21: Comparisons of the CNF tensile strength with varied NaBr 61

Figure 4.22: Interval plot of CNF tensile strengths with varied NaBr concentration 62

Figure 4.23: SEM image of CNF produced from doubled NaBr concentration 62

Figure 4.24: SEM image of CNF produced from halved NaBr concentration 62

Figure 4.25: Dried sheet of TEMPO-oxidised CNF 63

Figure 4.26: Dried sheet of TEMPO-oxidised CNF treated with rGO 63

Figure 4.27: Graph of the resistivity against strip length 65

Figure B.1 : FTIR Spectra of normal NaBr concentration 82

Figure B.2 FTIR Spectra of normal NaBr concentration 82

Figure B.3 FTIR Spectra of normal NaBr concentration 83

Figure B.4: FTIR Spectra of doubled NaBr concentration 84

Figures B.5: FTIR Spectra of doubled NaBr concentration 84

Figures B.6: FTIR Spectra of doubled NaBr concentration 85

Figures B.7: FTIR Spectra of halved NaBr concentration 86

Figures B.8: FTIR Spectra of halved NaBr concentration 86

Figures B.9: FTIR Spectra of halved NaBr concentration 87

Figures B.10: FTIR Spectra of doubled NaOCl concentration 88

Figures B.11 FTIR Spectra of doubled NaOCl concentration 88

Figures B.12: : FTIR Spectra of doubled NaOCl concentration 89

Figures B.13 TIR Spectra of halved NaOCl concentration 90

Figures B.14 TIR Spectra of halved NaOCl concentration 90

Figures B.15 TIR8 Spectra of halved NaOCl concentration 91

Figures B.16: Minitab Statistical Objective 92

Figure B.17: Minitab Statistical Test – One-Way ANOVA 93

Figure B.18 Probability test for doubled NaOCl concentration 94

Figure B.19: Probability test for normal NaOCl concentration 94

Figure B.20: Probability test for halved NaOCl concentration 95

Figure B.21: Probability test for normal NaBr concentration 95

Figure B.22: Probability test for doubled NaBr concentration 96

Figure B.23: Probability test for halved NaBr concentration 96

Figure B.24: SEM image of doubled NaOCl resolution 820x 97

FigureB.25: SEM image of doubled NaOCl resolution 320x 97

Figure B.26: SEM image of halved NaOCl resolution 820x 98

Figure B.27: SEM image of halved NaOCl resolution 265x 98

Figure B.28: SEM image of doubled NaBr resolution 790x 99

Figure B.29: SEM image of doubled NaBr resolution 300x 99

Figure B.30: SEM image of halved NaBr resolution 790x 100

Figure B.31: SEM image of halved NaBr resolution 295x 100

LIST OF TABLES

TABLE	PAGE
Table 3.1: Process variables of pilot refiner	33
Table 3.2: Concentrations of NaOCl and NaBr used to produce different CNF	40
Table 4.1: Tensile strengths results of different CNF samples	57
Table 4.2: Electrical resistance measurements of TEMPO-oxidised paper	64
Table 4.3: Electrical resistance measurements of the [CNF/Cu^{2+}/rGO]n paper	64
Table A.1: Percentage distribution of cellulose MWT of unrefined pulp	73
Table A.2: Percentage distribution of cellulose MWT of refined pulp	73
Table A.3: MWT data of the unrefined *E.grandis* pulp	74
Table A.4: MWT data of the refined *E.grandis* pulp	75
Table A.5: Tensile strength data of the halved NaOCl concentration	76
Table A.6: Tensile strength data of the doubled NaOCl concentration	77
Table A.7: Tensile strength data of the normal NaOCl concentration	78
Table A.8: Tensile strength data of the doubled NaBr concentration	79
Table A.9: Tensile strength data of the halved NaBr concentration	80
Table A.10: Tensile strength data of the normal NaBr concentration	81

LIST OF ABBREVIATIONS

TEMPO	2,2,6,6-Tetramethylpyradine-1-oxyl
CNF	Cellulose nanofibrillated fibres
MCC	Microcrystalline cellulose
SEM	Scanning Electron Microscopy
TEM	Transmission Electron Microscopy
FTIR	Fourier Transform Infra-Red Spectroscopy
GO	Graphene Oxide
rGO	Reduced Graphene Oxide
PEDOT	Polyethylene dioxythiophene
CTE	Coefficient of thermal expansion
MFC	Microfibrilated cellulose
ITO	Indium tin oxide
AZO	Aluminium doped zinc oxide
PC	Polycarbonate
LBL	Layer-By-Layer
PANI	Polyaniline
Ppy	Polypyrrole
ECP	Electron conductive polymer
PSS	Polystyrene sulphonic acid

Chapter 1: Background and motivation

The production of the new evolving photovoltaic cell appliances and electronic gadgets needs a diverse and fresh innovative approach (Valentini et al., 2014). The great problem to solve is about the economic sustainability of the current substrates used in electrical circuits. There is a great prospect for the utilization of flexible transparent conductive films in areas such as electronics, clothing, sensors, electrodes, and solar energy harvesting panels and related technologies (Gao et al., 2013). These films are prepared from nanoparticle materials such as certain metal oxides, cellulose nanofabricated fibres (CNF) and organic conductive molecules. With an increasing demand for greener products especially from the environmental lobby groups, manufacturing of such products from ecofriendly renewable sources such as cellulose may earn them a place in the electronic device industry (Gao et al., 2013). Cellulose nanofibres have been recently identified as worthwhile nanoparticles that are obtained from an abundant bio-renewable source such as plants (Zhou et al., 2013). From the abundance, renewability, recyclability, sustainability and environmental acceptability attributes, it is possible to reach the economies of scale with nanocellulose fibres (Zhou et al., 2013). However, native cellulose is non-electrically conductive by nature because of the sp^3-hybridized carbon centres. It is therefore, ideal to be used as substrates and borrow the electrical conductivity from other conductive nanoparticles. Preparing the conductive organic material based on polymers imposes some challenges as most organic compounds have a very low electrical flow and generally, are insulators. To render them conductive the organic polymer has to possess sp^2 hybridized carbon centres, i.e. conjugated double bonds and further be doped (nobbled) with either oxidizing or reducing agents to enhance electrical mobility (MacDiarmid and Heeger, 1980). This project aims to research the suitability of *eucalyptus grandis* microcrystalline cellulose (MCC) fibre produced from a magnesium acid sulphite process to prepare an optical transparent cellulose substrate that will be developed into an electrical conductive paper. The subsequent literature survey explores the chemistry

and physics needed to successfully develop the electrical conductive paper based on organic nanoparticles.

1.1 Problem statement

Recently natural organic polymers have found many applications in various fields of science including medicine and electronics. They have generated more interest to scientists because they offer processing flexibility and are renewable. The conventional semiconductors will remain important, however, the production costs are high and the future of these materials seem unsustainable (Pandey et al., 2012). The biopolymer-electronic-based products will offer products at competitive costs compared to the current metal and semiconductor based substrates used in the field of electronic engineering. The success of this project would lead to the optimization of the product processing and this research project forms the basis of the future development of the scalable electrical conductive paper.

1.2 Research aim and objectives

The aim of this research involves the synthesis of an electrical conductive cellulose nanofibre. This is achieved through the following objectives:

- To process microcrystalline *eucalyptus grandis* (*E.grandis*) pulp into cellulose nanofibre (CNF)
- To prepare the transparent films from the CNF
- To characterize the following properties of CNF; morphology, topographical image, transversal image and developed carbonyl groups, and measurement of the tensile strength of the CNF transparent films using Morfi Fibre Wall Thickness (MFWT), Scanning Electron Microscopy (SEM), Scanning Electron Microscopy (TEM), Fourier Transform Infra-Red Spectroscopy (FTIR) and Hounsfield Tensile Tester

- To prepare the CNF transparent electrical conductive films by coating it with Graphene Oxide solution
- To test the resistance of CNF substrate/Graphene Oxide using an Ohmic Tester

1.3 Expected research outcomes and contributions

The expected outcomes of this research project are as follows:

i) The successful processing of the microcrystalline E*. grandis* into CNF and the CNF nanoparticle confirmed with TEM analysis.
ii) The successful preparation of the transparent films from the CNF gel and the characterization of the surface using the SEM instrument.
iii) The successful characterization of the samples with the FTIR technique that indicates the oxidation of primary alcohol, which leads to the separation of adjacent polymer chains.
iv) The successful reduction of the resistivity of the CNF when coated with grapheme oxide, which confirms the improvement of electrical conductivity of the CNF film.
v) A research project report and journal paper that show the understanding and application of the theory on the subject matter.

1.4 Significance of the research project

Currently, the conductive polymers have not yet achieved the required economies of scale. Some challenges to overcome that are faced with constraints imposed by manufacturing costs, toxicity, and solubility issues. They also do not perform well during melt processes. Further developments of these materials will eventually enable them to find applications in electronic fields such as organic solar cells, printing electronic circuits, organic light-emitting diodes, actuators, electrochromism, supercapacitors,

chemical sensors and biosensors (Lange, 2008). The progress has been made to develop the nanostructured kinds of conducting polymers in order to produce polymers with higher surface area and better dispersability. Lately, materials such as poly-3,4-ethylenedioxythiophene (PEDOT) and polyaniline (PANI) which are conducting films have gained some large scale applications. While PEDOT is mainly used in antistatic applications with polyststyrene sulphonic (PSS) acid and as a transparent conductive layer in the form PEDOT: PSS dispersions. This research will contribute to the understanding of the science and engineering of the products based on conductive organic polymers especially in the field of Chemical and Electronic Engineering. The important contributions would be to improve the processing methods by closing the gaps that may have been omitted by the previous researchers. The outputs from this research are to identify and develop a unique product at the next level of study and launch it to the market.

Chapter 2: Literature Review

2.1 Natural fibres

2.1.1 Introduction

Fibres are categorized in two broad classes namely; natural and synthetic fibres. The natural fibres are further subdivided according to their sources, which could be plants (lignocellulosic biomass), animals or mineral origin (Salajkova, 2009). Synthetic fibres are produced by chemical process and materials involved are generally used to derive their nomenclature. Lignocellulosic biomass is a natural compound that consists of three major elements namely lignin, cellulose and hemicellulose (Lee et al., 2014). This project is focused on natural fibres produced from woody plants. All plant fibres share common repetitive disaccharide unit called cellobiose, which falls under a class of sugars broadly called carbohydrates. The cellobiose is simply a dimer of two glucose molecules that are joined by a β (1-4) glucopyranose. Fibres obtained from plants are either from bast, leaves, seeds, fruits, wood, cereals straw and certain grasses. Polymerised carbohydrates give rise to chains that when stacked together form cellulose fibrils.

The manufacturing process is the function of ingenuity that partly could be attributed to enzymes. They are found to constitute straight carbohydrate polymer chains or helical web throughout the plant structure depending on whether the dominating structure is alpha (α) and or beta (β) (Salajkova, 2009). The self-adhesion tendency characteristics of cellulose material has been identified many years ago (Gardner et al., 2008). The simplicity by which the adhesion occurs in cellulose has rendered it as a useful material in papermaking and several composite materials. Schools of thought concerning surface adhesion phenomena of fibres have been investigated and summarised as being caused by mechanical fibre interlock, surface adsorption process, diffusion and weak chemical, and physical forces (i.e. hydrogen bonding and van der Waals forces). It

has been found that by careful fractionating major components of lignocellulosic biomass, the yields are fractions of high value compounds. These compounds could be used as intermediates or precursors for green biofuels (e.g. ethanol), natural sugars (e.g. pentose's, hexoses) and cellulose with a potential of many applications including medicinal fields, food industry, chemical, electronic engineering, polymer composites, textile fibre manufacturing, bio composites and inorganic composites, etc. The lignocellulosic biomass is composed in such a manner that the core crystalline cellulose is glued together by chemical impermeable lignin that is hydrophobic, and anti-bacterial that act as barrier against microbial attack (Lee et al., 2014). There is second layer of porous hemicellulose consisting of organic sugars in which its pores are filled with lignin as shown (figure 2.1).

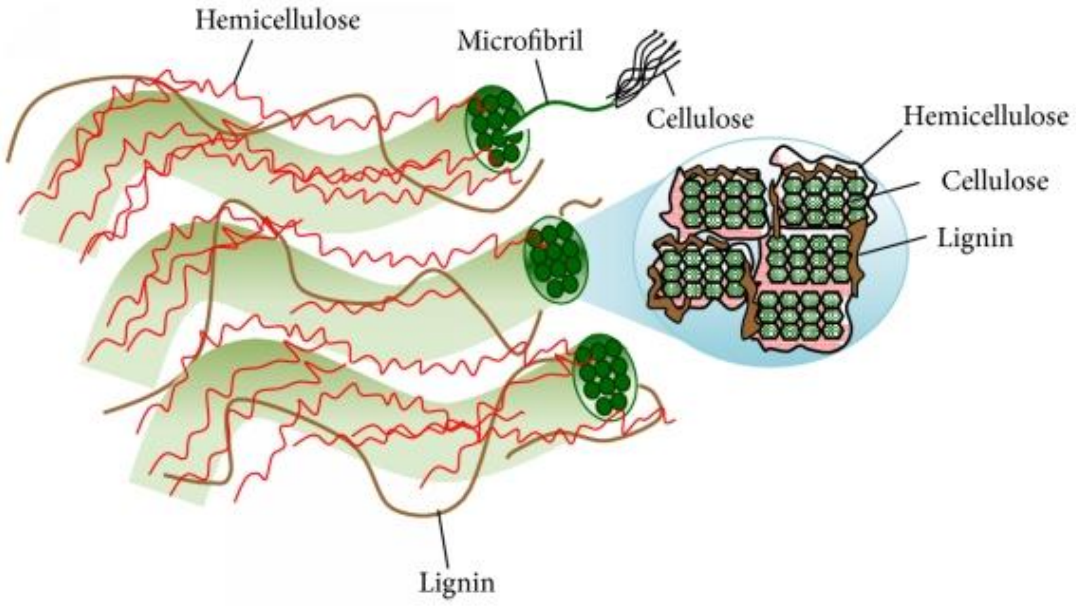


Figure 2.1: Structural components of lignocellolosic biomass (Lee et al., 2014)

The complex structure of lignocellulosic biomass possesses certain characteristics such as slight accessibility by chemical additives and ordered crystalline cellulose. The lignocellulosic biomass structural construction presents both difficulties and

opportunities for high value bio chemical recovery and extraction of pure cellulose for nanocellulose processing (Chundawatt et al., 2013). Retrosynthetic pathways reveal major molecules responsible for the structures of lignin, hemicellulose, and cellulose .that could be exploited for separation of lignocellulosic biomass (Agbor et al., 2011).

2.1.2 Lignin

The composition of lignin was analysed and found to consists of three cross-linked polymers of phenolic monomers especially p-coumaryl alcohol, coniferyl alcohol, and sinapyl alcohol (Figure 2.2). In general the plants with longer and soft fibre such pine woods contain higher quantities of lignin compared to other types of biomass. The long fibre plants are resilient to lignin extraction during the lignonocellulosic biomass separation (Grabber, 2003).

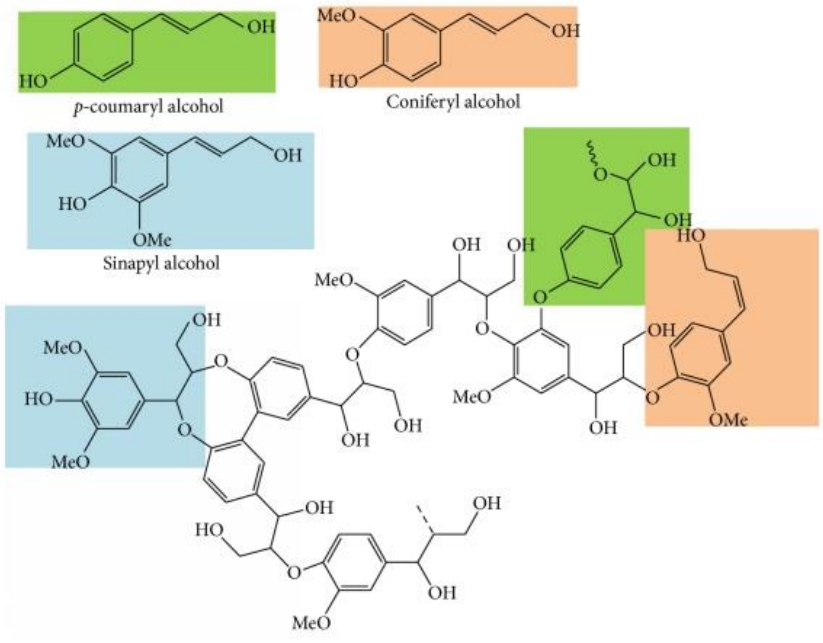


Figure 2.2: Dominating structures in lignin (Lee et al., 2014)

2.1.3 Hemicellulose

Hemicellulose similar to lignin also hinder the exposure of cellulose fibrils to be affected by solubilising chemicals during lignocellulosic biomass deconstruction. The cellulose is covered with tiny horizontal branches of hemicellulose. The molecular composition of hemicellulose was found to be consisting of different sugars such as pentoses, hexoses, and acetylated sugars, etc. (Figure 2.3). In order to effectively digest cellulose for nanocellulose production, it is recommended that at least 50% of hemicellulose should be extracted (Agbor et al., 2011). Hemicellulose can be simply hydrolysed by diluted acid, alkali, or enzymes under mild conditions, however, hemicellulose is .highly sensitive to heat. Under uncontrollable conditions it can easily decompose to produce unwanted products such as furfurals and hydroxymethyl-furfurals that hinder the fermentation process for bioethanol processing.

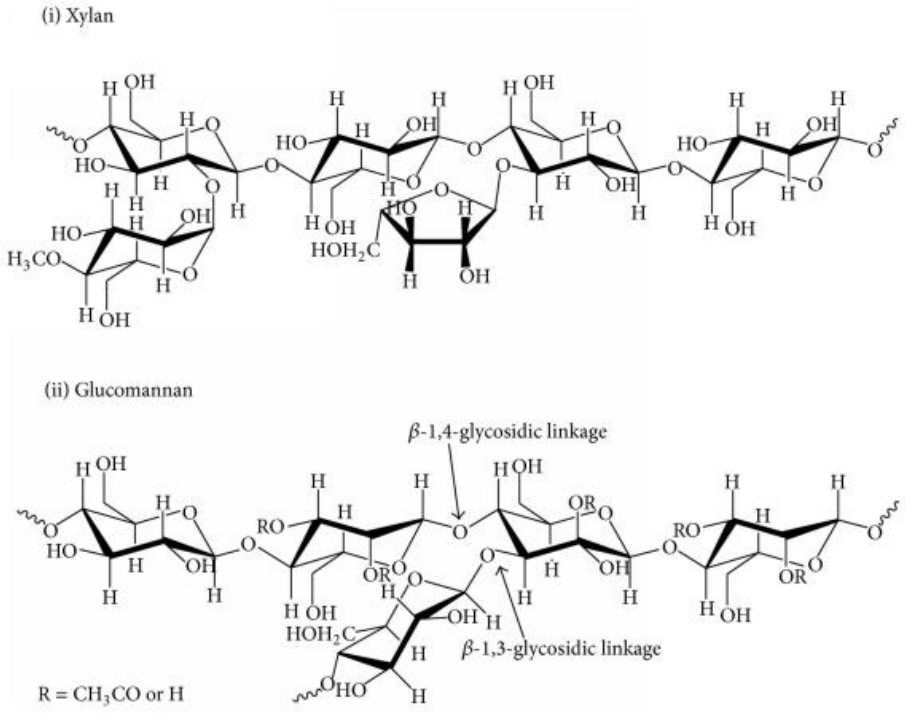


Figure 2.3: Chemical structure in hemicellulose (Lee et al., 2014)

2.1.4 Cellulose

Cellulose exists in plant domain in two forms i.e. crystalline and amorphous forms. The crystalline form of the polymer chains consist of regions with more ordered chains. In amorphous form the polymer chains consist of regions which are disorderly arranged and less dense fibrous structure. Since disordered amorphous regions are less dense, they are not resistant as crystalline regions against chemical hydrolysis during deconstruction of biomass. The amorphous cellulose is attacked and ruptured during chemical hydrolysis and cellulose swelling. Linear crystalline cellulose polymers are chemically bonded together by inter- and intramolecular bonds from adjacent oxygen's and hydrogens of the same polymer chains or from neighbouring chains. This allow them to be packed side by side in planar sheets formation and bundled into microfibrils (Figure 2.4). Strong hydrogen bonds and van Waals forces render cellulose insoluble in water. Extensive bonding effect presents another hydrolysis task for nanocellulose synthesis (Khalil et al 2012). In essence, only the cellulosic fibres that are on the surface of the microfibril that are exposed to solvents, oxidants, and chemicals agents can be hydrolysed.

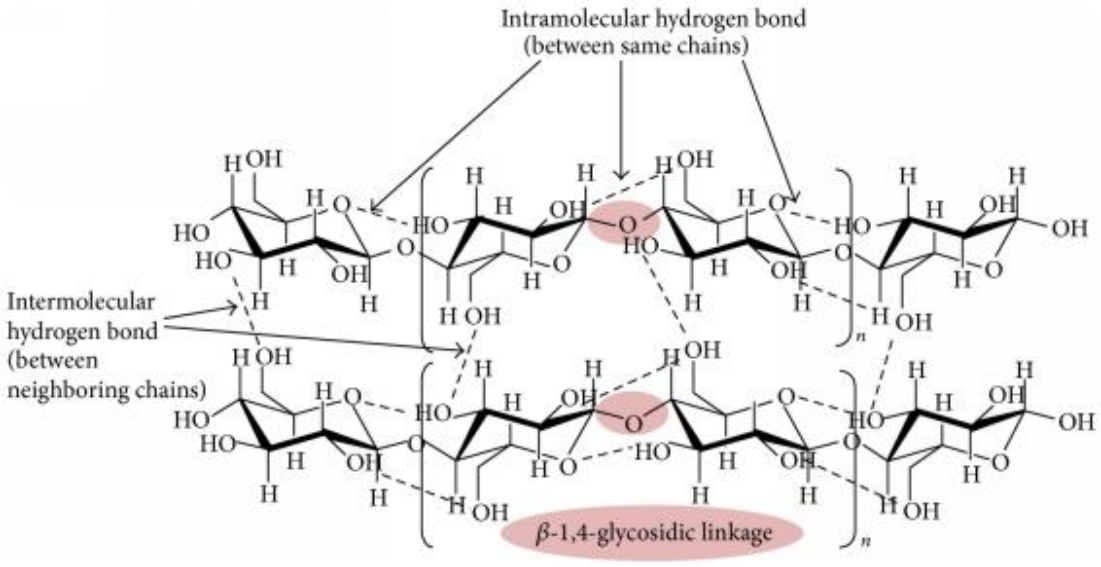


Figure 2.4: Chemical structures in cellulose chains (Lee et al., 2014).

Cellulose is a widely available natural material that is obtained from plants and grass estimated to constitute about 40% of ligno-cellulosic biomass (Wang et al., 2012). Because of its strength properties and versatility, it is useful in the manufacturing of many other materials. The cellulosic fibre is naturally produced as a dimensionally thin and long tubular material (within the size range from a few nm in diameter to several mm in length. However this is dependent on the type of species that is being investigated and the geographic location (Saito et al., 2006). The process by which the fibres are formed is naturally controlled and very specific in terms of distribution network direction. The accuracy of the placement of the molecules and the repetitive development of the succeeding layers in the body yields a very high degree of crystallinity. The well-organized structure of a plant has earned itself a position that is being researched for many usages because of its physical and versatile properties (Saito et al., 2006). It is estimated that the yearly production of cellulose is over 7.5×10^{10} tons (Lindström et al., 2014). Cellulose is made up of monomers that are arranged in a linear fashion to form polysaccharides irrespective of the original parent source. These monomers generally form a repeating d-glucopyranose dimer that repeats itself across the chain in a 1,4 linkage (Brinchi et al., 2013). It has been recognized that the cellulose as a material has a tremendous strength and has the ability to manufacture materials of great performance (Wegner and Jones, 2009).

Pine and spruce are common wood cellulosic pulps that are characterized as long fibres, whereas, eucalyptus, beeches, oak, etc. is wood pulps characterized as short fibres. There are other several fibre sources such as grass (bagasse), cotton, kenaf, etc. Figure 2.5 shows photographs of different parts of *eucalyptus grandis* (*E. grandis*) which is one of the eucalyptus species that is used as a source of cellulose fibre. *Eucalyptus* is found in a wide variety of flowering plant species that belong to the myrtle family. They form a wide part of trees among the vegetation of Australia. Eucalyptus consists of more than 800 species that are abundant in Australia. Very few species are available in the surroundings areas such as in New Guinea and Indonesia. *Eucalyptus* is the most common short fibre source of pulp and paper. A handful of species has been

adopted in South Africa and they are used for the manufacturing of timber, pulp, firewood and also for ornamental articles. Separating cellulose into its elemental form is a difficult task; however mechanical, chemical and biotechnological methods have (Shinichiro et al., 2008) been previously employed to produce cellulose nanofibres (CNFs) (Shinichiro, Kentaro, & Hiroyuki, 2008). Figure 2.6 shows the bundles of cell walls in wood matrix bound together by lignin.



Figure 2.5: E*ucalyptus grandis* plant a source of celluloce fibre (Immelman et al., 2015)

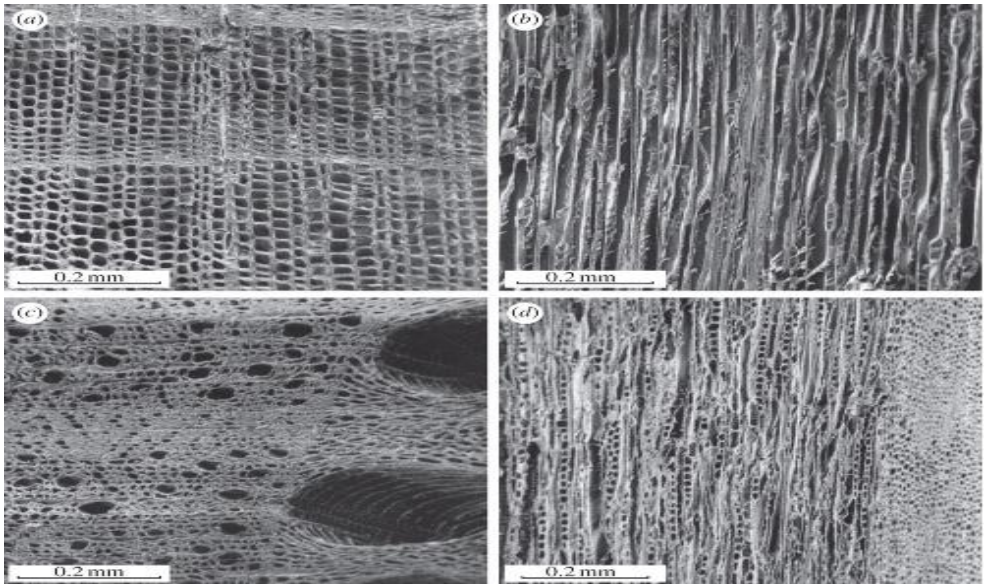


Figure 2.6: SEM of cell walls in wood matrix: (a) cedar cross section; (b) cedar longitudinal section; (c) oak cross section; (d) oak longitudinal section (Gibson, 2012)

Cellulose fibres in the papermaking industry are separated from the wood matrix by a process called pulping. The main common pulping processes are: (1) chemical pulping where the lignin holding the cellulose fibres together is chemically removed from the wood matrix under high temperature and pressure, and (2) mechanical pulping which uses mechanical frictional forces such as grinding stones and metal disks refiners to free the individual fibres. Chemical pulping is the most common process producing pulps with relatively high strengths. The process involves cooking small sized wood chips (4 – 6 mm in thickness) using strong chemicals at high temperatures and high pressures to release individual fibres from wood matrix. Figure 2.7 indicates the hierarchical development of wood structures.

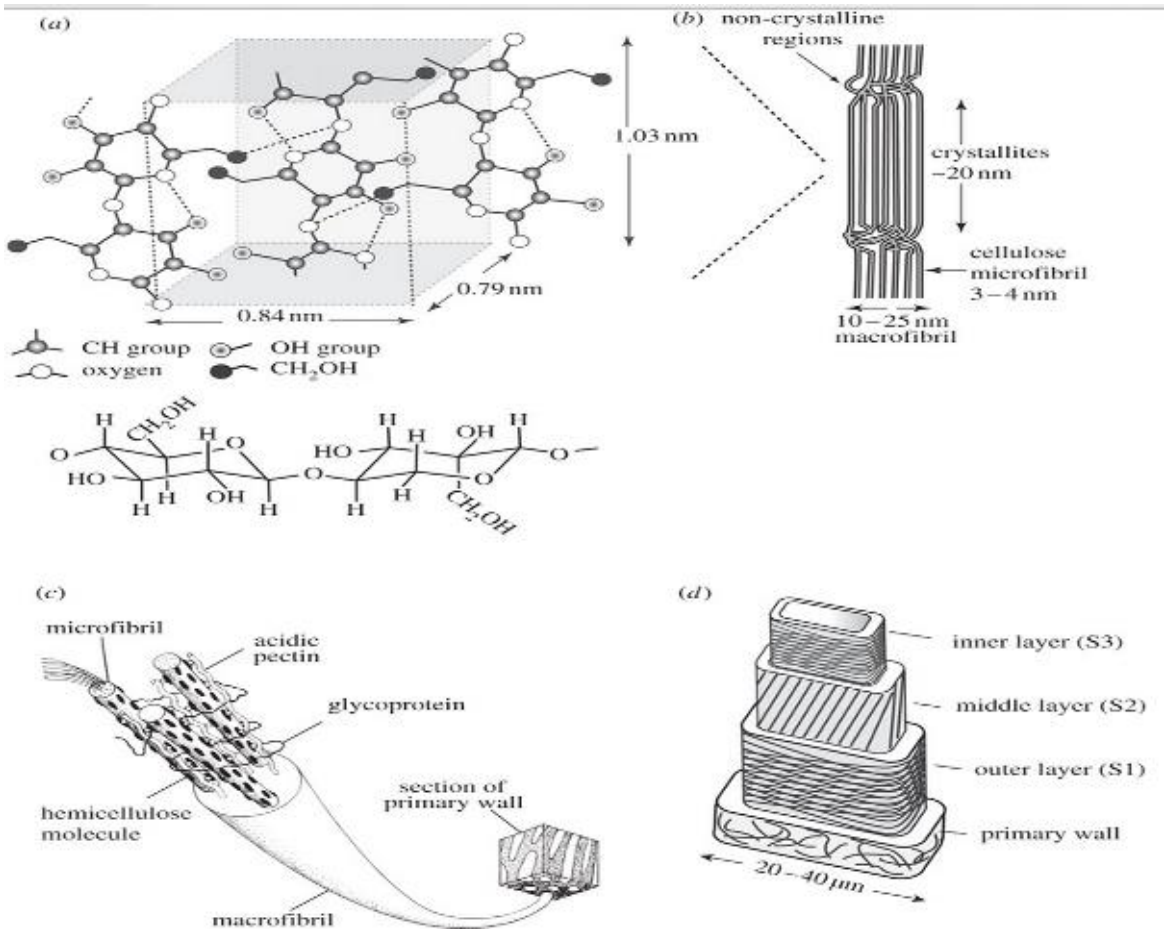


Figure 2.7: Internal hierarchy of wood structure (a) glucose molecules (b) microfibrils (c) macrofibrils and (d) wood cell wall made up of layers (S1, S2 and S3) (Gibson, 2012)

Because cellulose is readily available and renewable it has been sighted as the carbon feedstock resource.

2.2 Chemical treatment of cellulose

The methods required to digest plant cell walls into higher value products such as cellulose, hemicellulose, and lignin for different applications are hindered by response of the components to different chemicals during separation of lignocellulosic biomass. The method should consider the following points:

(i) Prevent structural disruption that would lead to the loss of cellulose, hemicellulose, and lignin contend ring fractionation;
(ii) To fractionate cost-effectively and reduce energy input; and
(iii) Reduce generation of toxic and hazardous wastes.

The purpose of biomass pretreatment is to dissolve lignocellulosic structure in such a way as to solubilise the noncellulosic materials and (hemicellulose and lignin) but secure cellulose material. In the process the cellulose crystallinity is reduced, and become porous (Karimi et al., 2013) (Figure 2.8). The current chemical pretreatment procedures that are employed to digest lignocellulosic biomass are listed below;

(i) Acid hydrolysis,
(ii) Alkaline hydrolysis,
(iii) Oxidation agents,
(iv) Organosolv, and
(v) Ionic liquids.

Each chemical pretreatment can be strategically employed to dissolve specific functional groups in biomass, for example, mild acid hydrolysis will solubilise hemicellulose and alkaline hydrolysis will dissolve lignin. Oxidising agents will degrade react cellulose under specific conditions. It is important that solubilised components can be easily recovered from particular chemical pretr4atment. The model of lignocellulosic biomass deconstruction is shown (figure 2.8).

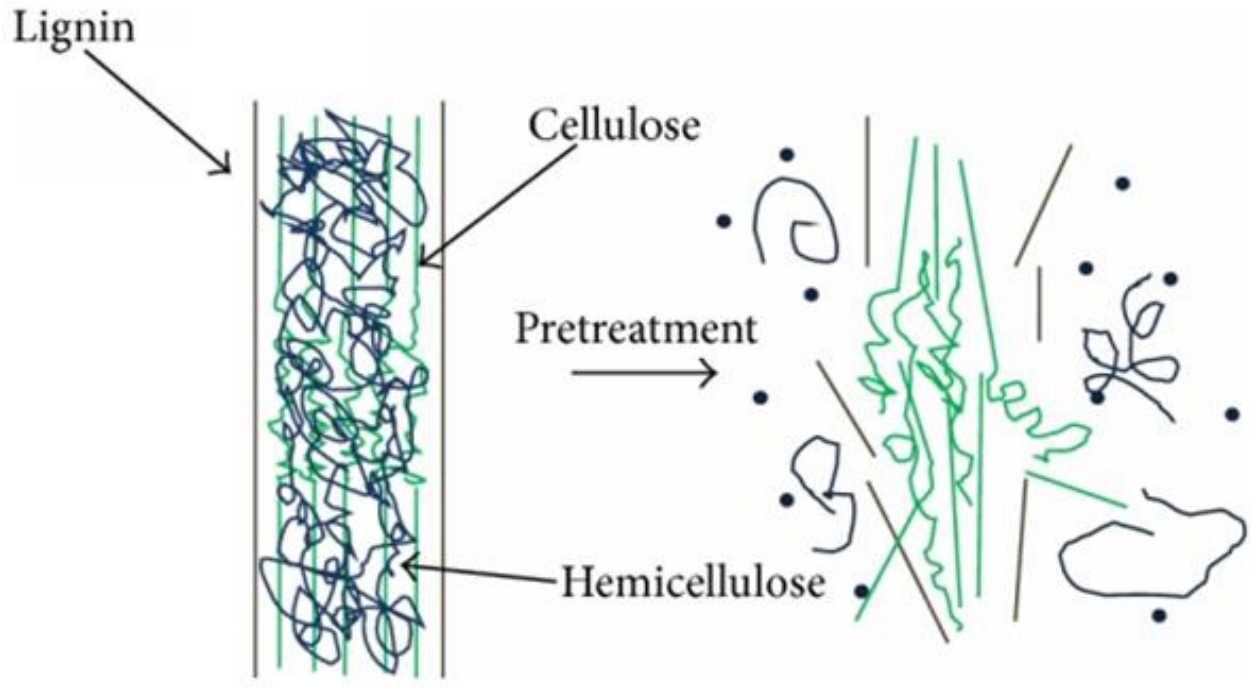
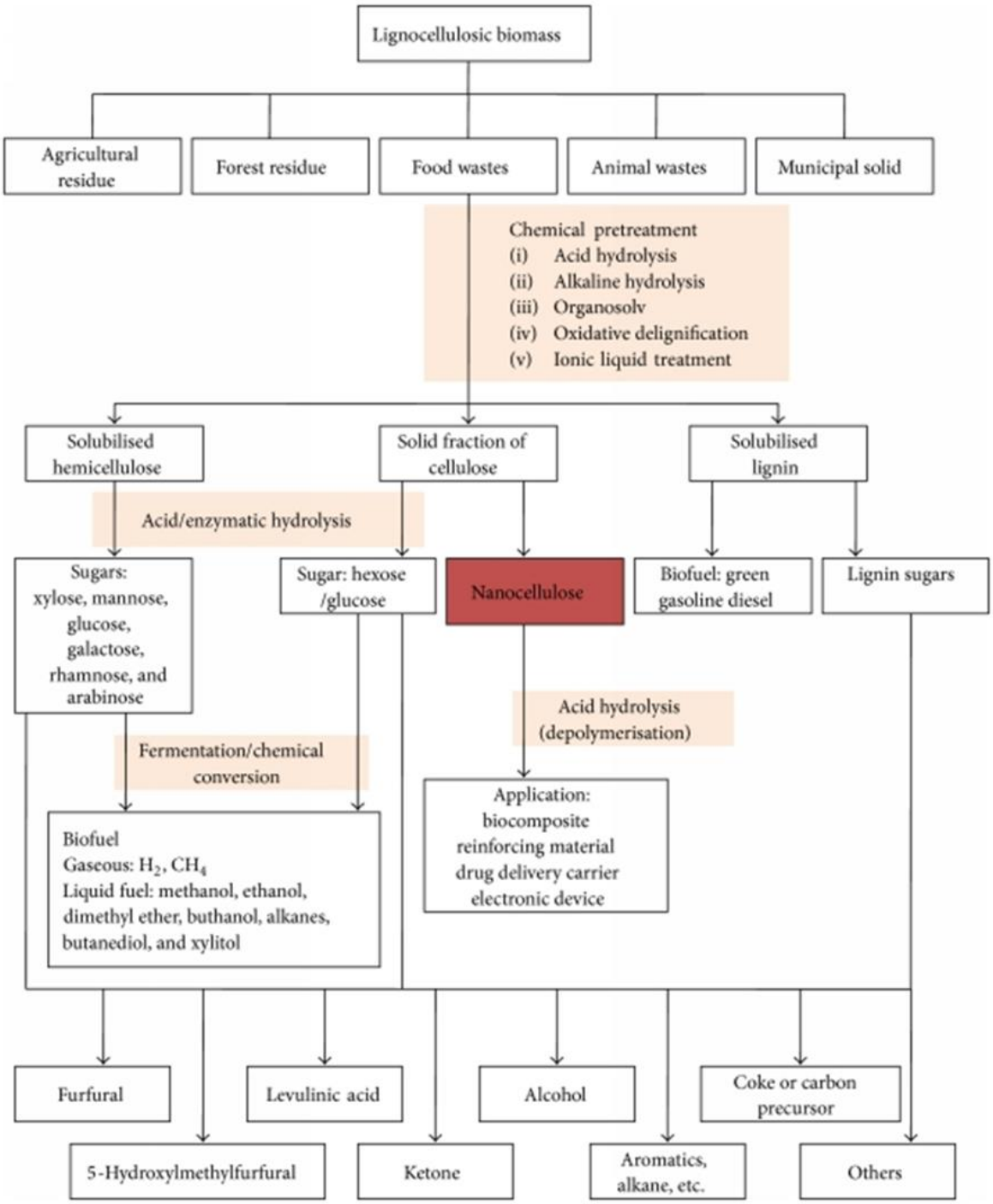


Figure 2.8: Deconstruction of lignocellulose (Lee et al., 2014).

Chemical pre-treatment strategies are shown (Figure 2.9) and briefly discussed



.

Figure 2.9: Strategy for lignocellulosic biomass fractionation (Lee et al., 2014)

2.2.1 Acid Hydrolysis

Acid hydrolysis is a process that target and disrupt the β (1,4) glycosidic bonds in cellulose. The mechanism suggests that hydronium ions targets and protonate the oxygen thus destabilising intermolecular and intra-molecular hydrogen bonds. It is an active agent for biomass decomposition to increase the production of monomeric sugars for biofuel manufacturing. Hydrolysing lignocellulosic biomass with acid is dangerous because of its toxicity, hazardous, and its corrosive nature. It requires acid resistance equipment hence it is an expensive process. Often the reaction becomes uncontrollable and produces undesirable products of monosaccharides undesirable coproducts such as carboxylic acids and alcohol (Peterson and Meyer, 2010).

2.2.2 Alkaline Hydrolysis

The mode of attack from alkaline hydrolysis entails disruption of lignin in lignocellulosic biomass. The mechanism involves formation of soaps (saponification) through reaction of caustic soda with carboxylic acids from hydrolysis of intermolecular ester bondsand reaction with xylan networks (hemicellulose) and lignin (Sun and Cheng, 2002) Breakdown of the ester linkages are replaced by nucleophilic acylation in the presence of alkaline salt. Alkaline hydrolysis has the following benefits:

(i) Swelling agent for cellulose
(ii) increase of internal surface area
(iii) Decrease of the degree of polymerization and crystallinity of cellulose
(iv) Hydrolysing the lignin structure by disrupting its glycosidic ether bond, and lignin can no longer behave as protective layer of cellulose and
(v) Make separated cellulose easy to be processed to nanocellulose synthesis.

2.2.3 Oxidation Agent.

Several oxidising agent such as organic peroxide, ozone, etc. are used to catalyse delignification process by reacting and cleaving lignin's aromatic structure (Yin et al., 2011). The mechanism favours high pH > 12, where the oxygen will be reduced to superoxide radical (−O2•), and cleave the ring by nucleophilic attack. The effective process oxidises aromatic ring of lignin and part of hemicellulose polymer to carboxylic acids compounds (e.g., formic acid, oxalic acid, and acetic acid). The process is appropriate for extraction of cellulose as the oxidation agent is more aggressive on lignin and partially on hemicellulose.

2.2.4 Organosolv

Organosolv involves pretreatment in the presence of organic solvents that act as dissolving agent by solubilising lignin and some of the hemicellulose under heat but not interfering with cellulose. The mechanism suggests that the OH− ion from alcohol solvent will attack the acid-ester bonds of lignin-hemicellulose and cleave ether linkages from lignin and hydrolyse the glycosidic bond in hemicellulose. Aromatics and polysaccharides of lignocellulose are also broken down. Generally the following solvents are used; in organosolv process; low boiling point organic solvents, for example, methanol, ethanol, acetone, ethylene glycol, and ethyl acetate (Zhao et al., 2009). Currently organosolv pretreatment is not economically viable as an extractive agent because of excessive washing with water is required to wash the pretreated components with organic solvent. and reclamation of organic solvents through distillation process leads to increase in energy consumption for the whole process (Zheng et al., 2009).

2.2.5 Ionic Liquids.

Ionic liquids (ILs) is a modern progress in chemical-based dissolution pretreatment technology. ILs are compounds composed of inorganic anions and organic cations. ILs are manoeuvrable and have a potential of solubilising a wide range of biomass materials. ILs with its catalytic effect possesses sites that are greatly available for the β-glycosidic bonds. They have a potential to dissolve cellulose, hemicellulose, and lignin under mild conditions without decomposing the chain's structure (Xiong et al., 2014). They are easily recovered at room temperature and can be reprocessed and reclaimed with ease Some examples of common ILs salts include 1-alkyl-3-methylimidazolium [Cnmim]+; 1-alkyl-2,3-dimethylimidazolium [Cnmmim]+; 1-allyl-3-methylimidazolium [Amim]+; 1-allyl-2,3-dimethylimidazolium[Ammim]+; 1-butyl-3-methylpyridinium [C4mPy]+; and tetrabutylphosphonium [Bu4P]+ with n = number of carbons in the alkyl chain (Tadesse and Luque, 2011).

2.3 Nanocellulose

Cellulose nanofibre (CNF) is produced from plants as a stable and well organized macromolecular structured material and is not reactive to most solvents (Takeshi et al., 2013). Nanocellulose are categorized according to their dimensions, functions, and preparation methods. This categorisation points to the origin and the process routes followed during production (Klemm et al., 2011). Herein, the nomenclature is used as (1) cellulose nanocrystal (CNC) and (2) nanofibrillated cellulose (CNF). Another type of nanocellulose is the (3) bacterial nanocellulose (BNC) which is synthesized with a bottom-up method from glucose by a family of bacteria, referred to as gluconoacetobacter xylinius (Klemm et al., 2011). In order to render cellulose molecules active few inorganic and organic solvents such as Ammonia and ethylene diamine (EDA) are often used to dissolve and derivatise it for further industrial processing. What makes CNFs more attractive are some of its characteristic properties when well-processed, namely; high aspect ratio (the length to diameter ratio), and high

crystallinity, low co-efficient of thermal expansion, low density, and high elastic modulus (Gao et al., 2013). Lately, more focus has been paid to the synthesis of the electrical conductive materials from the CNFs. A number of attempts to process cellulose have been explored and they include hydrolysis of cellulose with acid, alkalis, oxidants, enzymes, several solvents and mechanical processing methods. Thus far it has been difficult to prepare wood cellulose down to the dimensions of 3-4 nm without severely destroying the fibre (Gao et al., 2013).

2.3.1 Preparation of nanocellulose

The development of cellulose to NFCs demands severe mechanical action to achieve material suitable for oxidation into CNFs and CNCs (Khalil et al., 2014). The original material plant source and chemical reagents used to process cellulose determines the reactivity and physical properties of the final CNFs product. Encouraging efforts of oxidizing never-dried softwood cellulose with 2,2,6,6 -Tetramethylpiperidine-1-oxyl radical (TEMPO) and subsequent mechanical separation have been reported (Brodin & Theliander, 2012). The paper conductive films with good oxygen barrier properties, low thermal co-efficient of expansion close to glass (2.7 $X10^{-6}$ K^{-1}) with very high characteristic mechanical strength properties, good flexural and high refractive index of 1.545 have been synthesized at ambient conditions (Gao et al., 2013). The absence of vessels in softwood pulps makes it simpler to mechanically develop it compared to hardwood pulps. Previous research work has shown that the development of morphological properties of hardwood cellulose pulps for CNFs manufacturing are constrained by the presence of vessels. In the near future transparent conductive films have potential applications in the field of electronics such as flexible consumer electronics, smart clothing, energy harvesting devices and sensors. The imminent group of flexible transparent conductive films should overcome the cost barriers and economies of scales while maintaining their high transmittance and conductivity performance, etc. (Gao et al.,2013).

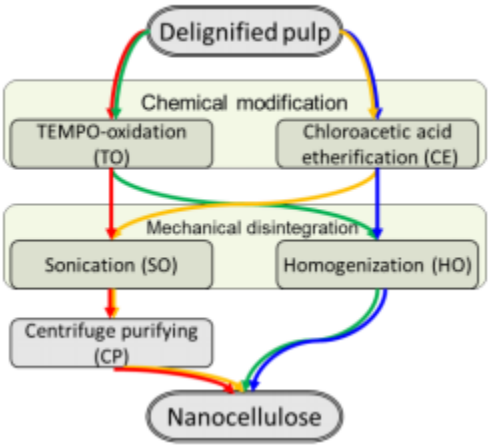


Figure 2.10: Nanocellulose synthesis process (Li, 2012))

2.4 Conductive Polymers

Conductive Polymers (CP) were discovered during the period of 1963 and its success story led Alan G. Heeger, Alan G. MacDiarmid and Hideki to win year 2000 Nobel Prize in Chemistry (Razaq, 2011). These special conductors offer significant characteristics over conventional metal and semiconductors. Some of the inherent characteristics they display are: participation in redox reactions, easy material design, and allow the flow of charge. In order for an organic polymer to be able to conduct current it must have free mobile electrons. The theory of electrical conductivity of solid materials is based on how the electrons are arranged and distributed within the molecules that make up the material (Atkins & de Paula, 2010). Many models exist to describe this phenomenon but the tight-binding approximation theory is discussed in this article. According to this model the valence electrons fill the molecular orbitals distributed across the solid. The main assumptions are that there is a probability to find an electron in an atomic orbital of atom A, and a probability also to find an electron in atomic orbital of atom B, then the overall wave function (ψ), is a superposition of the two atomic orbitals:

$$\psi_{\pm} = N(A \pm B) \qquad (2.1)$$

For diatomic hydrogen (H_2) ion:

A denotes $XH_{1SA,}$, B denotes $XH_{1SB,}$ and N is a normalization factor.

In compounds, numerous atomic orbitals overlay across each other and the result is the formation of molecular orbitals that are narrowly spread-out. They are almost similar in energy and produce continuous groups (bands) of energy levels (Atkins & de Paula, 2010). These energy groups are separated by band gaps where there are no molecular orbitals. Depending on the span of energy between different atomic orbitals, the different energy bands overlay across each**.** Another important phenomenon is the 'Fermi level'. Fermi level is described as the highest occupied energy level in a solid at zero absolute temperature (T = 0). This level is found closely to the centre of the band. If the band has orbitals that are not completely filled, the electrons from the Fermi level with suitable energy will enter nearby empty levels. The result is that these electrons move freely through the solid producing electrical conductivity (Atkins & de Paula, 2010). The atom comprises of small but substantial nucleus that contain particles called protons and neutrons. At the surrounding of the nucleus is a cloud of orbiting particles called electrons. The electrons can be transmitted from one body to another. When a body acquires electrons it becomes negative and the body that donates the electrons becomes positive. Charge separation plays a vital part in the operation of electrical equipment, such as batteries, microphones, and alternators in automobile electrical systems, etc. (Atkins & de Paula, 2010). Electrical conductors can be classified as either metallic conductors or semiconductors depending on the temperature depende**nce** of their conductivities. The conductivity of a metal conductor is inversely proportional to temperature. On the other hand, the conductivity of a semiconductor increases with temperature. An insulator is a semiconductor with a very low electrical conductivity. If there is a cube of material that is 1 cm on a side for a total cross-sectional area of 1 cm^2 and a length of 1 cm through which the electricity flows, and a 1-V potential difference in the circuit, and 1 ampere of electricity flowing (1 A = 1 C/s), then there is 1 Ω of resistance from Ohm's law (Kirkham, 2014).

2.4.1 Measuring resistance and resistivity of materials

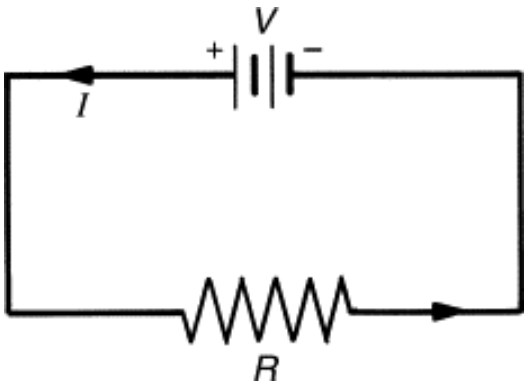


Figure 2.11: Diagram of electrical circuit with V, I, and R.

From the above diagram on figure 2.10, Ohm's law states that:

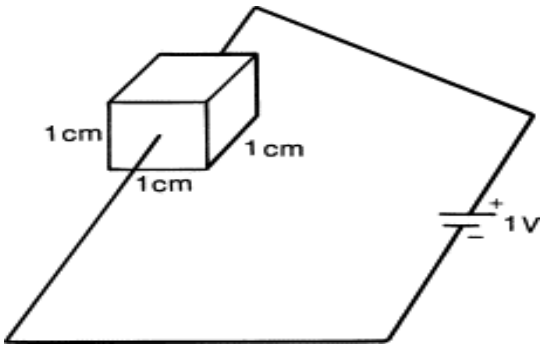
$$R = \frac{V}{I} \qquad (2.2)$$

Where:

R = Resistance of a conductor in ohms

V = Potential difference in volts (Vijay et al., 2011)

I = Electric current in amperes



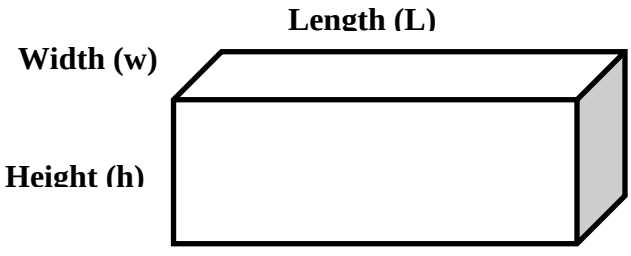


Figure 2.12: Diagram showing principle of resistance measurements (Kirkham, 2005)

If parameters such resistance (*R)*, length (*L*), and area (A), are known, then the resistivity, i.e. the ability of the material to resist the flow of current can be determined from the law of resistance, hence the conductivity could also be calculated. The law of resistance states that a piece of body with constant cross section has a resistance R that is proportional to its resistivity and length and inversely related to its cross-sectional area (Westland, 2011).

$$R = \rho \frac{L}{A} \qquad (2.3)$$

Where:

R = resistance (ohms)
L = length of material (centimetre)
A = Cross sectional area (square centimetre)
ρ = resistivity (ohms centimetre) (Kirkham, 2005).

From equation 3, it follows that conductivity sigma (σ), which is the reciprocal of resistivity is given by equation 4.

$$\sigma = \frac{1}{\rho} \qquad (2.4)$$

Where:

σ = conductivity
ρ = resistivity

The electrical conductivity is used to quantify the capability of the material to conduct an electric current, and the electrical resistivity measures how strongly the material opposes the flow of electric current. The international system (SI) units for these parameters are Siemens per metre (S/m) and ohmmeter (Ωm) respectively. In conducting polymers, conjugated double bonds facilitate electron conduction along the

chain (Atkins & de Paula, 2010). For example, in polyacetylene, the delocalized π-bonds electrons do move up and down the polymer chain. The electrical conductivity of polyacetylene increases significantly when it is partially oxidized by a strong dopant (Doping agent). The partially oxidized polyacetylene results in a product called a polaron because of a partially localized cation radical that travels through the chain. Further oxidation of a polymer by one more equivalent oxidant forms either bipolarons or solitons. Conductive polymers are organic polymers that allow the flow of electricity by virtue of conjugated double bonds. Generally their conductivities are similar to those of semiconductors (En Wikipedia retrived March 10, 2014). The important feature of conducting polymers is that they have a backbone of adjacent sp^2 hybridized carbon atoms. One valence electron on each carbon centre resides in a p_z orbital, which is orthogonal to the other three sigma-bonds. All the p_z orbitals combine with each other to form a molecule with a delocalized set of orbitals. Doping the material by oxidizing it increases the mobility of electrons due to an increased number of vacant orbitals to form a p-type semiconductor. The organic polymers can also be doped by a reduction process which introduces electrons to the unfilled band to create n-type materials. The benefit of the conductive polymers is the ease by which they can be processed, usually using the dispersion methods. Methods to improve the conductive properties of organic materials have been developed. If the conjugated organic polymer is undoped, the energy gap is larger than 2 eV and the material is either a semiconductor or an insulator and the material cannot be thermally activated (En Wikipedia retrived March 10, 2014). For example undoped polyacetylene has a low electrical conductivity of around 10^{-10} to 10^{-8} S/cm. However if the polyacetylene is doped with less than 1% of doping material, the electrical conductivity increases in order of around 0.1 S/cm. Levels of around 0.1–10 kS/cm are typical for doped organic polymers. The highest reported conductivity value for doped acetylene was 80 kS/cm Heeger et al., 1988).

2.4.2 Applications of conductive polymers

There is a lot of interest and attraction that has developed in the area of transparent flexible energy storage devices such as supercapacitors (Wang, et al., 2013). Among .many CP explored great potential had been observed but not limited to; polyacetylene (PA), polypyrrole (PPy), polyaniline (PANI), polythiophene (PT), poly-(3,4-ethylenedioxythiophene) (PEDOT), and graphene oxide (GO) (Razaq, 2011). Applications of transparent conductive coatings have been extended broadly to electrodes where light transmission is needed such as in photo-electrochemical experiments (Moreno & Araiza, 2005). Indium tin oxide (ITO), and aluminum doped zinc oxide (AZO) have been discovered to provide suitable coatings for the transmission of light (Rabe, et al., 2007). The performance of an electronic device is essentially dependent on the type of the substrates used during the fabrication and is therefore very important for the fundamental properties of the devices (Wang, et al., 2013). The following are examples of the substrates; cellulose, ITO-coated glass, polyethylene terephthalate (PET), polyethylene naphthalate (PEN) polycarbonate (PC), and polyimide (PI). Some of these offerings are thermoplastics and thermosets that display undesirable characteristic properties such as inflexibility, large co-efficient of expansion (CTE), poor printability and recyclability. An ongoing research has focused on biodegradable CNFs that might have good optical transmittance properties of above 90% in the visible region and low CTE of about 2.7 ppm K^{-1} in combination with high mechanical strength and flexibility (Wang et al., 2013). In order to control nanoscale constituents over a substrate a Layer-by-layer (LBL) assembly method is often employed (Gao et al., 2013). The mechanism of an LBL assembly method involves hydrogen bonding, $\pi - \pi$ stacking interactions, and electrostatic forces between the substrates and different dilute solutions. An LBL assembly can be used to deposit and integrate nanoscale particles to a variety of nanostructures such as nanotubes, nanosheets, nanoparticles and biomolecules with nanofibres. The advantages of an LBL assembly method in grafting the nanoscale dynamic particles onto CNF paper are that it forms thin films and conserve the active surfaces of the nanoscale structure, the characteristic that is vital for the performance of the electronic devices (Wang et al.,

2013). Previous work has shown that an electrical conductive polymer, (PANI) has the following encouraging properties; a pseudo-capacitive behaviour, low cost, ease of synthesis, and stable redox properties and for this reason it has been used to produce electrode materials. Polypyrrole (PPy) is another organic conductive material that has been well researched because it can be easily synthesized, thermally and environmentally stabilized. Because of its high electrical conductivity this property has made it earn applications in the production of counter-electrodes in electrolytic capacitors, light-weight batteries, anti-corrosive coatings, sensors, actuators and for membrane separation (Khalil et al., 2012). However the PPy has some application constraints that are due to its poor mechanical properties. To deal with this issue blending PPy with other natural and synthetic polymers to form conductive composite materials with better electrical conductivity and high mechanical strength properties has been considered. A number of flexible transparent conductive films based on reduced graphene oxide/ nanocellulose composites, metal oxides semiconductors, carbon nanotubes, and metallic nanowires have been produced (Gao et al.,2013). Different procedures to embed these nanomaterials on flexible plastic substrates such as PET by spin coating, filtration, Langmuir-Blodget assembly, dip-coating, etc. have been employed. However plastic substrates introduce another problem of high co-efficient thermal expansion. The plastic substrate may not be compatible with high processing temperatures and are also not regarded as eco-friendly materials (Gao et al.,2013).

2.4.3 Graphene

Graphene is prepared from the parent graphite in a reported number of ways. The schematic diagram (Figure 2.12) shows a recent simplified method of preparing graphene termed “Solvothermal exfoliation of intercalated graphite flakes” (Farag et al., 2015). According to this procedure, graphite is first treated with tartaric acid followed by thermal treatment at 750 °C for one minute. The product is further treated with isopropanol at 400 °C for 2 hr. (Farag, et al., 2015). Graphene does not have the same amazing attributes such as mechanical strength, electrical and thermal conductivity displayed by carbon nanotubes (CNTs (Sundararaj, 2012). CNTs have grown

tremendously as a research area and have publicised applications in drug delivery, gene delivery, biosensors and medical imaging. In order to activate the graphene, it has to be oxidised to graphene oxide (GO).

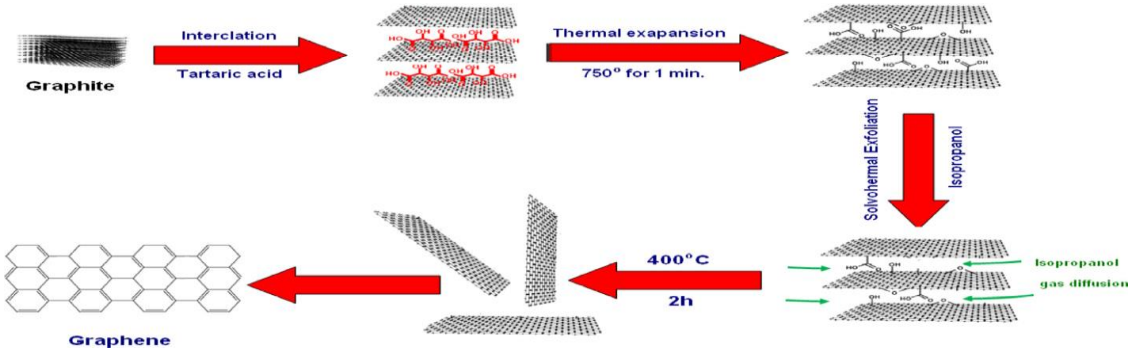


Figure 2.13: **Mechanism of exfoliation of graphite flakes to graphene (Farag et al., 2015).**

2.4.4 Graphene oxide (GO) and reduced graphene oxide (rGO)

Graphene oxide can be produced in a number of ways such as oxidising graphite with highly oxidising chemicals such as nitric acid, sulphuric acid and potassium permanganate. The results of the oxidation are the formation of the epoxy groups as shown in figure 7a (the red modelling balls represents oxygen atoms) (Songfeng et al., 2010). It was observed that the nanosheets prepared from GO has the tendency to stack during its reduction and subsequently the activity of the supercapacitors constructed from them is lowered (Wang et al., 2013). Experiments proved that when a Layer-By-Layer assembly (LBL) of GO nanosheets was done with conductive PANI nanowires on the substrate, and the GO nanosheets were reduced with hydroiodic acid, hydrazine or any suitable reducing agent to form reduced graphene oxide (rGO), the compact stacking of GO nanosheets was successfully avoided. The rGO was observed to have improved *in vitro* photo-thermal sensitivities than CNTs. Reduction enables the lowering in vertical resistivity of the multilayer as well as boosts the low capacitance of rGO. The reduction mechanism proposed for hydroiodic acid is shown on figure 2.13 below.

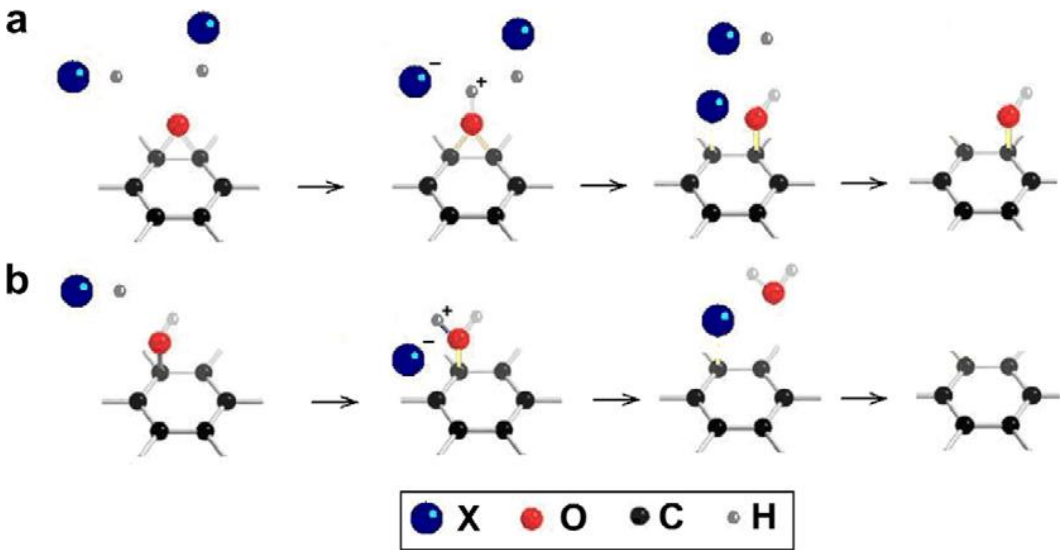


Figure 2.14: Reduction mechanism of GO (a) with hydro-iodidic acid and ring-opening of an epoxy group and (b) Halogenation substitution reaction of a hydroxyl group (Songfeng et al., 2010)

Chapter 3: Experimental procedures and analysis techniques

3.1 Raw materials and Characterisation Instruments

The following materials and analytical techniques were used for the synthesis of electrical conductive cellulose

Materials

- Eucalyptus grandis pulp (92 alpha) supplied by Sappi Saiccor Ltd. RSA
- TEMPO (2,2,6,6-tetramethylpipiridine-1-oxyl) Supplied by Sigma-Aldrich, USA.
- Graphene Oxide supplied by Sigma-Aldrich, USA
- Sodium bromide supplied by Merck
- Sodium hypochlorite solution purchased from Rochelle Chemicals, RSA
- Hydro-iodic acid, supplied by Sigma-Aldrich, USA
- Cupric Sulphate supplied by Merck

These reagents were analytically pure grades and were used without further purification.

Analytical techniques

- Morfi Fibre Wall Thickness (MFWT)
- Scanning electron microscopy (SEM)
- Transmission electron microscope (TEM)
- Fourier Transform Infra-Red (FTIR) Spectroscopy
- Hounsfield Tensile Strength Tester, and
- Multimeter for the electrical resistance measurement

3.2 Synthesis of microfibrilated cellulose (MFC)

The variables and settings of the Pilot Refiner used for the preparation of cellulose microfibrilated fibres are in Table 4.1. The microfibrilated cellulose (MFC) was achieved by mechanical fibrillation of the suspension of *eucalyptus grandis* (*E.grandis*) pulp - 92 alpha in water at a consistency of 3%. The Pilot Refiner used as fibrillating equipment is shown in Figure 3.1. The process involved introducing in the disintegrating tank dry pulp sheets into water. The total batch size was 243 kg. The disintegration of fibres, hydration and agitation lasted for 30 minutes. The fibre slurry was pumped through the grooved metal disks i.e. rotor and stator from the disintegrating tank using the hydraulic pump. The fibre suspension was drawn from the bottom of disintegrating tank and travelled through the refining loop and returned back into the tank (Figure 3.2). The fibre suspension was pumped through the centre of the stator plate positioned face to face with the rotor plate as shown in appendix Figure 3.3. The pulp slurry spread over the bars and grooves of the closed refiner plates and moved outwards exiting at the small outlet opening at the end of the disks. The gap between disks during operation was adjusted and maintained between 0.2 mm and 0.5 mm to achieve maximum fibrillation. The refining power was maintained at 26 kW for fibrillating *E.* G*randis* pulp. The Pilot Refiner was equipped with a carousel that periodically sampled pulp into beakers according to the set program. During fibrillation process the cell walls of the fibres were peeled off and formed microfIbrils (Figure 4.4); this process is often accompanied by undesirable shortening of the fibres.

3.3 Synthesis of CNF and [CNF/Cu^{2+}/rGO]*n*

The modified procedure described by Isogai (Saito, et al., 2006) cited in Cellulose nanofibres/reduced graphene oxide flexible transparent conductive paper by (Gao et al.,2013) was used to process MFC into transparent cellulose nanofibres (CNFs). The procedure followed stated that: a 400 ml batch should consist of 2 g *E grandis* cellulose, 0.033 g TEMPO, 0.33 g sodium bromide, 30 mmol of sodium hypochlorite and the

balance being water. The batch was constantly stirred in a water/ ice bath mixture controlled at 10°C. The pH was adjusted to 10 using 0.5M sodium hydroxide solution. The reaction mixture was allowed to stand for 6 hours. The product was washed three times using distilled water and centrifuged at 10 000 rpm. A 0.2% nanocellulose solution was sonicated for 45 minutes at 540 watts using a bench Sonicator. The final product was stored in a fridge set at 4°C. The wet CNF gel was dried at 25°C on a PET tray overnight in the laboratory oven. The dried sheets were cut into strips using a pair of scissors. The dimensions of the strips were 90 mm in length and 15 mm in width. The dried cellulose were characterised using SEM. The nanocellulose gel was characterised using TEM. The strips were also tested for tensile strength using the Hounsfield instrument. The CNF gel was also mixed with the Cu^{2+} ions solution (1mg/ml, pH 4.5), and dried in the oven to form a copper impregnated CNF sheet at 65 °C. Subsequently the strips were dipped in Graphene Oxide (GO) (1 mg/ml) hence termed CNF/ Cu^{2+}/GO. The CNF/ $Cu^{2+/}$GO strip were reduced with hydro-iodic acid (HI) and termed [CNF/Cu^{2+}/rGO]n where n is the number of dipped layers here. The blank CNFs strips (i.e. cellulose strips without treatment with Cu^{2+} ions, GO and HI) strips were tested for electrical resistance using the Multimeter together with the [CNF/Cu^{2+}/rGO]n.

3.4 Process flow diagrams of the Pilot Refiner

Figure 3.2 shows the process flow diagrams for Pilot Refiner equipped with a disintegrating tank, hydraulic pump, 12 inch refiner with mechanical disks (rotor and stator), carousel, hot water geyser and electrical DB.

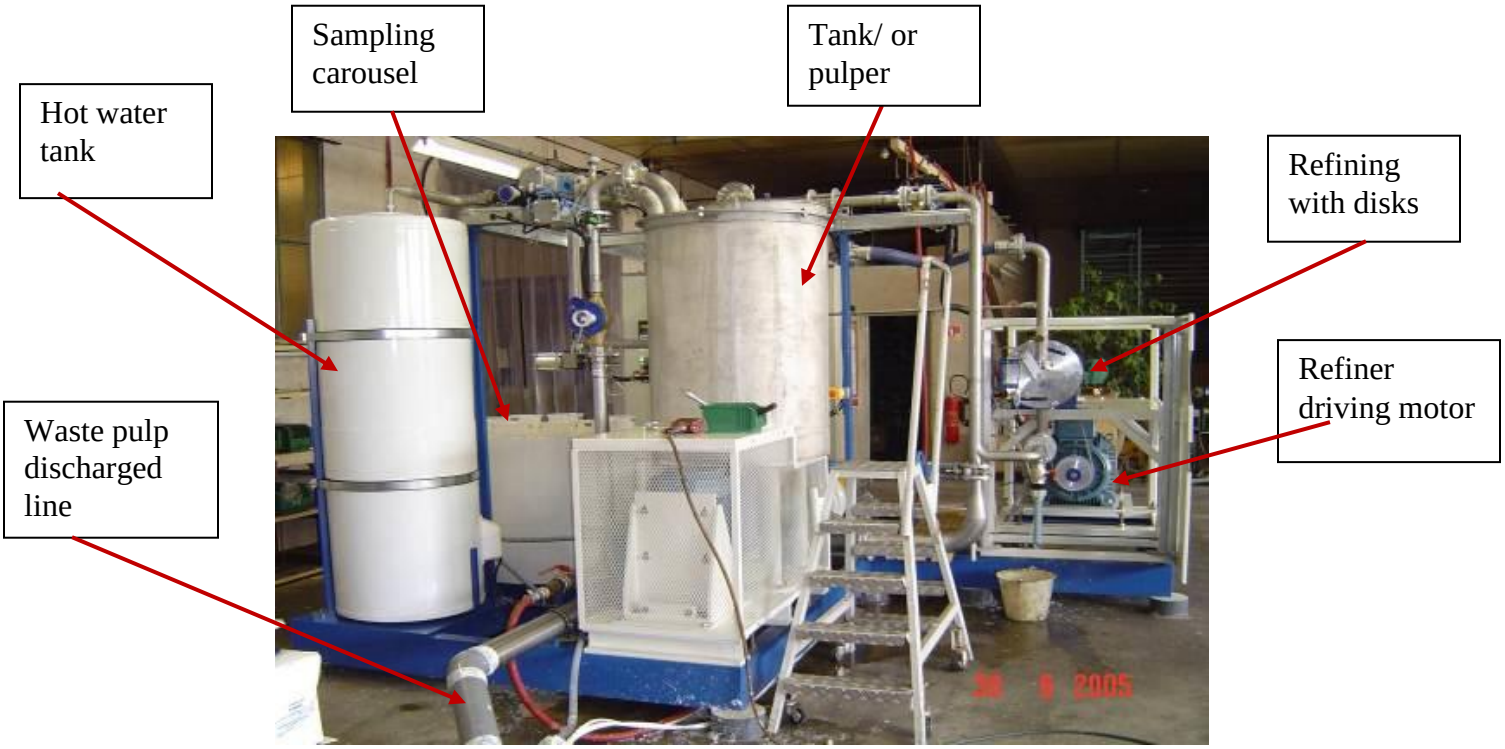


Figure 3.1: Photograph of the Pilot refiner

Table 3.1: Process variables of **pilot refiner**

Refiner parameters	Measurements
Diameter of the refining disk plates	12 inch plates (both stator and rotor)
Plates bar width	1.5 mm
Plates groove width	1.5 mm
Plates bar height	4 mm
Gap between the plates during refining	average 0.2 mm
Refiner inlet pressure	1.6 bar
Refiner outlet pressure	2.7 bar
Pulp flow rate	8 m^3/h
Fibre swelling time in water before refining	1 hour
Refining intensity (energy distribution per bar length)	0.3 J/m
Specific refining energy (energy transferred to fibre)	588 kWh/ton
Shöpper Riegler of the pulp before fibrillation (^{0}SR)	21 ^{0}SR
Shopper Riegler of the pulp after fibrillation ((^{0}SR)	Above 95 ^{0}SR

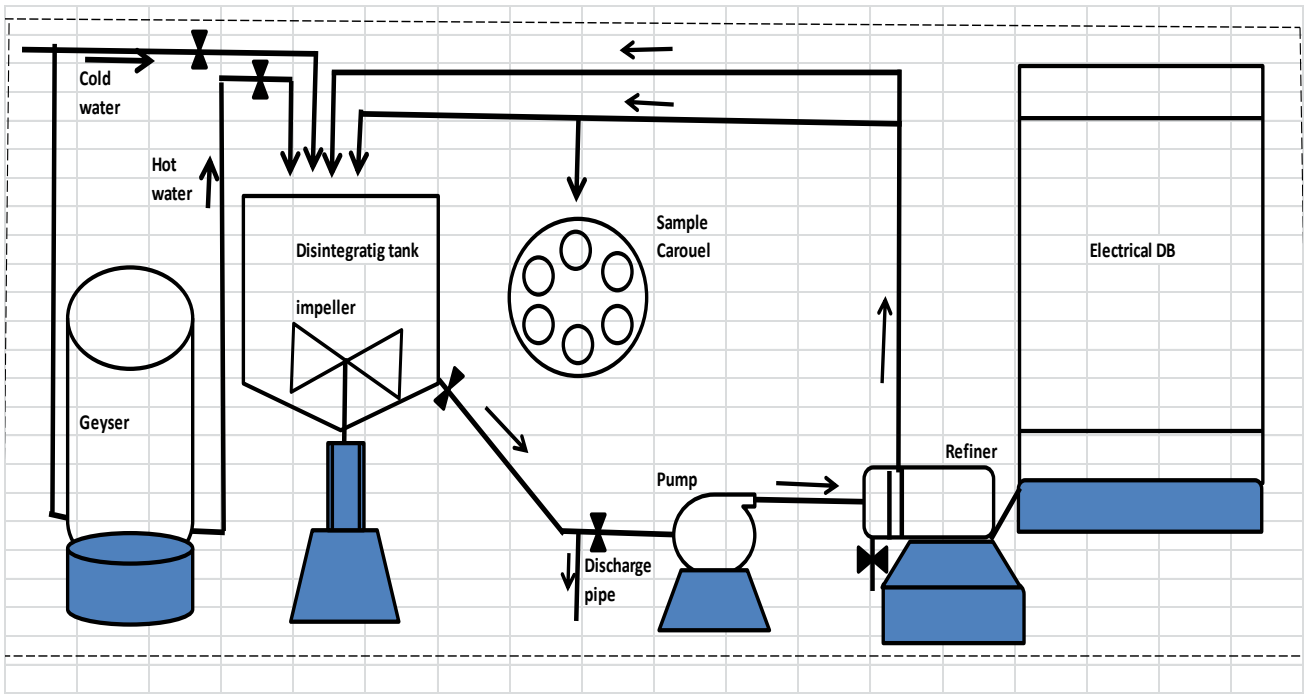


Figure 3.2: Process flow diagram of the Pilot refiner

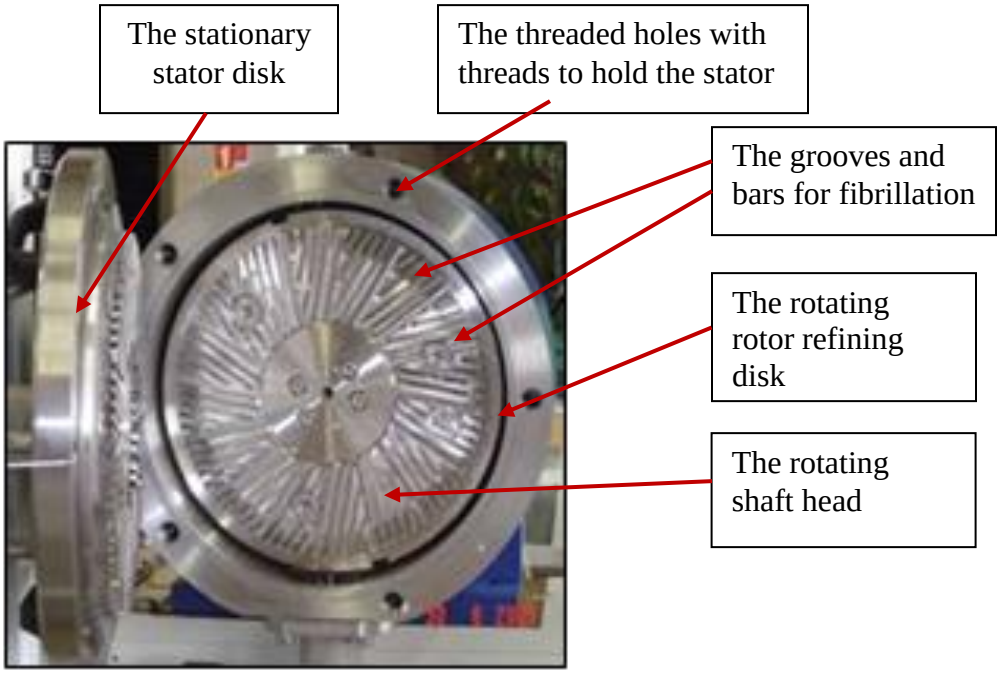


Figure 3.3: Rotor and stator disks of the Pilot refiner

3.5 Analytical Techniques

3.5.1 Morphological Fibre Wall Thickness Analysis (MorFi WT)

The size distribution of refined and unrefined E. grandis pulp was determined using the Morphological Fibre (MorFi) Analyzer (Techpap, France). The measurement resolution is down to 0.7 µm and gives complete information with regards to average cell wall thickness and distribution (Eymin-Petot-Tourtollet, 2000). The fines content was measured in term of the thickness in the prepared samples.

The equipment, as shown in Figure 3.4 integrates a digital camera and a software package, which can automatically measure fibres in suspension. This equipment can analyze low concentration of pulp suspensions and required a specified fibre dimensions to measure the analysed parameters. Samples were taken offline, from an

automatic carrousel containing 9 sample cells controlled by a PC as shown in Figure 3.5.

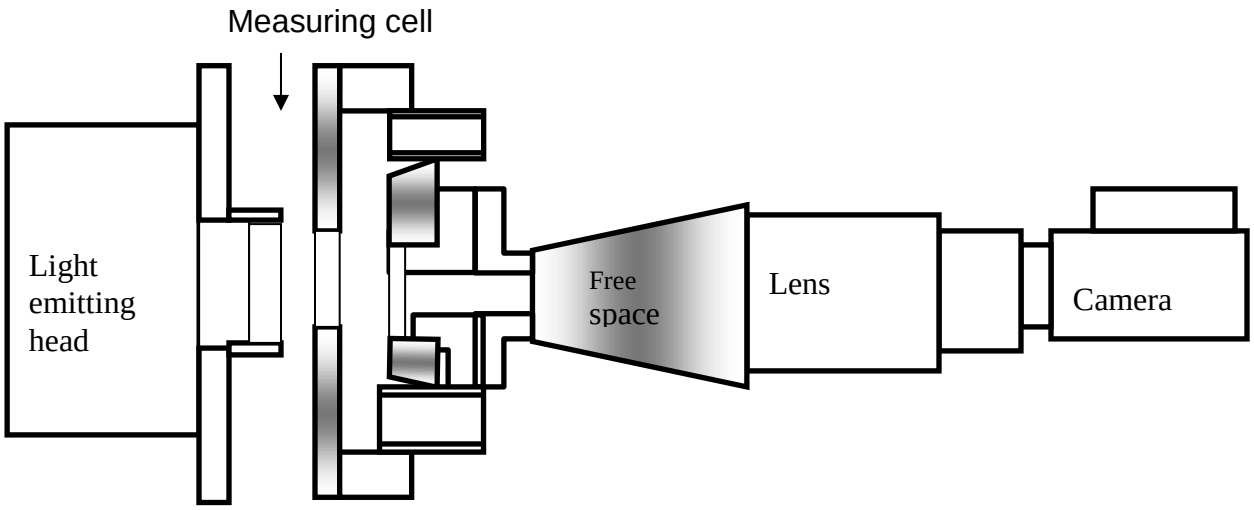


Figure 3.4: Diagram illustrating the KEY components of the Morfi MWT



Figure 3.5: TECHPAP Instrument to measure MFWT

3.5.2 Scanning electron microscopy (SEM)

The surface morphology was recorded with Scanning Electron Microscope (Model: S-4300, Japan). The electron beam traverses a series of lenses, and the reflected one on the specimen is collected by detectors. The transferred electron signal had colors intensity depending to the strength of the detected signal. The samples used in this analysis should be conductive to avoid charging artifacts; which affect the image quality. Samples were mounted on metal stubs in a coater unit, and placed into the SEM with higher energy electrons between 2 to 1000 keV. The schematic diagram of key components of SEM instrument is shown in Figure 3.6

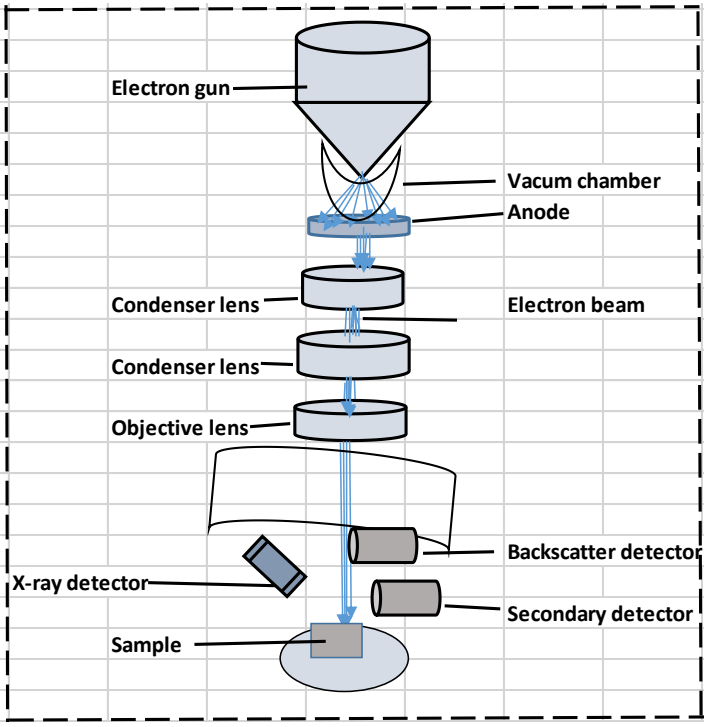


Figure 3.6: **KEY components of SEM instrument (Skoog et al., 2014)**

3.5.3 Transmission electron microscope (TEM)

TEM works on the same fundamental laws that govern the operation of light microscope except that it achieves more magnification than what light microscopes achieve because light is restricted by its wavelength whereas TEM uses electrons. The wavelength of light is approximately 600 nm and the wavelength of an electron is 6 pm. The shorter wavelength gives higher resolution or the magnification. The light used by a TEM instrument originates from the electrons (Microscopemaster.com, 2015). TEM analysis was used to visualize the change in the morphology of the nano cellulose fibre sample. In this study, TEM measurements were done on a Jeol model 1200EX instrument operating at 80 kV. Electrons are easily deflected and accelerated using an external field and potential, respectively. The electrons travelled through the sample, and are either scattered or transmitted. The non-uniform distribution of electron contained the details structured of the sample analyzed. The TEM consists of the following critical components that lead to the formation of an image (Figure 3.7):

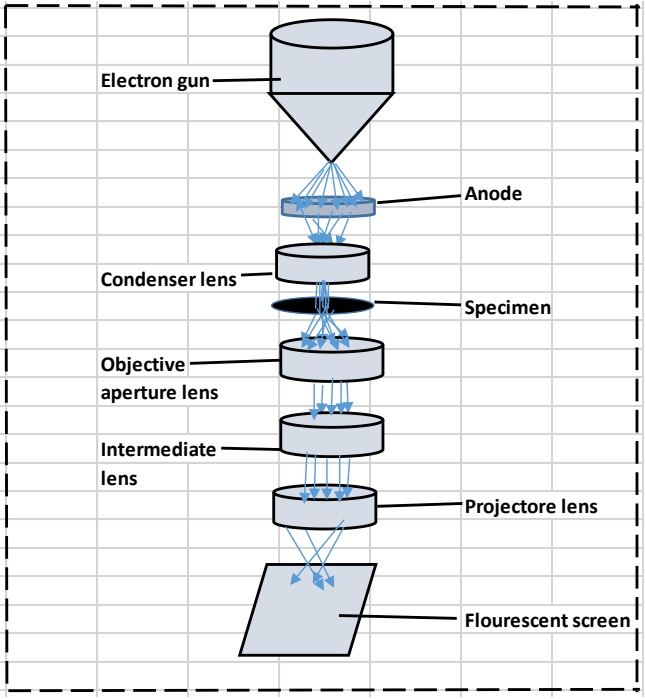


Figure 3.7: Key components of TEM instrument (Skoog et al., 2014)

3.5.4 Fourier Transform Infra-Red (FTIR) Spectroscopy

In this technique, the infrared beam after leaving the interferometer passes through an optically dense crystal with higher reflective index. After its interaction with the sample, the infrared spectrum is obtained. The total reaction time of the cellulose with oxidizing agents was six hours. The concentrations (concentrations) of the oxidizing sodium hypochlorite (NaOCl) and the catalyst sodium bromide (NaBr) were also doubled and halved. The FTIR spectra of all cellulose nanofibres obtained were determined and analyzed. The energy absorbed by the organic groups and subsequent vibrations, stretching, rotation, and bending of functional groups was recorded at specific wavenumbers against absorbance. The scans were carried out between 650 and 4000cm^{-1} at the resolution of 4cm^{-1}. A schematic diagram of an FTIR instrument is shown in Figure 3.8.

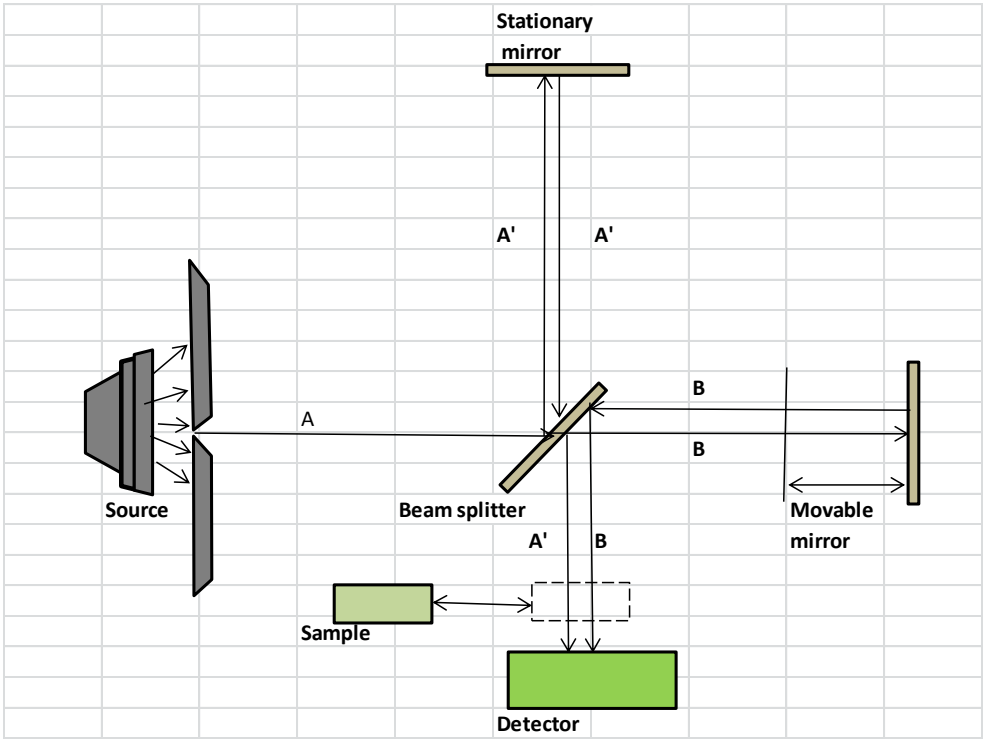


Figure 3.8: **Schematic diagram of FTIR spectroscopy (Skoog et al., 2014)**

3.5.5 Hounsfield TensileTester

It has been reported that the tensile strength of the sheet produced from the CNF material was very high. As part of the objective of the research it was important to characterize the tensile strength of the CNF synthesized with the TEMPO mediated oxidation method. In order to achieve this objective the concentrations of the NaBr catalyst and NaOCl solution were varied twice from the normal concentration. The concentration of each chemical was doubled and also halved from the normal inclusion level in the process. Sheets were prepared from the CNF gels under pressurized condition to avoid creeping using the Rapid Köthern Drier instrument. Several strips with lengths of 90mm and 15mm in widths were cut using the customized cutter designed to cut the tensile strips for tensile strength tests. Data generated from tensile strength tests was evaluated using the minitab statistical program.

The procedure involved preparation of nine to ten replicas of CNF strips from each of five samples produced with varying NaOCl and NaBr concentrations as shown in Table 3.2.The tensile strength of the CNF was measured with Hounsfield Tensile Tester (Figure 3.9).

.

Table 3.2: Concentrations of NaOCl and NaBr used to produce different CNFs

Chemical name	Concentration used per 400ml batch	Comment
NaOCl	8 mmol	Standard NaOCl concentration
NaOCl	16 mmol	Doubled NaOCl concentration
NaOCl	4 mmol	Halved NaOCl concentration
NaBr	0.33g	Control NaBr concentration
NaBr	0.66g	Doubled NaBr concentration
NaBr	0.165g	Halved NaBr concentration

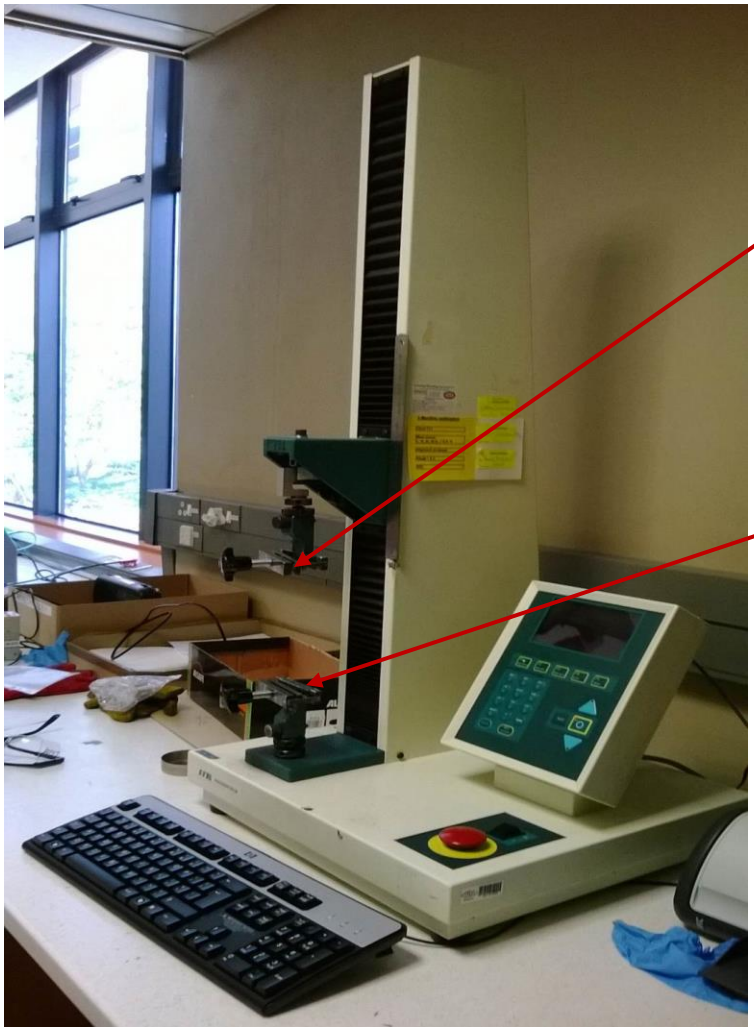


Figure 3.9: Hounsfield instrument for testing tensile strength

Statistical analysis method of CNF tensile strengths data

The objective of the statistical analysis was to determine whether there are significant differences between the tensile strengths of strips prepared from different NaOCl and NaBr concentrations. This difference will be achieved by comparing the means (averages) of the results obtained the groups of samples.

The Null Hypothesis: The Null Hypothesis states that all means are statistical equal i.e. there is no significance difference between the means of different formulations.

The Alternate Hypothesis: **"**States that at least one mean is statistically different".

Statistical tests were performed under the following protocols:

Data type – Continuous

Comparisons – More than two means

Tests – One way ANOVA and test for equal variances

Alpha level (α) - 0.05

Chapter 4: Results and discussion

4.1 Characterisation of the unrefined and the refined pulp with Morfi WT

The fibres of the unrefined and refined *E.grandis* pulp were dispersed in water and the cell Mean Wall Thickness (MWT) was measured using the Techpap MorFi WT instrument (Figure 3.5). The unfibrilated pulp had a fibre distributions as seen in Figure 4.1 lying between 3.09 and 3.26µm with the average thickness of 3.18 µm (Table A.1 and A.3 in appendix). While the mechanically fibrilated fibres had a fibre distributions as seen in figure 4.2 lying between 3.00 and 3.09µm with the average thickness of 3.07µm (Table A.2 and A.4 in appendix). These values indicates that there was substantially reduction in cell wall thickness as a result of mechanical fibrilation. Fibrilation refers to the peeling and cutting process of the outer and inner layers of the cellulose fibre walls. The net results of the fibrilation is the formation of both microfibrils, fines and nanofibrils. Further oxidation with sodium hypochlorite/ TEMPO and sodium bromide converted microfibrils into nanofibrils. The difference in size distribution between unrefined and refined cellulose can be seen in the following Figures 4.1 and 4.2.

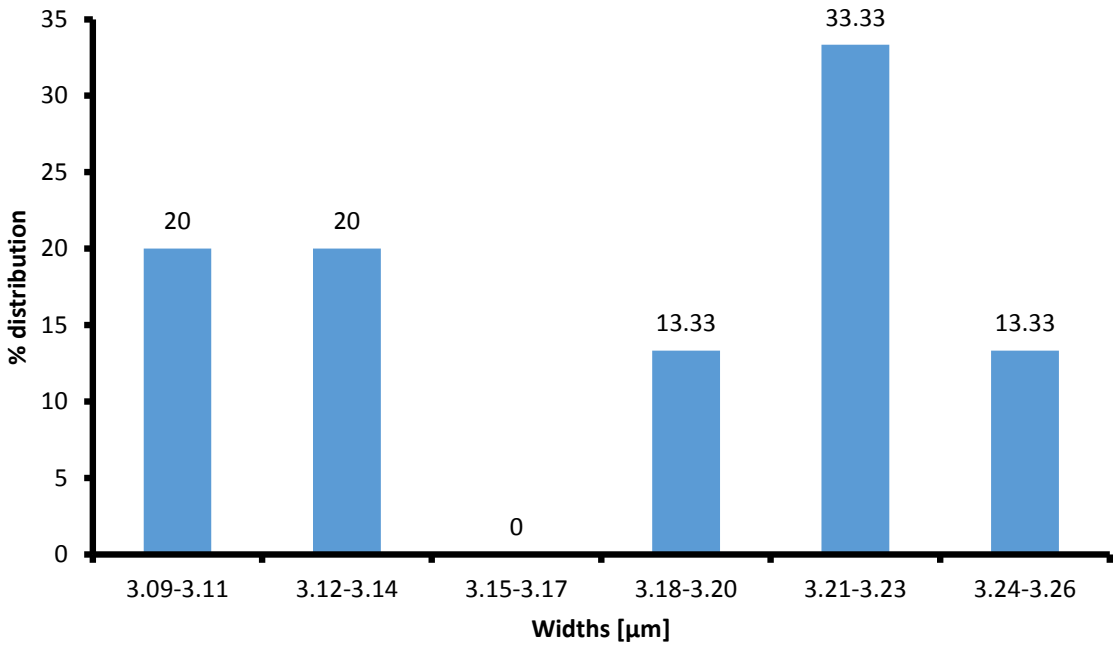


Figure 4.1: Graph showing MWT distribution ofunrefined *E.grandis* pulp

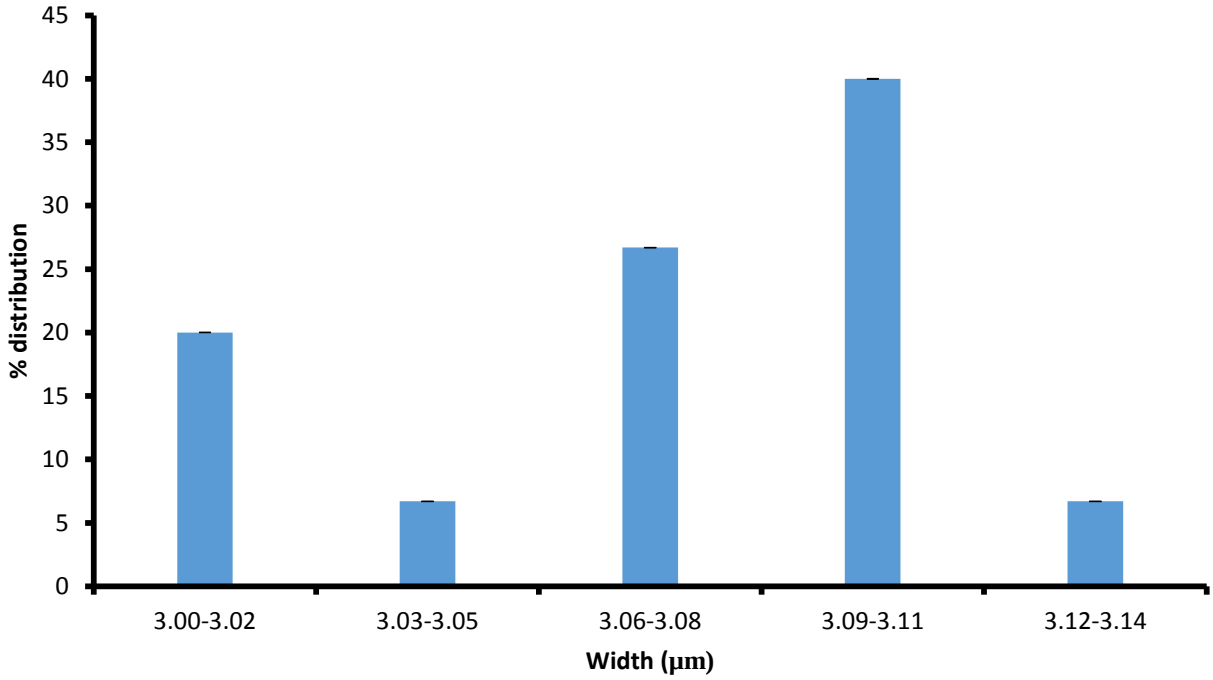


Figure 4.2: Graph showing MWT distribution ofrefined *E.grandis* pulp

4.2. Characterisation of un-oxidised cellulose pulp with SEM

The virgin *E. Grandis* pulp was supplied as dry sheets at 90% consistency. A small piece of sheet (5 mm X 5 mm) was characterised with SEM instrument. The average fibre width of unrefined *E. Grandis* fibres was found to be approximately 3.18 µm by MorFI WT in Appendix (Table A.3). The average cross-sectional width of pilot refined pulp fibres were found to be 3.07 µm by MorFI WT in Appendix (Table A.4). The decrease in the average fibre width between the unrefined and the refined fibre was caused by fibrilation action with refiner mechanical metal bars. The fibre walls around the lumen collapsed during the refining process. From the SEM images (Figures 4.3 and 4.4), it was observed that the width of the flattened fibre ranged from less than 1 micron to about about 20 µm. The fibres appears in different shapes i.e. straight, curled and even kinked. The fibres consists of very little macrofibrils (bundles of microfibrils). The image of the mechanically refined *E. Grandis* fibres (Figure 4.4) showed frail and severely fibrillated fibres. The pulp has been forced through a small gap of between 100 to 300 **µ**m between the rotor and the stator (Figure 3.3) in Appendix. The surface of the fibres no longer appeared smooth and intact after mechanical fibrillation but they appear to have rattled structures characterised by many macrofibrils (Compare Figures 4.3 and 4.4). The mechanically frail structure would facilitate the ease of penetration by oxidising chemicals and the reaction thereof with microfibrils.

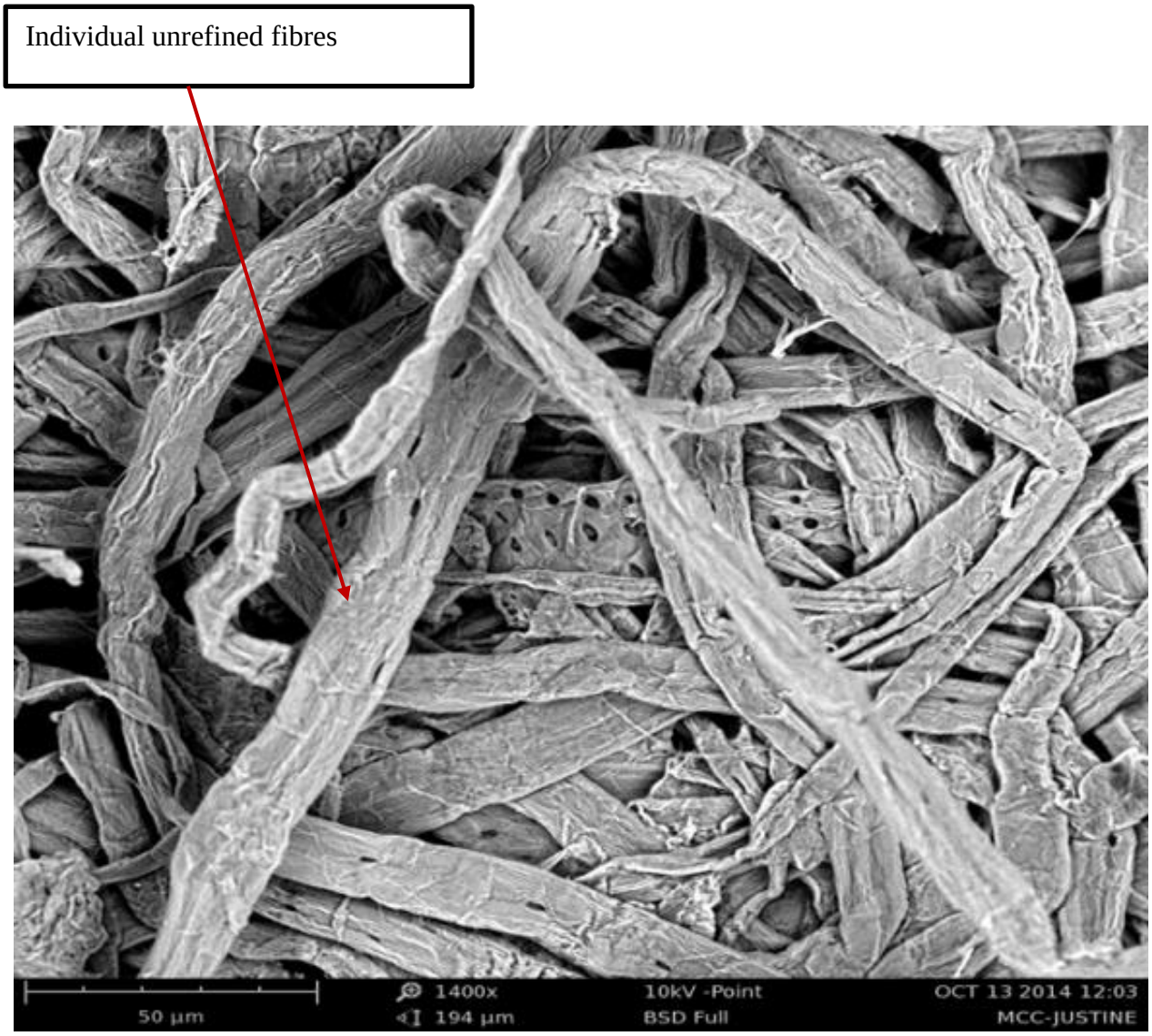


Figure 4.3:SEM image of unrefined *E.grandis* pulp, 1400x resolution

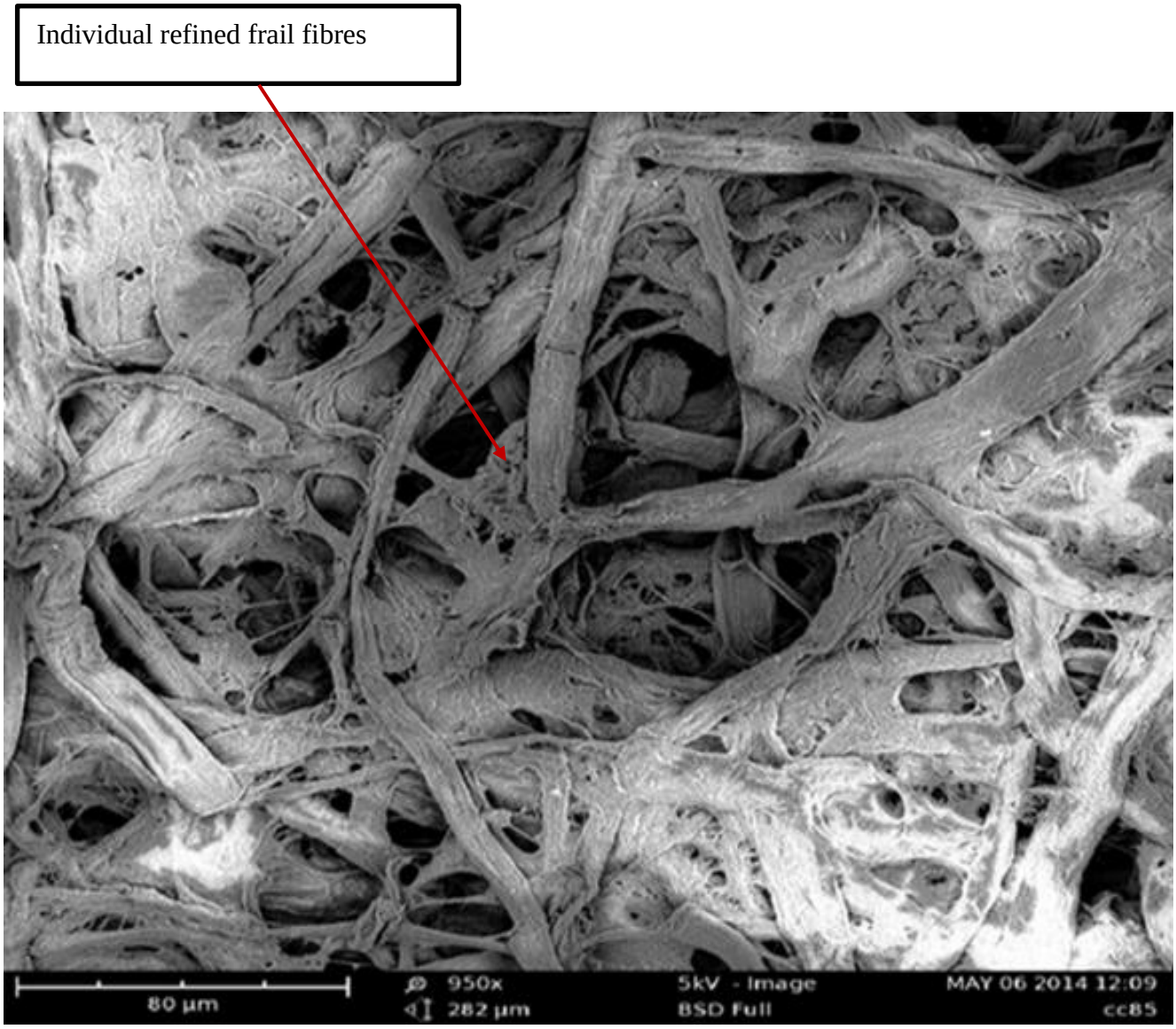


Figure 4.4:SEM image of mechanically refined *E.grandis* pulp, 950x resolution

4. 3 The SEM image of TEMPO-oxidised cellulose

The high resolution (1750x) transversal SEM images revealed that the TEMPO-oxidised NFC repolymerised during the drying process as shown (Figure: 4.5) (Brinchi, et al., 2013). The image showed a thick gel-like substance of dry nanofibrilated cellulose. The high resolved SEM image (3800x) (Figure 4.6) showed multiple layers of both microfibrilated and nanofibrilated cellulose fibres. The SEM image (Figure 4.7) showed

the surface of the oxidised nanofibrilated cellulose fibre. The foam-like surface is nanocellulose fibrils. It is this fine material that repolymerises when the water is vaporised from the cellulose gel. Different magnification levels are shown in Figures 4.5 (Low magnification), 4.6 (moderated magnification) and 4.7 (Highly magnification). Low magnification could not display a clear view; moderated can display few layers of nanocellulose bonded together and highly magnification can be used to view a singly nanocellulose fibre. The SEM confirms that the material produced was a nanocellulose fibre as can be seen in Figure 4.7. A single isolated nanocellulose, which is not degraded to glucose.

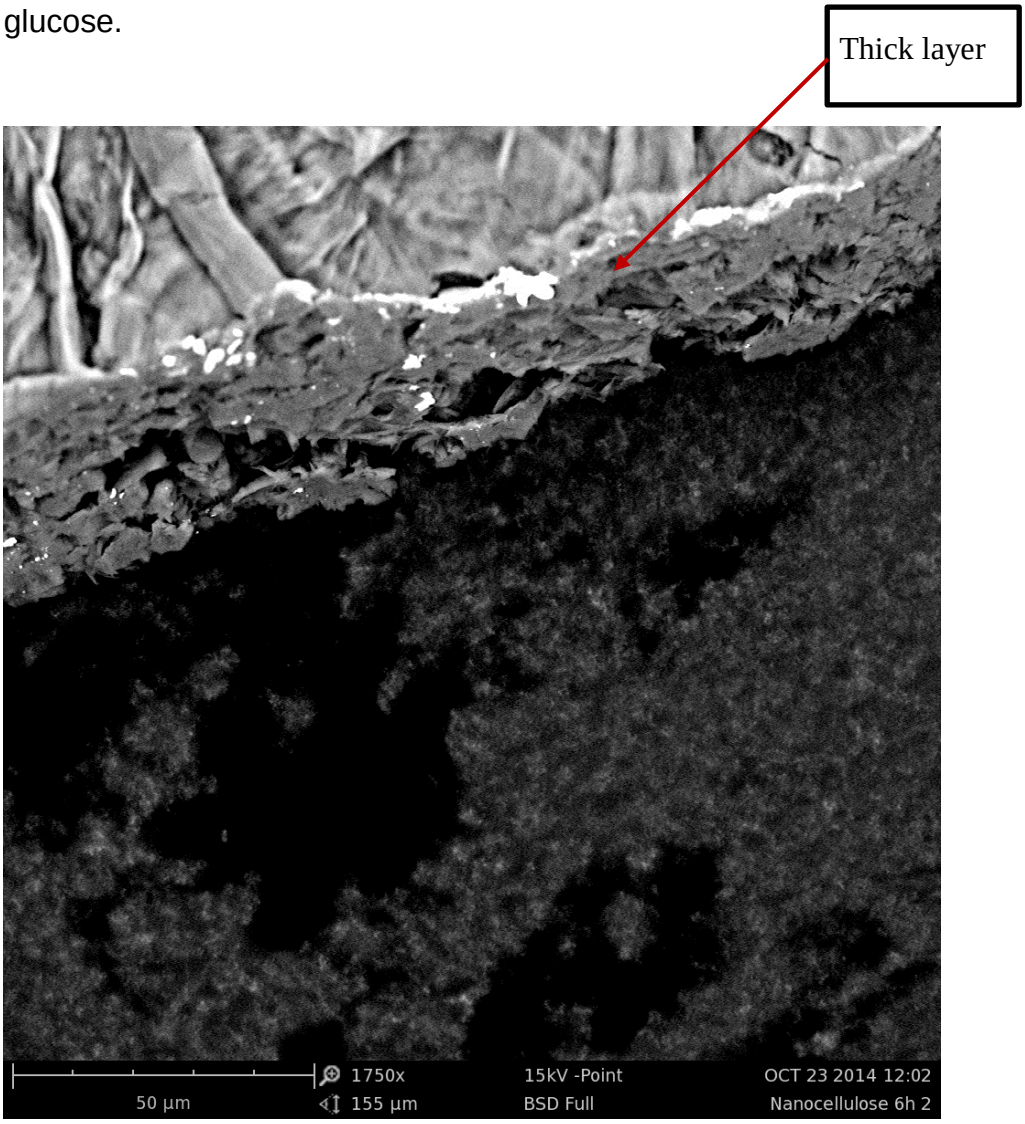


Figure 4.5: SEM image of gelled TEMPO-oxidized CNF

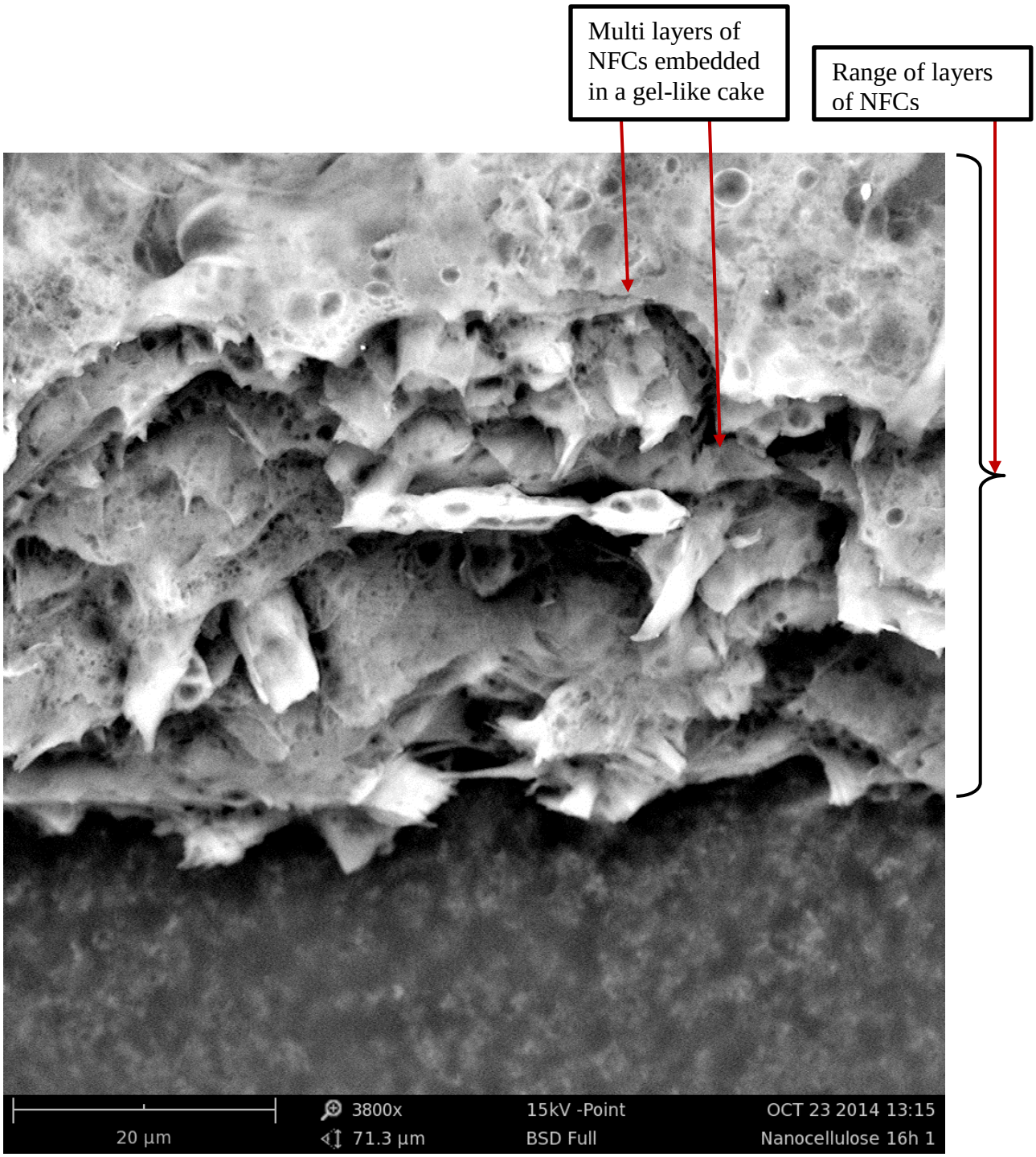


Figure 4.6: SEM showing multilayers on dried CNF

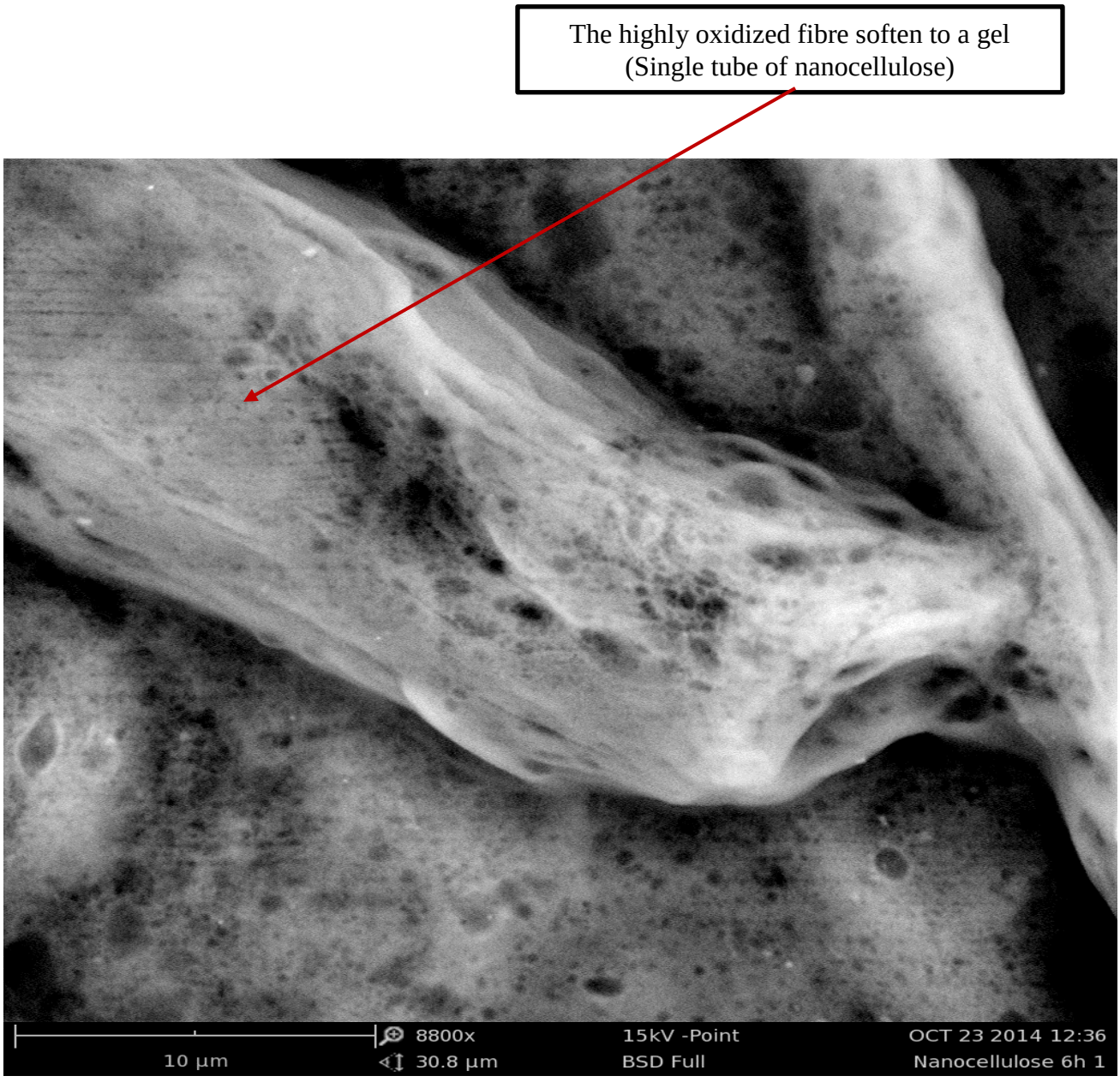


Figure 4.7: High resolution SEM image of TEMPO-oxidised CNF

4.4 Topographical image of oxidised CNF

SEM image (Figure 4.8) shows the topographical appearance of the oxidised cellulose fibre. Figure 4.8 revealed important sections on the surface of a collapsed fibre i.e. the long crystalline regions and the folded sections of amorphous (non-crystalline) regions. This topographical image displayed a real view of nanocellulose fibre that contains weak spot (amorphous region) and a strong crystalline region. The amorphous celluloses are more susceptible to chemical or mechanical treatment than the crystalline region. Production of nanocellulose through mechanical means break cellulose fibre at amorphous region; and similarly producing nanocellulose chemically expose the amorphous area to chemical attack.

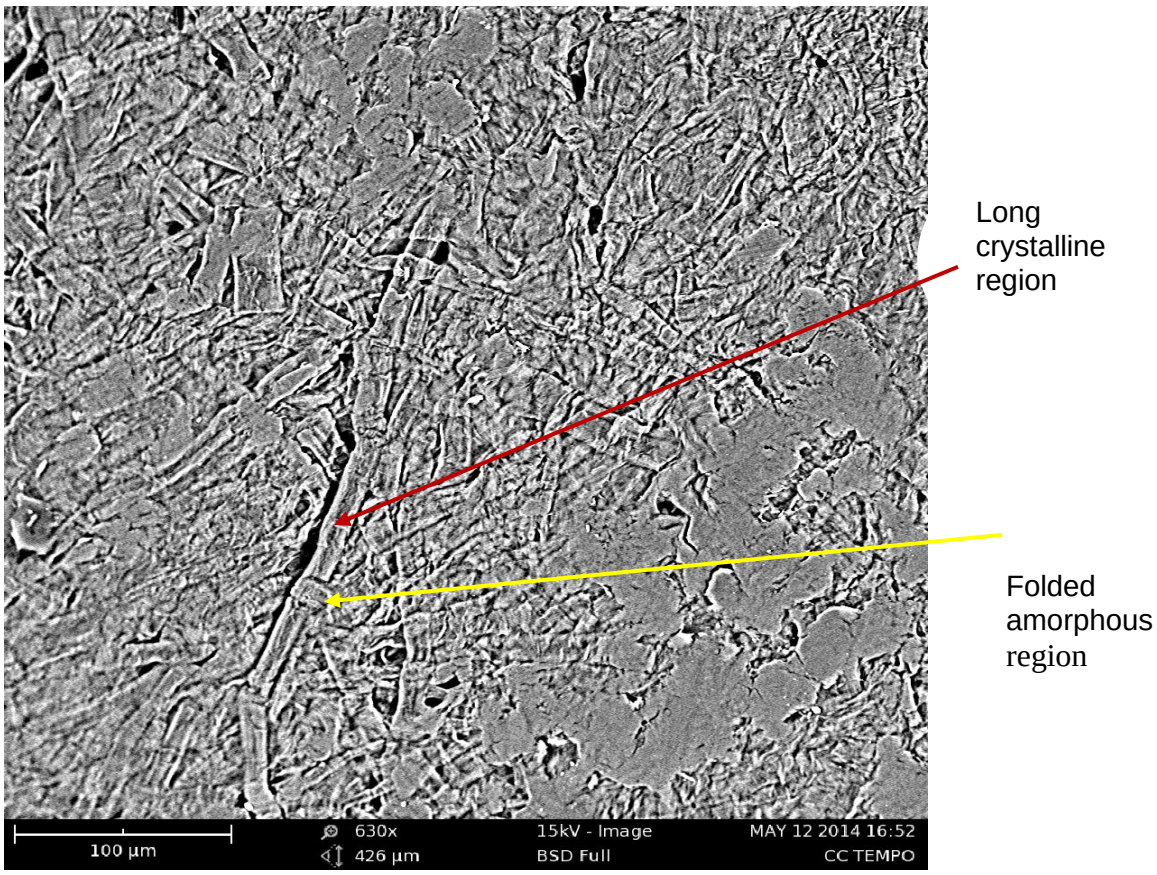


Figure 4.8: Topographical image of dried TEMPO-oxidised CNF

4.5. Characterization of oxidized cellulose using TEM

TEM images indicate numerous CNF particles with several dimensions at nano-level (Figure 4.9). As mentioned earlier under SEM characterization that it proved difficult to isolate individual nanocellulose fibre from solution because of the polymerization that takes place during the drying or evaporation process. From the image (Figure 4.10) it was observed that nanofibres tend to aggregate themselves into bigger “cloud-like” material. When the fibres agglomerate and form a dense mass the TEM image looks darker and opaque compared to a more transparent image of less aggregated nanofibres (Figure 4.10). The agglomeration was caused by hydrogen bonding between adjacent oxygen (partially negative) and hydrogen atoms (partially positive) of the adjacent polymer chains. During the TEMPO-oxidation the primary alcohol is oxidized to an aldehyde that has a partial positive (carbocation). The carbocation will have an affinity to highly negative oxygen on the surroundings. Therefore within this system repolymerization is inevitable. From the TEM images (Figures 4.9 and 4.10), it was observed that the dimensional sizes of the oxidized cellulose were at nano-level (as agglomerated cellulose had also nano-size dimension). The aggregation of the nanocelluse fibres was a result of the hydrogen bonding and the generated positive carbocations, which attracted the negatively charged oxygen atoms from the adjacent hydroxyl groups. The nanocellulose was produced at a concentration of 2% in water, and it was enriched up to 10% by centrifugation. Concentrated nanocellulose gave dark TEM images as seen in Figures 4.9 and 4.10.

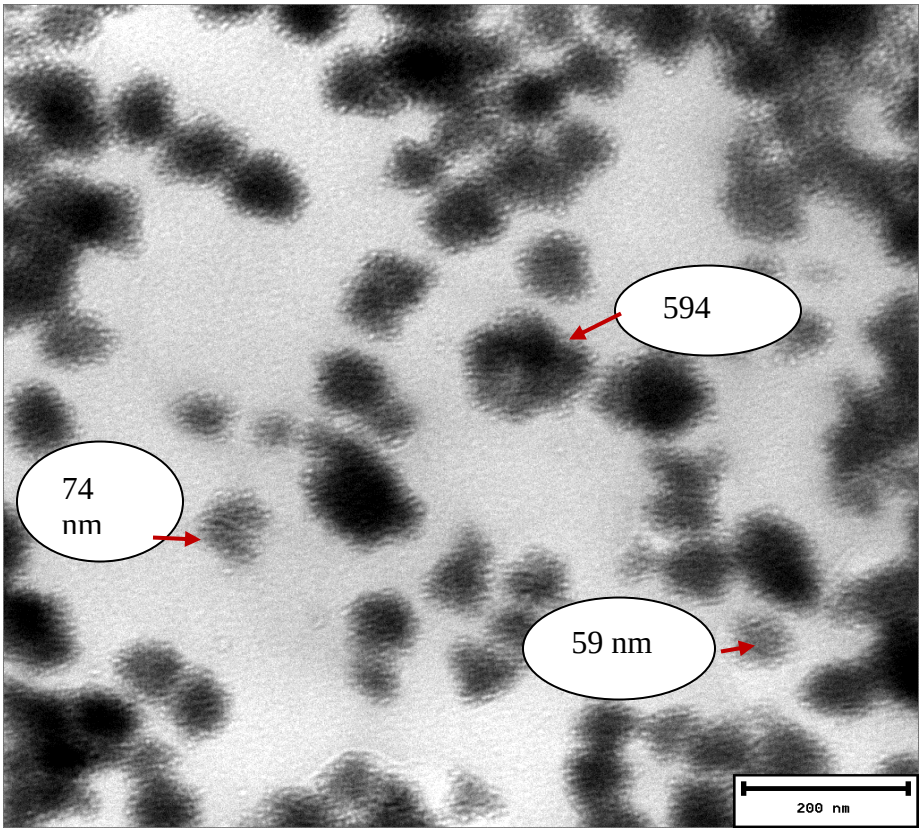


Figure 4.9: TEM image of re-polymerised CNF

In Figure 4.10, few “clouds” of CNF aggregates and individual wool-like strands were observed. Small spacing within the CNF “cloud” which separated the strands of the repolymerising nanofibres was observed. These individual strands are as small as 1.4 nm and below as shown in the TEM image Figure 4.10.

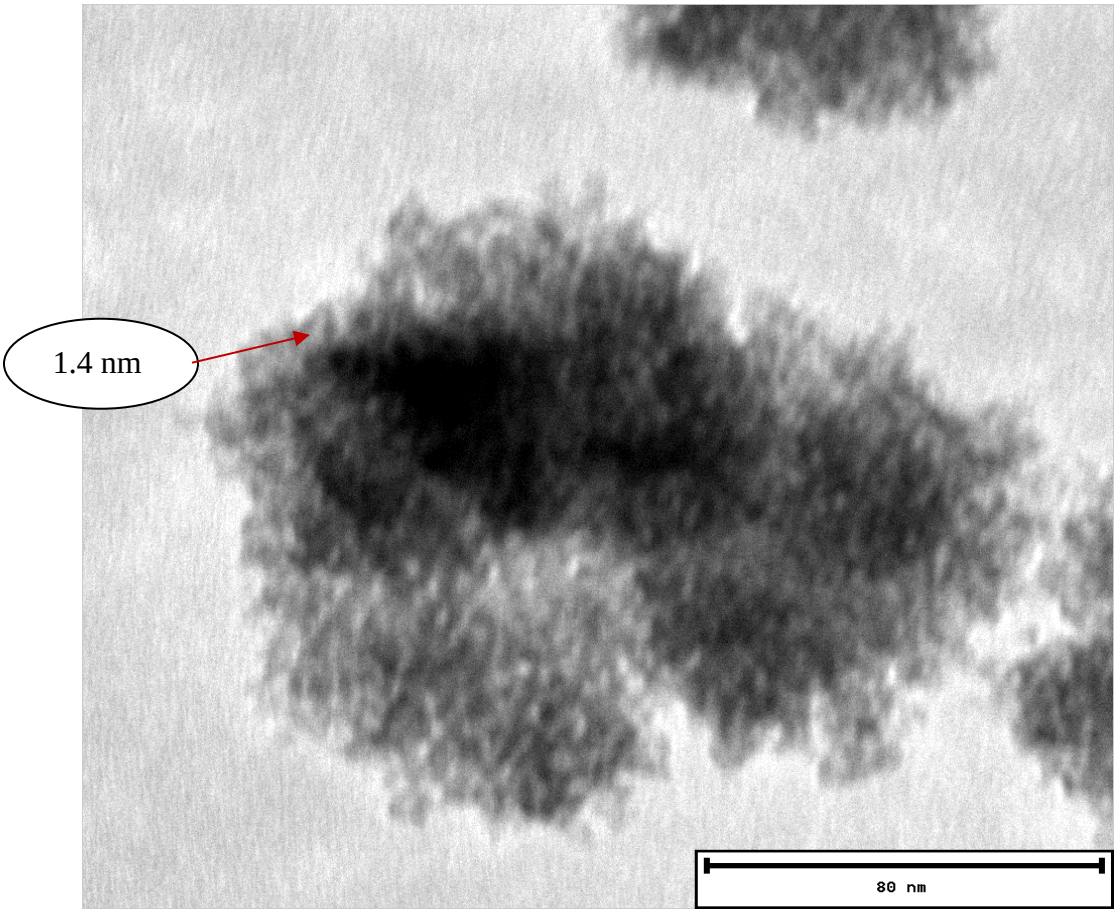


Figure 4.10: A “cloud” of CNF aggregating fibres

4.6 Characterization of CNF using FTIR

FTIR spectrum of the un-oxidized fibrillated cellulose (Figure 4.11) showed two prominent peaks at 3338.15 and 2885.64 wavenumbers characteristic of –OH (alcohol groups) vibrational frequencies. There was a missing peak between 1720 to 1740 cm^{-1} wavenumbers that is characteristic of –C=O (carbonyl) stretch band (Costa et al., 2015; Rosli et al., 2013). The carbonyl stretch peak was observed on FTIR spectrum (Figure 4.12) of the TEMPO-mediated oxidation of fibrillated cellulose. The peak that developed at 1720 to 1740 cm^{-1} wavenumbers confirmed the oxidation of the primary alcohol groups to aldehydes. There was no further change in the observed structure of the cellulose other than peak at 1720 to 1740 cm^{-1} and it is assumed that there was no further oxidation beyond the aldehyde stage as there was no carboxylic stretch bands observed (Costa et al., 2015; Rosli et al., 2013).

When the concentration of NaOCl was halved, keeping the concentrations of other chemicals constant, the carbonyl stretch peak at 1720 to 1740 cm-1 was dramatically reduced in size (Figure 4.13). This suggested that this oxidation process of CNF is driven by the concentration of the NaOCl. When the concentration of NaBr was halved but maintaining the concentrations of other chemicals constant, it was observed that the carbonyl stretch peak at 1720 to 1740 cm^{-1} remained unaltered (Figure 4.14). This suggested that at halved concentration, the NaBr catalyst is sufficient to perform its catalytic function. When the concentration of NaOCl was doubled it was observed that carbonyl stretch peak slightly increased (Figure 4.15). When the concentration of NaBr was doubled it was observed that a second peak developed at the slightly upper wavenumbers approximately 1760 cm^{-1} (Figure 4.16). This peak or stretch is a carboxylic carbonyl stretch; the increase in NaBr concentration by doubling the concentration accelerated the oxidation of some of the aldehydes group to carboxylic acid group. This was not observed with the change in concentrations of NaOCl.

The carbonyl peak not observed 1598.33 cm^{-1}

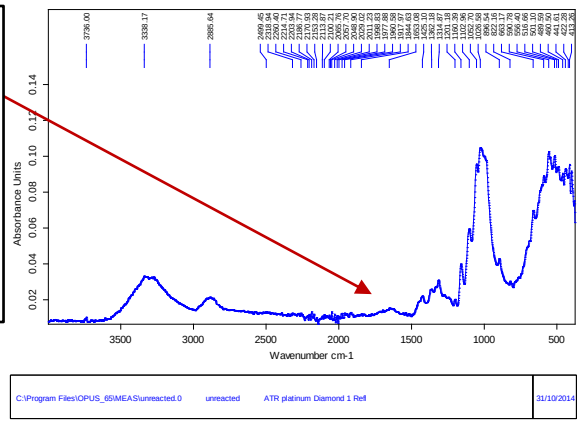
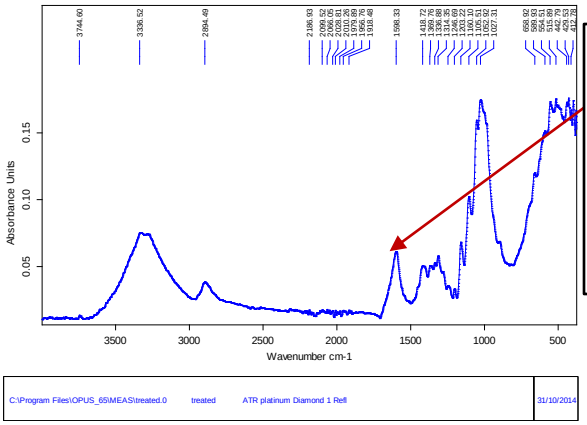


Figure 4.11: FTIR spectrum of the un-oxidized cellulose



The carbonyl peak produced a peak at +/- 1598.33 cm^{-}

Figure 4.12: FTIR spectrum of oxidized cellulose after six hours

The carbonyl peak at 1720 to 1740 cm^{-1} reduced

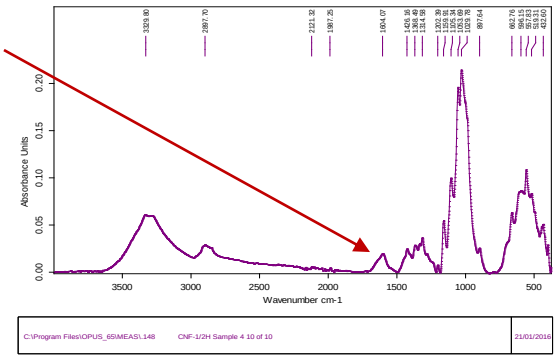
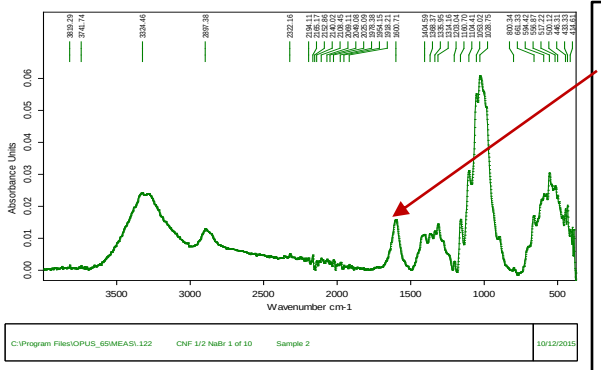


Figure 4.13: FTIR spectrum of cellulose when the NaOCl concentration was halved



The oxidation of cellulose peak at +/- 1720 to 1740 cm^{-1} remained

Figure 4.14: FTIR spectrum of cellulose when the NaBr concentration was halved

Doubling the NaOCl increased the peak at +/- 1720 to 1740 cm^{-1}

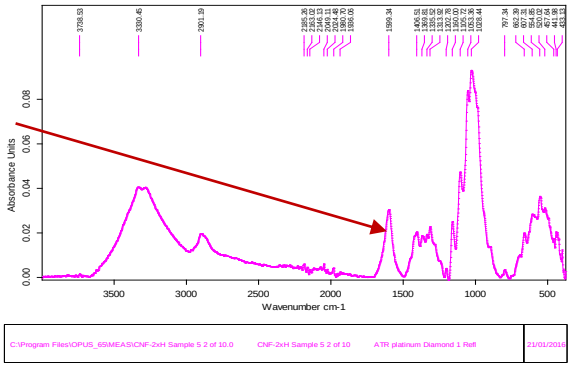
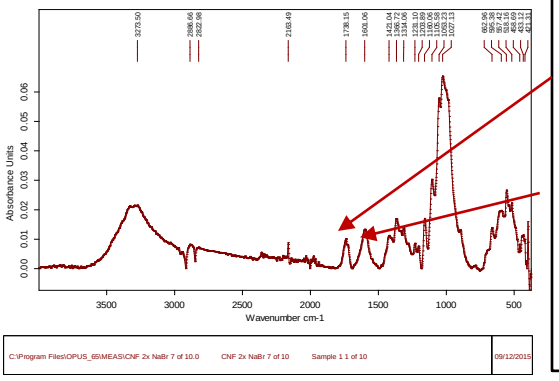


Figure 4.15 Spectrum of cellulose when the NaOCl concentration was doubled



Doubling NaBr developed two peaks at +/- 1720 to 1740 cm^{-1}

Figure 4.16: Sspectrum of cellulose when the NaBr concentration was doubled

4.7 Characterization of the CNF with tensile tester

The tensile strengths results showing the impact of changing chemical concentrations are tabulated on table 4.1. It can be seen that the tensile strength of the produced CNF was very high for both chemicals used. Increasing the concentration of NaOCl and NaBr, reduce the tensile strength of the produced CNF. Halved NaBr enhanced the strength of CNF compared to NaOCl. Below are more discussion on the effect of chemical concentration of NaBr and NaOCl.

Table 4.1: Tensile strengths results of different CNF samples

Tensile of standard procedure NaOCl & NaBr	Tensile of Doubled NaOCl	Tensile of Halved NaOCl	Tensile of Doubled of NaBr	Tensile of Halved NaBr
kN/m	kN/m	kN/m	kN/m	kN/m
4.40	5.52	5.09	3.38	7.97
3.20	3.78	5.05	3.73	9.77
5.08	1.92	4.55	4.58	7.22
4.18	2.85	4.16	3.45	7.92
4.13	5.63	4.25	3.79	10.0
44.74	2.90	3.34	3.46	6.47
4.25	3.41	5.36	0.63	8.49
4.82	1.99	4.82	1.92	4.75
5.95	4.11	3.81	1.32	2.81
Average 4.51	**Average 3.57**	**Average 4.63**	**Average 2.92**	**Average 6.81**

4.7.1 Statistical analysis of CNF tensile with different NaOCl concentration

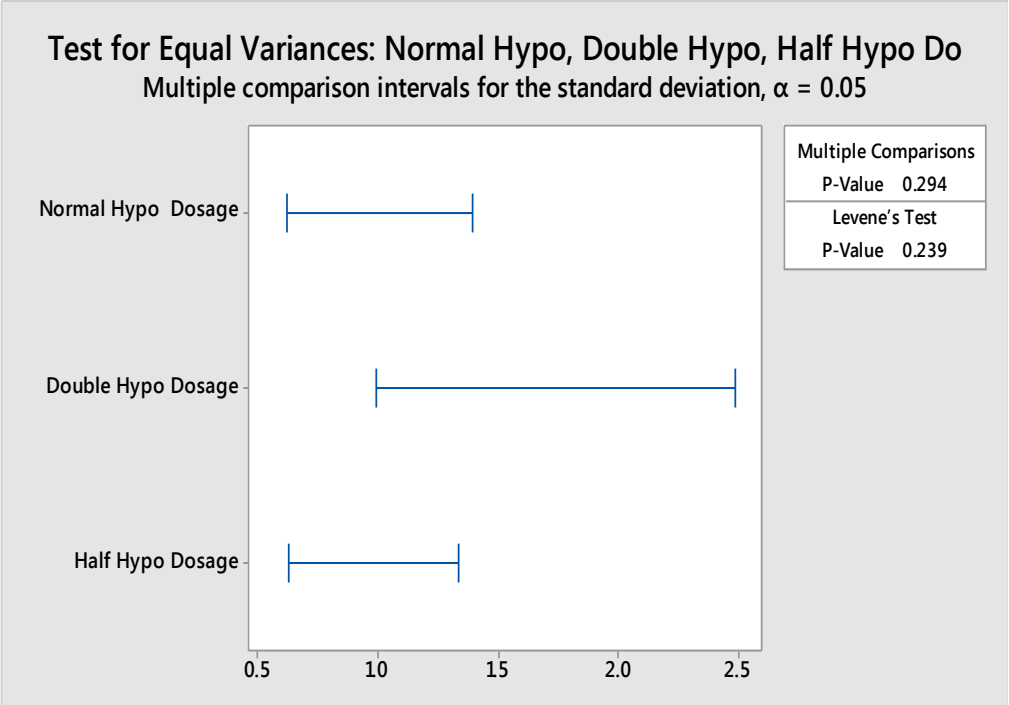


Figure 4.17: Comparisons of CNF tensile with varied NaOCl concentration

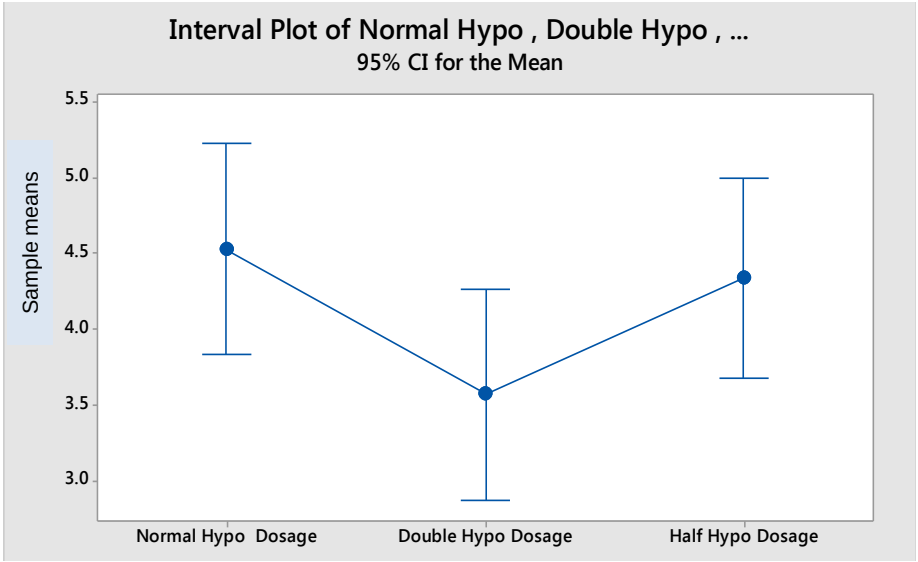


Figure 4.18: Interval plot of CNF tensile with varied NaOCl concentration

4.7.2 Discussion of the results of varied NaOCl concentration

The results showed that when NaOCl concentration was halved or doubled the multiple comparisons intervals overlapped (Figure 4.17) which meant that there was no significant difference between the tensile strengths based on the difference in Hypochlorite concentrations (Dai et al,. 2014; Rodríguez-Castellanos et al. 2015). The overall multiple comparison p-value was found to be 0.123 which is greater than 0.05. This also confirmed that there was no statistical significant difference between the standard deviations of the means of all concentrations of hypochlorite (Figure 4.18). Therefore the Null Hypothesis was accepted which stated that “all means are statistically equal” and the Alternate Hypothesis were rejected. Plots of probabilities of hypochlorite means are attached in Appendix (Figures B.18 to B.23). Different sodium hypochlorite concentrations did not yield any noticeable increase or decrease in tensile strengths of the CNF material. It was observed (Figure 4.18) that the doubled sodium hypochlorite concentration slightly reduced the tensile strength of the CNF material. The result suggested that the doubled sodium hypochlorite concentration had aggressive oxidation action on CNF and most of nanofibrils were dissolved into gel as shown by the SEM image (Figure 4.19). The presence of nanofibrils (Figure 4.20) seemed to perform interlock function between the nanoparticles and hence assist in strength improvement. This was observed when the microfibrils were partially oxidised as was the case with halved NaBr catalyst (Figure 4.24) (Dai et al,. 2014; Rodríguez-Castellanos et al. 2015).
.



Figure 4.19: SEM image of CNF produced from doubled NaOCl.

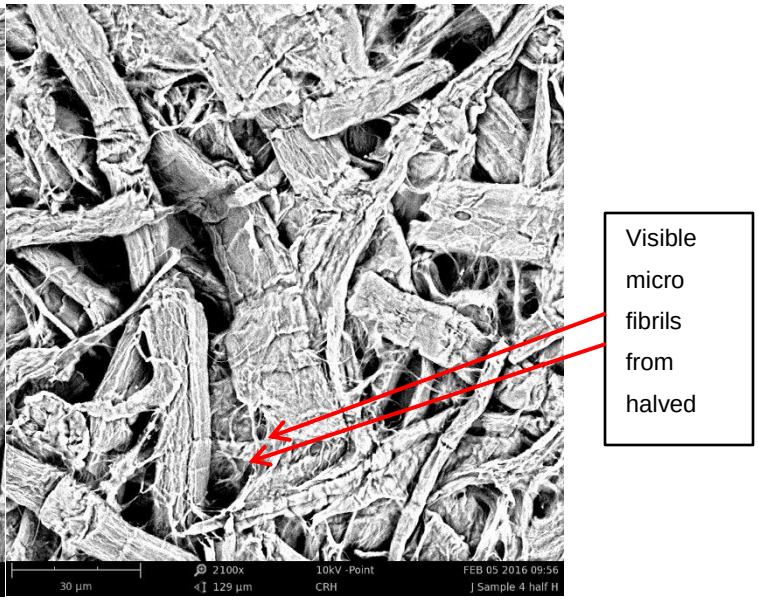


Figure 4.20: SEM image of CNF produced from halved NaOCl

4.7.3 Discussion of the results of varied NaBr concentration

Results obtained after varying NaBr concentrations are shown in Figures 4.21 and 4.22. There was no overlap of multiple intervals between normal and halved concentrations of bromide (Figure 4.21) i.e. the corresponding standard deviations was significantly different. Therefore there was significant difference between the tensile strengths of the normal bromide and halved bromide tensile strengths. The pooled multiple comparison p-value of the CNF means was found to be 0.029, which was smaller than α of 0.05. That meant that there was at least one mean that was statistical different from the means of CNF tensile strengths produced from different concentration of NaBr (Figure 4.21). From the interval plot (Figure 4.22) it was observed that there was no overlap between the standard deviations of the means of halved NaBr and doubled NaBr. From these results the Null Hypothesis was rejected and the Alternate Hypothesis accepted that “At least one mean was statistically different”. Plots of probabilities of NaBr means are attached in Appendix (Figures B.1 to B.8). The rate of

cellulose oxidation process appeared to be driven by both the concentration of NaOCl (oxidant) and NaBr (co-catalyst) (Rodríguez-Castellanos et al. 2015). The disappearance of fibrils and the formation of CNF gel were observed with doubled concentration of NaOCl and doubled concentration of NaBr (Figures B.11 and B.31). The presence of nanofibrils was still visible with halved concentrations of NaOCl and NaBr. However it was also observed that the presence of nanofibrils was more prominent with halved NaOCl than in NaBr (Figures 4.19 and 4.24). This provided some explanation why the doubled concentration had lower tensile strengths (the absence of fibrils) than the halved concentrations.

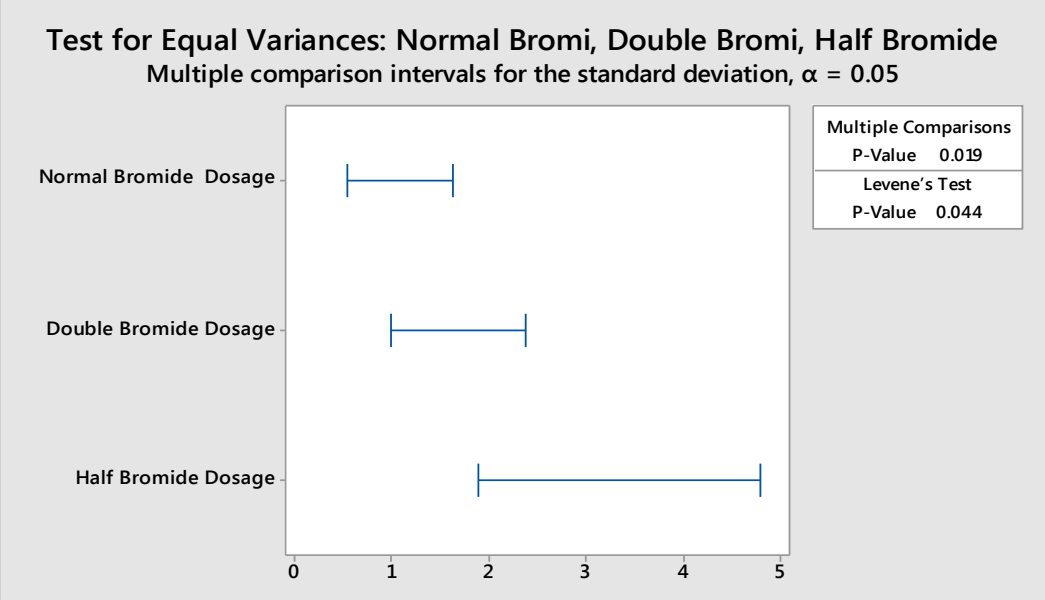


Figure 4.21: Comparison of CNF tensile strengths with varied NaBr

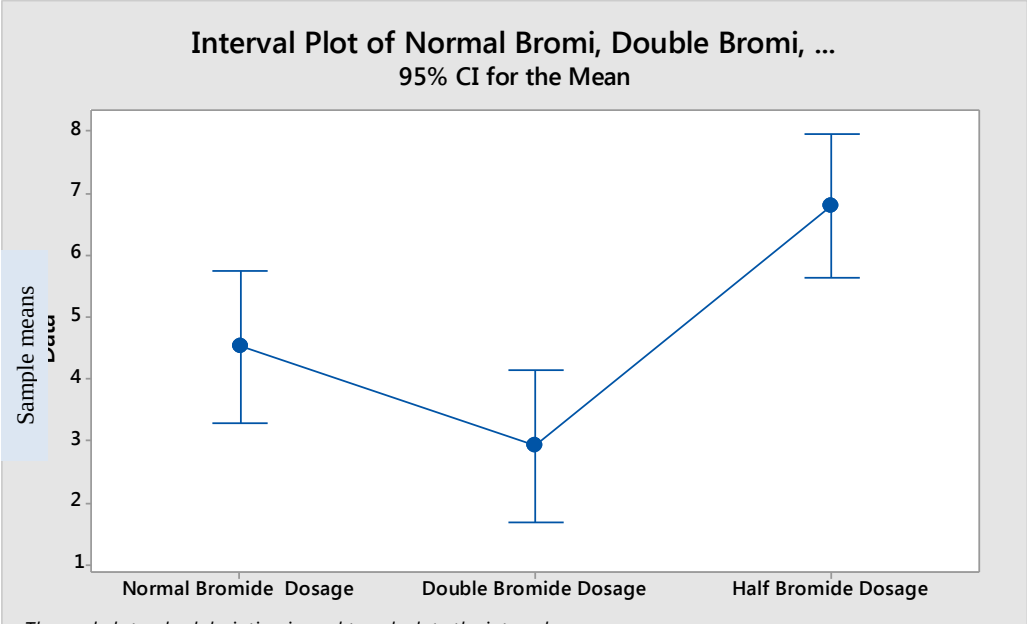


Figure 4.22: The interval plot of CNF tensile strengths with varied NaBr concentration.

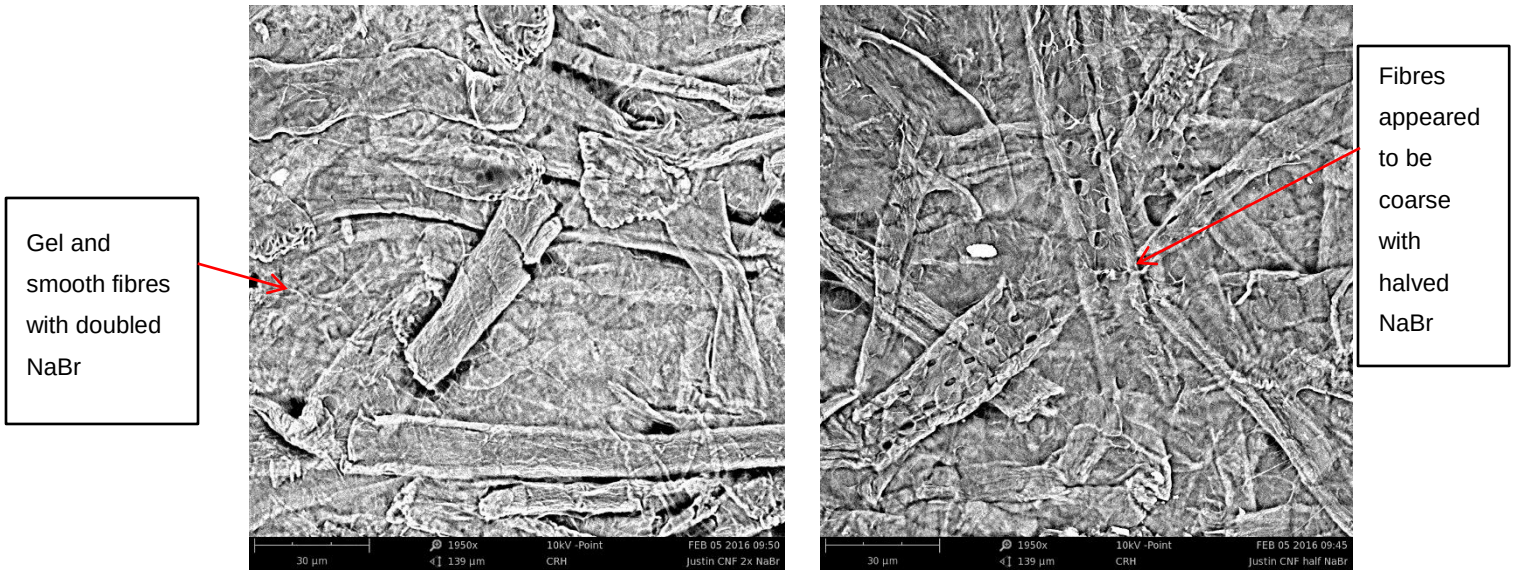


Figure 4.23: SEM image of CNF produced from doubled NaBr concentration

Figure 4.24: SEM image of CNF produced from halved NaBr concentration

4.7.4: Electrical resistance tests of oxidized CNF and rGO paper

The images of the control CNC paper (oven dried TEMPO-oxidised *E.grandis* pulp) and the conductive CNC/Cu^{2+}/rGO]n paper (oven dried TEMPO-oxidised *E.grandis* pulp) treated with reduced graphene oxide) are shown on Figures 4.25 and 4.26 respectively.



Figure 4.25: Dried sheet of TEMPO-oxidised CNF



Figure 4.26: Dried sheet of TEMPO-oxidised CNF treated with rGO

It was observed that the colour of the CNC/Cu^{2+}/rGO]*n* paper was somewhat greyish-to-black as a result of the colour of Graphene Oxide and hydro-iodic acid (greyish to black liquids). Both the control paper strips and the [CNF/Cu^{2+}/rGO]*n* paper strips (test samples) were tested for electrical resistance using the Multimeter. Three paper strips with dimensions of 4 mm width and 20 mm in length were cut from each sample and tested for resistance. The results of the resistance measurements of the control sample are on Table 4.2. From these results it was observed that the untreated paper strip had very high resistivity. The results of the resistivity measurements of CNF/Cu^{2+}/rGO]*n* (reduced Grapheme Oxide treated paper) are on Table 4.3.

Table 4.2: Electrical resistance measurements of the TEMPO-oxidised paper

Control sample	Resistivity/ (MΩ)	Strip width (m)	Strip length (m)	Remarks
Replica 1	Infinity	0.004	0.005	Very large
Replica 2	Infinity	0.004	0.010	Very large
Replica 3	Infinity	0.004	0.015	Very large

Table 4.3: Electrical resistance measurements of CNF/Cu^{2+}/rGO]*n* paper

Control sample	Average R/ MΩ	Strip width/ m	Strip height/ m	Strip length/ m	Strip area/ m^2	Resistivity (ρ)/ Ω.m	Conductivity 1/ρ/ ($Ω^{-1}m^{-1}$)
1	1.1	0.004	0.0001	0.005	$4x10^{-7}$	88	0.011
2	1.2	0.004	0.0001	0.01	$4x10^{-7}$	48	0.021
3	1.5	0.004	0.0001	0.015	$4x10^{-7}$	40	0.025

When the paper was coated with reduced Graphene Oxide, the resistivity was reduced. The resistivity results were used to calculate the electrical conductance of the CNF paper. The calculated resistivity and conductivity were in agreement with the equation 2.3 in sections 2.3 (The resistivity was inversely proportional to the strip length). The conductance was calculated from equation 2.4.

The resistance R is proportional to the length L of the conductor for a fixed area. Resistivity ρ is the property of material that causes resistance to the flow of current. Because the dimensional parameters of a semi-conductor (paper strip) were known then the conductivity σ was calculated from resistivity. It was impossible to repeat the experiment because there was not sufficient graphene oxide available.

The graph below (Figure 4.27) shows the relationship that was observed between the resistivity and conductivity of the semi-conductive strip of paper with increasing length. From the graph it was demonstrated that when the length of the strip of paper was extended, the conductivity also increased in line with the equation $R = \rho\frac{L}{A}$. as discussed on the previous section.

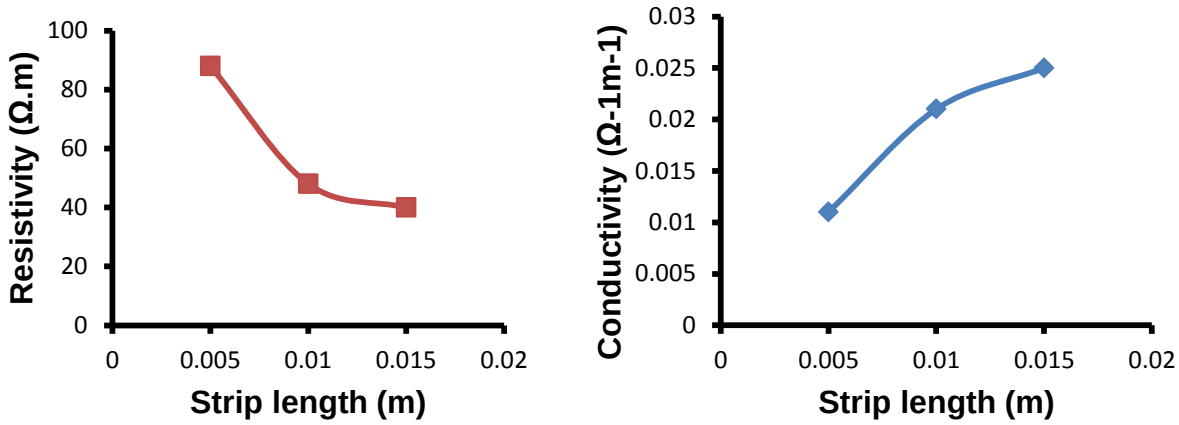


Figure 4.27: GraphS of the resistivity against strip length

Chapter 5: Conclusions and Recommendations

5.1 Conclusions

The morphological fibre widths of the starting and mechanically refined *E.grandis* pulp were determine by TECHPAP Morfi MWT instrument. The average unrefined pulp had cell wall widths of 3.18 microns. The average cell widths of the refined fibres were 3.07 microns. The SEM images also show the condition of the fibres before and after mechanical treatment. The SEM and TEM images of the TEMPO-oxidized pulp showed that the *eucalyptus grandis* pulp was successfully synthesised to cellulose nanofibre (CNF) under the conditions of the experiment. From SEM images, it was observed that on drying, the CNF repolymerised into a nanogel. When the TEM images were investigated it was observed that microfibrilated cellulose (MFC) was reduced to CNF with the dimensions ranging from 1.4 nm to 594 nm (nanoscale).

The FTIR spectra revealed that the TEMPO/NaBr/NaOCl oxidation did not go beyond aldehyde stage. The new absorbance peak that was developed at wavenumber 1720 to 1740 cm^{-1} was not present on the spectrum of the un-oxidised pulp. This new peak was a characteristic of the carbonyl stretch of the aldehyde functional group. Although the pH was decreasing during the oxidation of primary of alcohol, this was caused by the generation of the hydrochloric acid from the NaOCl and the removal of the hydrogen ion from the alcohol functional group of the carbohydrate. This peak also confirms that the TEMPO targets the terminal primary alcohols. When the NaOCl concentration was halved a decrease of the carbonyl stretch peak was observed. When the NaOCl concentration was doubled an increase of the carbonyl stretch peak was observed. When the concentration of NaBr co-catalyst was halved there was no change on the carbonyl stretch peak observed. When the concentration of NaBr co-catalyst was doubled a second peak developed at +/-1760 cm^{-1} wavenumber that is suggested to be

a carboxylic carbonyl stretch. It seems that the oxidation reaction of the alcohol of cellulose to aldehydes is also driven by the concentration of NaOCl.

The Standard Laboratory Hounsfield Tensile Tester for measuring the strength of paper samples was used to measure the tensile strength of the oxidized and dried paper strips prepared at different concentrations of NaOCl and NaBr. The results of the doubled and halved sodium hypochlorite did not show any significant difference in tensile strength at 95% confidence limit. The results of the halved sodium bromide showed significant higher tensile strength for the halved bromide concentration than doubled sodium bromide. The higher strength of the halved sodium bromide could be attributed to the partial oxidation of MFC, which lead to overlapping and crosslinking during the formation of a paper. The normal sodium bromide tensile strength was not significantly different from halved bromide strength. When formulating for stronger CNF paper consider partial oxidation of the cellulose pulp.

Two sets of translucent paper films were prepared from the washed and dried nanocellulose gel. Three control paper films of different lengths were not coated with the reduced graphene oxide solution. The other three paper films were coated with graphene oxide and the graphene oxide was reduced with iodide ions to make it more negative. The reason to prepare few strips of paper was a constraint caused by the little quantity of graphene oxide that was available. The yellowish translucent film is an image of the untreated film. The greyish dark film is graphene oxide treated film. The multimeter was used to measure the resistance of the films. The results of the control paper showed that the untreated paper had a very high electrical resistance which is characteristics of wood. The meter gave the resistance reading to the infinity. The results of the graphene coated paper showed that the high electrical resistance of paper had been reduced to at least semi-conductor level. The resistivity of untreated pulp was very large and the conductivity could not be calculated. The resistivity of the coated paper was converted using a formula and found to be 2.27×10^{-4} $m^{-1,}$ 2.08×10^{-4} m^{-1} and $1.67 \times 10^{-4}\Omega^{-1}.m^{-1}$ depending on the length of the strip which is in line with the fact that says; conductivity is inversely proportional to length and directly proportional to area.

In conclusion the objectives of the Research Project were met and the positive results were achieved. It is hoped that this fundamental work in the area of electrical conductive polymers reinforces and adds some valuable information to a much already explored research area.

5.2 Recommendations

Based on this project the following recommendations are made:

- The project should explore other oxidizing agents such as Hydrogen peroxide, Ozone, Chlorine dioxide, Etc. and optimised
- More other organic materials should be explored
- The current challenge of scaling up the production of the CNC should be tackled
- The application area of the nanocellulose products should be investigated to make use of the opportunity of the abundance of trees provided by Mother Nature.

References

Atkins, P. & de Paula, J., (2010). Materials 1: macromolecules and self-assembly. In: P. Artkins & J. De Paula, eds. *Physical Chemistry.* Portland: Oxford University Press, pp. 659-667.

Brinchi, L. I., Cotana, F., Fortunati , E. & Kenny., J. M., (2013). Production of nanocrystalline cellulose from lignocellulosic biomass: technology and applications. *Carbohydrates Polymers,* 94(1), pp. 154-169.

Brodin, F. W. & Theliander, H., (2012). Absorbent matewrials based on kraft pulp: preparation and material characterization. *BioResources,* 7(2), p. 1666.

Costa, L.A., Fonseca, A.F., Pereira, F.V. and Druzian, J.I., 2015. Extraction and characterization of cellulose nanocrystals from corn stover. *Cellulose Chemistry And Technology*, *49*, pp.127-133.

Dai, L., Long, Z., Lv, Y. and Peng, Q.C., 2014. The role of formic acid pretreatment in improving the carboxyl content of TEMPO-oxidized cellulose. *Cell Chem Technol*, *48*(5-6), pp.469-475.

Dominique MOINEAU, (2014). Morfi Wall Thickness. *techpap innovation for paper*

Farag S. A.H et al., (2015). Synthesis and structure of high quality graphene prepared via solvothermal exfoliation of intercalated graphite flakes. *Superlattices and Microstructures,* 86(2015), pp. 270-274.

Gao, K et al., (2013). Cellulose nanofibres/reduced graphene oxide flexible transparent conductive paper. *Carbohydrate Polymers,* 97(1), pp. 243-251.

Gibson, L. J., (2012). The hierarchical structure and mechanics of plant materials. *J. R. Soc. Interface,* 9(76), pp. 2749-2766.

Heeger, A. J., Kivelson, S., Skrieffer, J. R. & Su, W. -P., (1988). Solitons in conducting polymers. *Reviews of Modern Physics.,* 60(3), p. 781.

Immelman A et al., (2015). Tree farming Guidelines for private growers - Part 2 Siviculture. In: J. Jansen, ed. *Tree farming Guidelines for private growers.* Cascades, RSA: Sappi Forests, pp. 3-21.

John, M. J., (2008). Biofibres and biocomposites. *Cabrbohydrate Polymers ,* Volume 71, pp. 343-364.

Khalil , J., Benoit , B., Bruno , C. & Claude , D., (2012). Characterization of conductive composite films based on TEMPO-oxidized cellulose nanofibres and polypyrrole. *Journal of Materials Science,* 47(8), pp. 3752-3762..

Khalil A. et al., (2014). Production and modification of nanofibrillated cellulose using various mechanical processes: A review. *Carbohydrate Polymers,* Volume 99, pp. 649–665.

Kirkham, M. B., (2014). Electrical Analogues for Water Movement through the Soil-Plant-Atmosphere Continuum. In: M. B. Kirkham, ed. *Principles of Soil and Plant Water Relations.* Manhattan, USA: Academic Press, pp. 391-407.

Klemm D et al., (201)1. Nanocelluloses: A New Family of Nature-Based Materials. *Angewandte Chemie International Edition,* 50(24), pp. 5438–5466.

Kuma J et al., (2012). An overview on the cellulose based conducting composite. *Elsivier,* 43(7), pp. 2822-2826.

Lange, U., (2008). Conducting polymers in chemical sensors and arrays. *Analytica Chimica Acta,* 614(1), pp. 1-26.

Li, Q.Q., 2012. Nanocellulose: preparation, characterization, supramolecular modelling, and its life cycle assessment. PhD Faculty of Virginia Polytechnic Institute & State University.

Lindström, T., Aulin, C., Naderi, A. & Ankerfors, M., (2014). Microfibrillated Cellulose. In: I. John Wiley & Sons, ed. *Encyclopedia of Polymer Science and Technology.* Stockholm: John Wiley & Sons, Inc, pp. 1-34.

MacDiarmid, A. G. & Heeger, A. J., (1980). Organic metals and semiconductors: the chemistry of polyacetylene, (ch)x and its derivatives*. *Synthetic Metals,* 1(2), pp. 101-118.

Moreno, I. & Araiza, J., (2005). Thin-film spatial filters. *Optics Letters,* 30(8), pp. 914-916.

Pandey J. K et al., (2012). An overview on the cellulose based composites. *Composites Part B: Engineering,* 43(7), pp. 2822-2826.

Rabe T et al., (2007). Suitability of lithium doped electron injection layers for organic semiconductor lasers. *Applied Physics Letters,* 90(15), p. 1103.

Razaq, A., (2011). *Develoipment of Cellulose-Based Nanostructred, Conductive Paper for Biomolecuar Extraction and Energy Storage Applications,* Sweden: Acta Universitatis Upsaliensis Uppsala.

Rodríguez-Castellanos, W., Rodrigue, D., Martínez-Bustos, F., Jiménez-Arévalo, O. and Stevanovic, T., 2015. Production and characterization of gelatin-starch polymer matrix reinforced with cellulose fibers. *Polymers from Renewable Resources*, *6*(3), p.105.

Rosli, N.A., Ahmad, I. and Abdullah, I., 2013. Isolation and characterization of cellulose nanocrystals from Agave angustifolia fibre. *BioResources*, *8*(2), pp.1893-1908.

Saito T et al., (2006). Homogeneous suspensions of individualized microfibrils from TEMPO-catalyzed oxidation of native cellulose.. *Biomacromolecules,* 7(6), pp. 1687-1691.

Salajkova, B. M., (2009). *Cellulose nanofibres and aerogels materials,* BRNO, Czech Republic: BRNO Unirvesity of Technology, Faculty of Chemistry.

Shinichiro, I., Kentaro, A. & Hiroyuki, Y., (2008). The Effect of Hemicelluloses on Wood Pulp Nanofibrillation and Nanofibre Network Characteristics. *Biomacromolecules,* 9(3), pp. 1022–1026.

Skoog, D. A., West, D. M., Holler, J. F. & Crouch, S. R., (2014). Infrared Spectrophotometers. In: S. Kiselica, ed. *Fundamentals of Analyticaal Chemistry.* Brooks/Cole: International Edition, pp. 713-719.

Songfeng , P., Jinping , Z., Jinhong, D. & Wencai , R., (2010). Direct reduction of graphene oxide films into highly. *Carbon,* 48(2010), pp. 4466-4474.

Sundararaj, J. L., (2012). *Carbon nanotubes (CNTs), being the most specialized variety among closed graphitic,* New York: Stony Brook University.

Takeshi, S., Toshika, S. & Hiromichi, W., (2013). Hydrolytic Activities of Crystalline Cellulose Nanofibres. *Biomacromolecules,* 14(3), pp. 613-617.

Valentini, L., Bon, B. S., Fortunati, E. & Kenny, J. M., (2014). Preparation of transparent and conductive cellulose nanocrystals/ graphene nanoparticles films. *Journal of Material Science,* 49(3), pp. 1009-1013.

Venon-Perry, K. D., (2000). Scanning electron microscopy: an inntroduction. *Analysis,* 13(4), pp. 40-44.

Vijay, V., Rao, A. D. & Narayan, K. S., (2011). In situ studies of strain dependant transport properties of conducting polymers in elastomeric substrates. *J. Appl. Phys. 109, 084525,* 109(8).

Wang X et al., (2013). Layer-by-Layer assembled hybrid multilayer thin film electrodes based on transparent cellulose nanofibres paper for flexible supercapacitors applications. *Journal of Power Sources,* 249, pp. 148-155.

Wegner, T. H. & Jones, E. P., (2009). A Fundamental Review of the Relationships between Nanotechnology and Lignocellulosic Biomass. In: L. A. Rojas, ed. *The*

Nanoscience and Technology of Renewable Biomaterials. Chichester, UK: John Wiley & Sons, p. doi: 10.1002/9781444307474.ch1.

Westland, J. C., (2011). Electrodermal Response in Gaming. *Journal of Computer Networks and Communications,* 2011, pp. 1-14.

Zhou Y et al., (2013). Recyclable organic solar cells on cellulose nanocrystal substrates. *SCIENTIFIC REPORTS,* 3(1536), pp. 1-5.

Appendix

Appendix A: Tables

Table A.1: Percentage distribution of cellulose MWTof the unrefined pulp

Classes [µm]	Frequency	Distribution [%]
3.09-3.11	3	20
3.12-3.14	3	20
3.15-3.17	0	0
3.18-3.20	2	13.33
3.21-3.23	5	33.33
3.24-3.26	2	13.33

Table A.2: Percentage distribution of cellulose MWTof the refined pulp

Classes [µm]	Frequency	Distribution [%]
3.00-3.02	3	20
3.03-3.05	1	6.7
3.06-3.08	4	26.7
3.09-3.11	6	40
3.12-3.14	1	6.7

Table A.3: MWT data of the unrefined *E.grandis* pulp

Tests samples	MWT results (micron)	Results mean	Difference of results & mean	Square of the differences
1	3.09	3.18	-0.08	0.007097
2	3.09	3.18	-0.08	0.0066584
3	3.09	3.18	-0.08	0.0067269
4	3.21	3.18	0.04	0.0014039
5	3.21	3.18	0.04	0.0014204
6	3.21	3.18	0.03	0.0011523
7	3.21	3.18	0.03	0.0010869
8	3.20	3.18	0.03	0.000801
9	3.18	3.18	0.00	3.527E-06
10	3.25	3.18	0.07	0.0047231
11	3.24	3.18	0.07	0.0042345
12	3.23	3.18	0.06	0.0034378
13	3.14	3.18	-0.04	0.0012377
14	3.14	3.18	-0.03	0.00106
15	3.13	3.18	-0.05	0.0024091
Average	**3.18**			
Range	**0.16**			
Variance	**0.0029**			
Standard deviation	**0.054**			

Table A.4: MWT data of the refined *E.grandis* pulp

Tests samples	MWT results (micron)	Results mean	Difference of results & mean	Square of the differences
1	3.08	3.07	0.01	0.0001215
2	3.09	3.07	0.02	0.0004128
3	3.09	3.07	0.02	0.0002621
4	3.09	3.07	0.02	0.0004099
5	3.08	3.07	0.01	0.00021
6	3.09	3.07	0.02	0.0002446
7	3.07	3.07	0.00	1.409E-09
8	3.03	3.07	-0.04	0.0014992
9	3.06	3.07	-0.01	0.000137
10	3.01	3.07	-0.06	0.0038365
11	3.00	3.07	-0.07	0.0044586
12	3.02	3.07	-0.05	0.0028929
13	3.11	3.07	0.04	0.0014179
14	3.14	3.07	0.07	0.0055087
15	3.09	3.07	0.02	0.0005374
Average	**3.07**			
Range	**0.13**			
Variance	**0.0015**			
Standard deviation	**0.038**			

Table A.5: Tensile strength of the halved NaOCl concentration

Product Code:		Temperature:	
Batch No:	CNF S4	Humidity:	
Product Type:	Handsheets	Gage Length:	90.0 mm
Operator:	Ronnie	Grammage:	N/F
		Test Speed:	10.0 mm/min
		MD / CD:	N/A
		Wet / Dry:	Dry

	Width mm	Thickness mm	Area mm²	Tensile Strength kN/m	Stretch at Break %	TEA J/m²
	15.0	N/F	N/F	5.09	1.02	25.9
	15.0	N/F	N/F	5.05	1.21	27.3
	15.0	N/F	N/F	4.55	0.73	15.8
	15.0	N/F	N/F	4.16	0.60	11.7
	15.0	N/F	N/F	4.25	1.06	26.1
	15.0	N/F	N/F	3.34	0.57	8.60
	15.0	N/F	N/F	5.36	0.87	21.6
	15.0	N/F	N/F	4.82	0.72	18.2
	15.0	N/F	N/F	3.81	0.66	11.2
	15.0	N/F	N/F	5.90	0.90	25.3
Average	15.0	N/A	N/A	4.63	0.83	19.2
SD	0	N/A	N/A	0.77	0.21	7.04
Maximum	15.0	N/A	N/A	5.90	1.21	27.3
Minimum	15.0	N/A	N/A	3.34	0.57	8.60
Range	0	N/A	N/A	2.56	0.64	18.7
Median	15.0	N/A	N/A	4.68	0.80	

Table A.6: Tensile strength of the doubled NaOCl concentration

Sile strength of

Product Code:		Temperature:	
Batch No:	CNF S5	Humidity:	
Product Type:	Handsheets	Gage Length:	90.0 mm
Operator:	Ronnie	Grammage:	N/F
		Test Speed:	10.0 mm/min
		MD / CD:	N/A
		Wet / Dry:	Dry

	Width mm	Thickness mm	Area mm²	Tensile Strength kN/m	Stretch at Break %	TEA J/m²
	15.0	N/F	N/F	5.52	0.70	19.7
	15.0	N/F	N/F	8.09	0.95	36.6
	15.0	N/F	N/F	3.78	0.47	8.02
	15.0	N/F	N/F	1.92	0.94	11.6
	15.0	N/F	N/F	2.85	0.46	3.69
	15.0	N/F	N/F	5.63	0.69	17.6
	15.0	N/F	N/F	2.90	0.50	6.97
	15.0	N/F	N/F	3.41	0.46	5.13
	15.0	N/F	N/F	1.99	0.94	11.8
	15.0	N/F	N/F	4.11	0.68	9.21
Average	15.0	N/A	N/A	4.02	0.68	13.0
SD	0	N/A	N/A	1.91	0.20	9.72
Maximum	15.0	N/A	N/A	8.09	0.95	36.6
Minimum	15.0	N/A	N/A	1.92	0.46	3.69
Range	0	N/A	N/A	6.17	0.49	32.9
Median	15.0	N/A	N/A	3.60	0.69	

Table A.7: Tensile strength of normal NaOCl concentration

Product Code:		Temperature:	
Batch No:	JNCNF	Humidity:	
Product Type:	CNF S6	Gage Length:	90.0 mm
Operator:	Refilwe	Grammage:	N/F
		Test Speed:	10.0 mm/min
		MD / CD:	N/A
		Wet / Dry:	Dry

	Width mm	Thickness mm	Area mm^2	Tensile Strength kN/m	Stretch at Break %	TEA J/m^2
	15.0	N/F	N/F	4.40	0.76	14.1
	15.0	N/F	N/F	3.20	0.57	7.41
	15.0	N/F	N/F	5.08	0.76	14.9
	15.0	N/F	N/F	4.18	0.59	10.8
	15.0	N/F	N/F	4.13	0.75	13.7
	15.0	N/F	N/F	4.74	0.78	16.9
	15.0	N/F	N/F	4.25	0.75	14.4
	15.0	N/F	N/F	4.82	0.68	14.5
	15.0	N/F	N/F	5.95	0.77	19.2
	15.0	N/F	N/F	3.71	0.69	11.5
Average	15.0	N/A	N/A	4.45	0.71	13.7
SD	0	N/A	N/A	0.76	0.07	3.27
Maximum	15.0	N/A	N/A	5.95	0.78	19.2
Minimum	15.0	N/A	N/A	3.20	0.57	7.41
Range	0	N/A	N/A	2.75	0.21	11.8
Median	15.0	N/A	N/A	4.32	0.75	

Table A.8: Tensile strength of the doubled NaBr concentration

Product Code:		Temperature:	
Batch No:	Sample1	Humidity:	
Product Type:	Hsheets	Gage Length:	90.0 mm
Operator:	Ronnie	Grammage:	N/F
		Test Speed:	10.0 mm/min
		MD / CD:	N/A
		Wet / Dry:	Dry

	Width mm	Thickness mm	Area mm²	Tensile Strength kN/m	Stretch at Break %	TEA J/m²
	15.0	N/F	N/F	3.38	0.76	11.3
	15.0	N/F	N/F	3.73	0.78	14.4
	15.0	N/F	N/F	4.58	0.93	22.0
	15.0	N/F	N/F	3.45	0.52	8.22
	15.0	N/F	N/F	3.79	0.59	9.32
	15.0	N/F	N/F	3.46	0.50	7.75
	15.0	N/F	N/F	0.63	0.29	0.871
	15.0	N/F	N/F	1.92	0.45	3.07
	15.0	N/F	N/F	1.32	0.34	1.72
Average	15.0	N/A	N/A	2.92	0.57	8.73
SD	0	N/A	N/A	1.31	0.21	6.69
Maximum	15.0	N/A	N/A	4.58	0.93	22.0
Minimum	15.0	N/A	N/A	0.63	0.29	0.871
Range	0	N/A	N/A	3.94	0.64	21.1
Median	15.0	N/A	N/A	3.45	0.52	

Table A.9: Tensile strength of the halved NaBr concentration

Product Code:		Temperature:	
Batch No:	Sample2	Humidity:	
Product Type:	Hsheets	Gage Length:	90.0 mm
Operator:	Ronnie	Grammage:	N/F
		Test Speed:	10.0 mm/min
		MD / CD:	N/A
		Wet / Dry:	Dry

	Width mm	Thickness mm	Area mm²	Tensile Strength kN/m	Stretch at Break %	TEA J/m²
	15.0	N/F	N/F	7.97	1.01	41.0
	15.0	N/F	N/F	9.77	1.21	64.5
	15.0	N/F	N/F	7.22	0.92	31.8
	15.0	N/F	N/F	7.92	1.01	42.0
	15.0	N/F	N/F	10.0	1.25	68.0
	15.0	N/F	N/F	6.47	0.76	23.6
	15.0	N/F	N/F	8.49	0.94	39.3
	15.0	N/F	N/F	4.75	0.89	20.8
	15.0	N/F	N/F	2.81	0.77	7.28
	15.0	N/F	N/F	2.65	0.70	7.76
Average	15.0	N/A	N/A	6.81	0.95	34.6
SD	0	N/A	N/A	2.63	0.18	20.9
Maximum	15.0	N/A	N/A	10.0	1.25	68.0
Minimum	15.0	N/A	N/A	2.65	0.70	7.28
Range	0	N/A	N/A	7.38	0.55	60.8
Median	15.0	N/A	N/A	7.57	0.93	

Table A.10: Tensile strength of normal NaBr concentration

Product Code:		Temperature:	
Batch No:	JNCNF	Humidity:	
Product Type:	CNF S6	Gage Length:	90.0 mm
Operator:	Refilwe	Grammage:	N/F
		Test Speed:	10.0 mm/min
		MD / CD:	N/A
		Wet / Dry:	Dry

	Width mm	Thickness mm	Area mm^2	Tensile Strength kN/m	Stretch at Break %	TEA J/m^2
	15.0	N/F	N/F	4.40	0.76	14.1
	15.0	N/F	N/F	3.20	0.57	7.41
	15.0	N/F	N/F	5.08	0.76	14.9
	15.0	N/F	N/F	4.18	0.59	10.8
	15.0	N/F	N/F	4.13	0.75	13.7
	15.0	N/F	N/F	4.74	0.78	16.9
	15.0	N/F	N/F	4.25	0.75	14.4
	15.0	N/F	N/F	4.82	0.68	14.5
	15.0	N/F	N/F	5.95	0.77	19.2
	15.0	N/F	N/F	3.71	0.69	11.5
Average	15.0	N/A	N/A	4.45	0.71	13.7
SD	0	N/A	N/A	0.76	0.07	3.27
Maximum	15.0	N/A	N/A	5.95	0.78	19.2
Minimum	15.0	N/A	N/A	3.20	0.57	7.41
Range	0	N/A	N/A	2.75	0.21	11.8
Median	15.0	N/A	N/A	4.32	0.75	

Appendix B: Figures

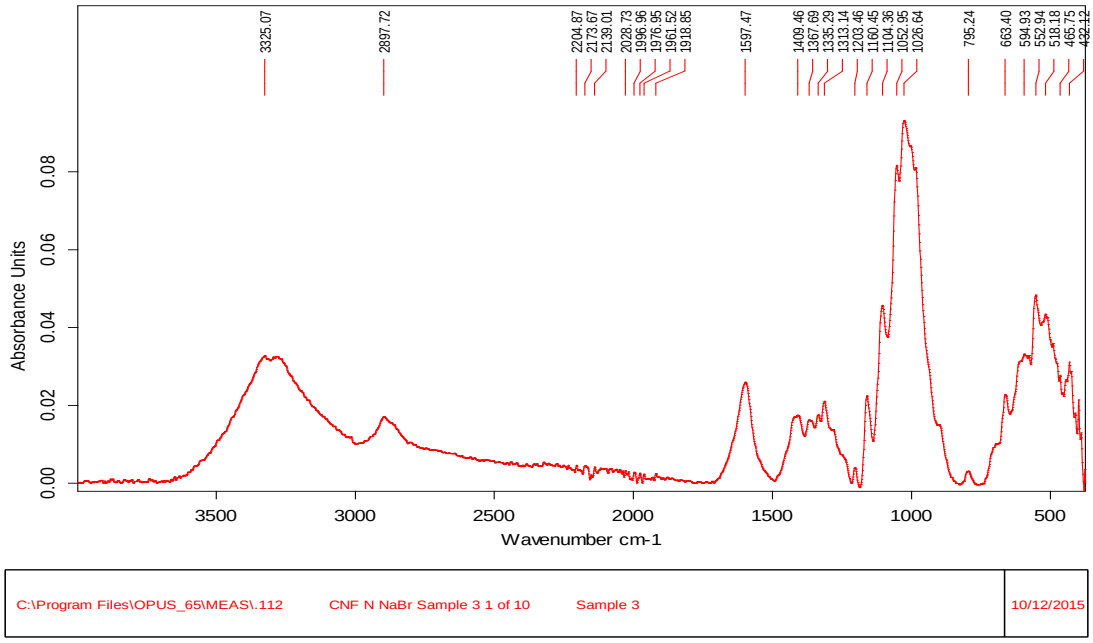


Figure B.1: FTIR Spectra of normal NaBr concentration

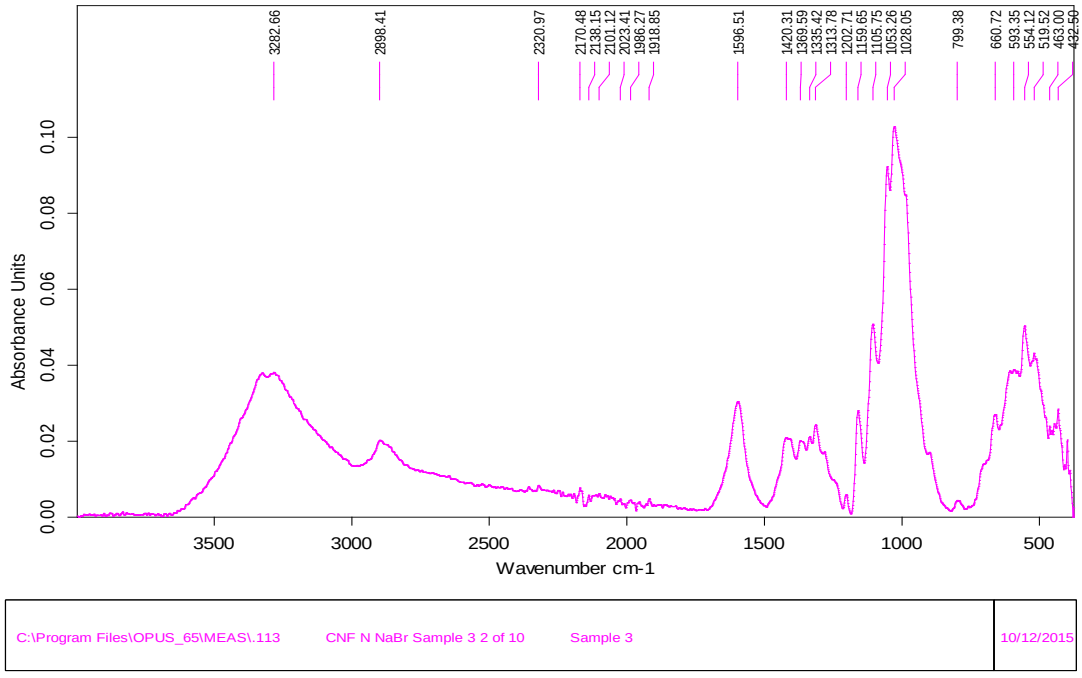


Figure B.2: FTIR Spectra of normal NaBr concentration

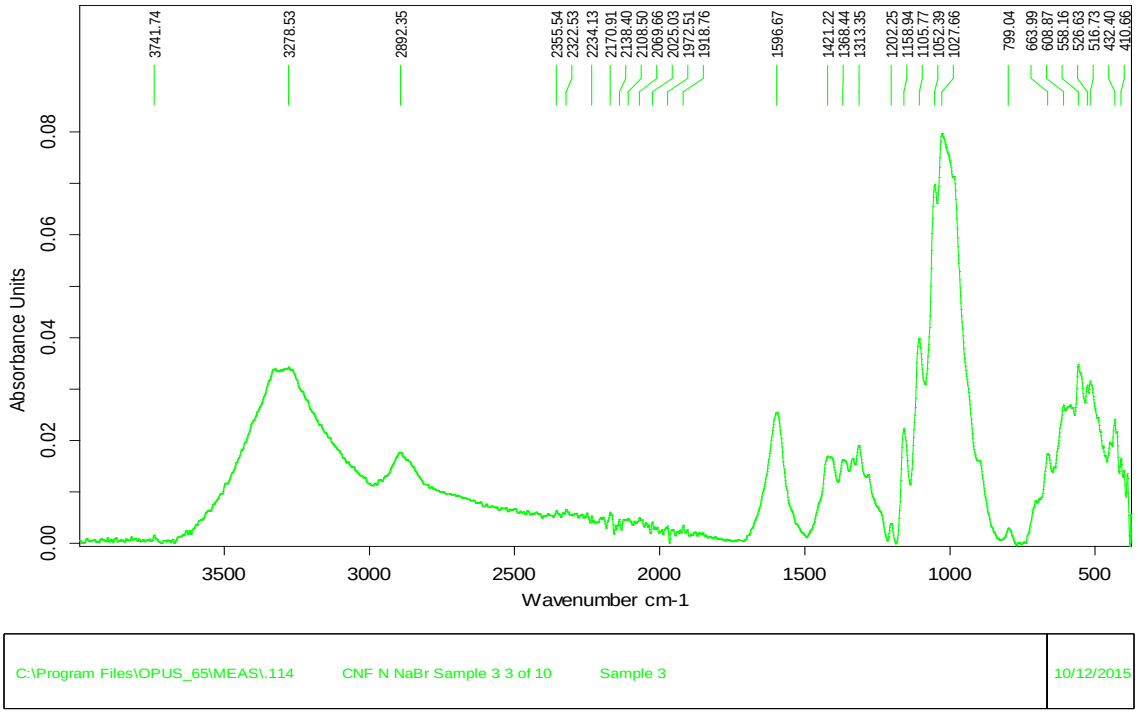


Figure B.3: FTIR Spectra of normal NaBr concentration

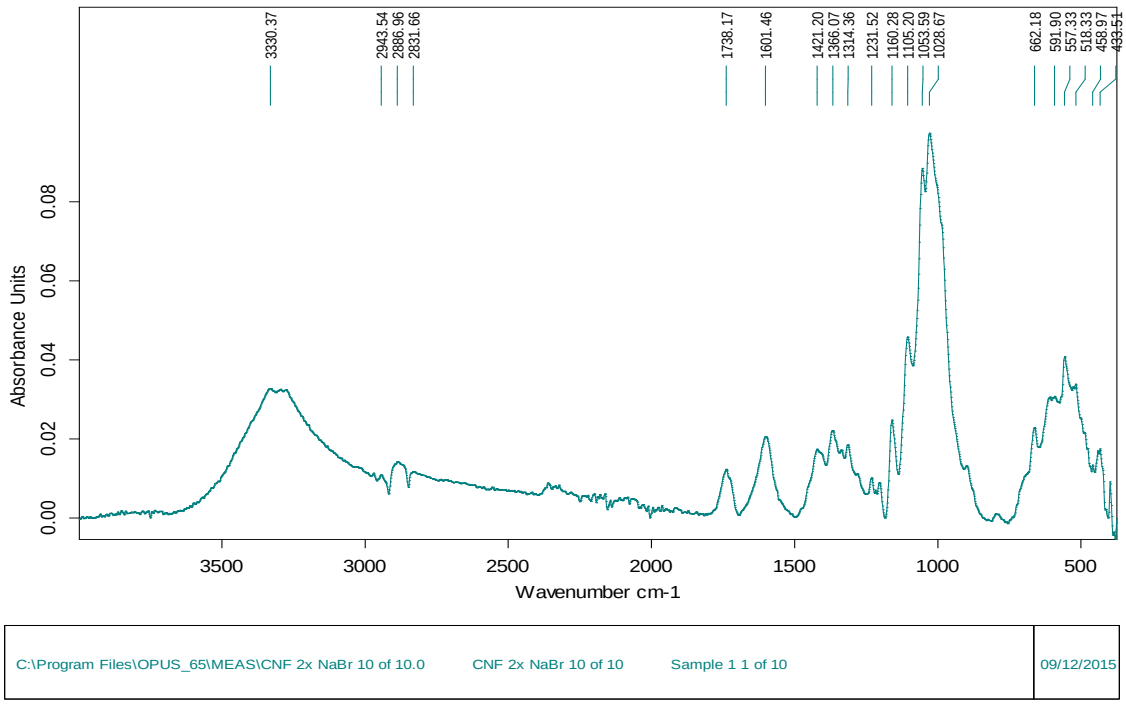


Figure B.4: FTIR of doubled NaBr concentration

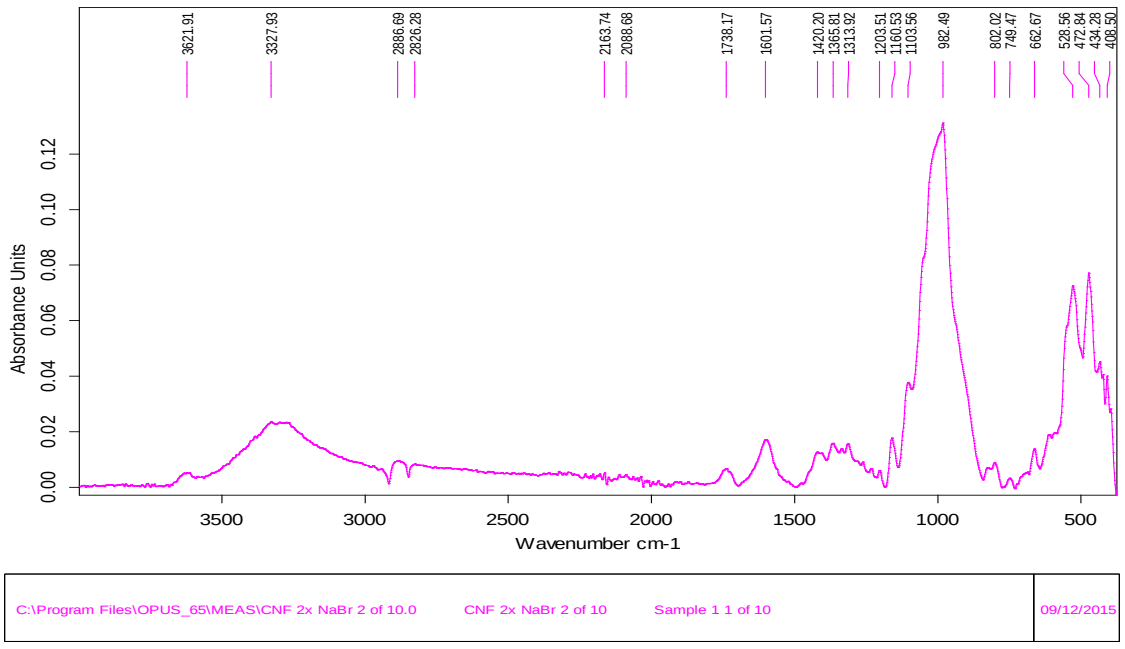


Figure B.5: FTIR of doubled NaBr concentration

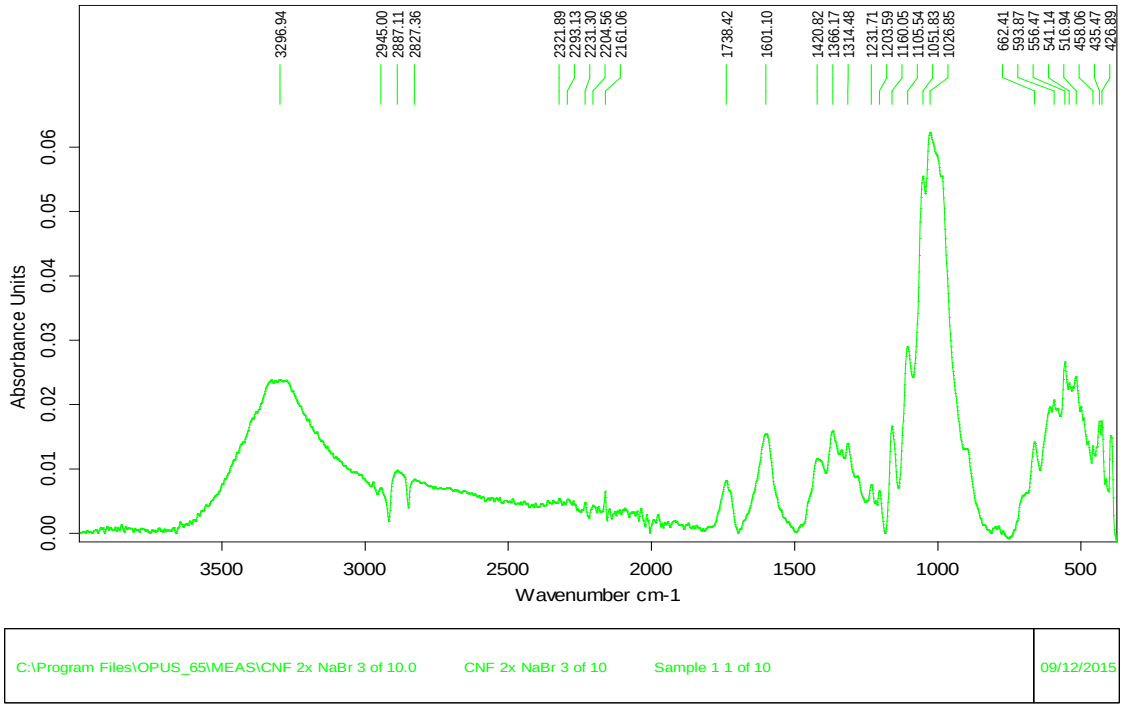


Figure B.6: FTIR of doubled NaBr concentration

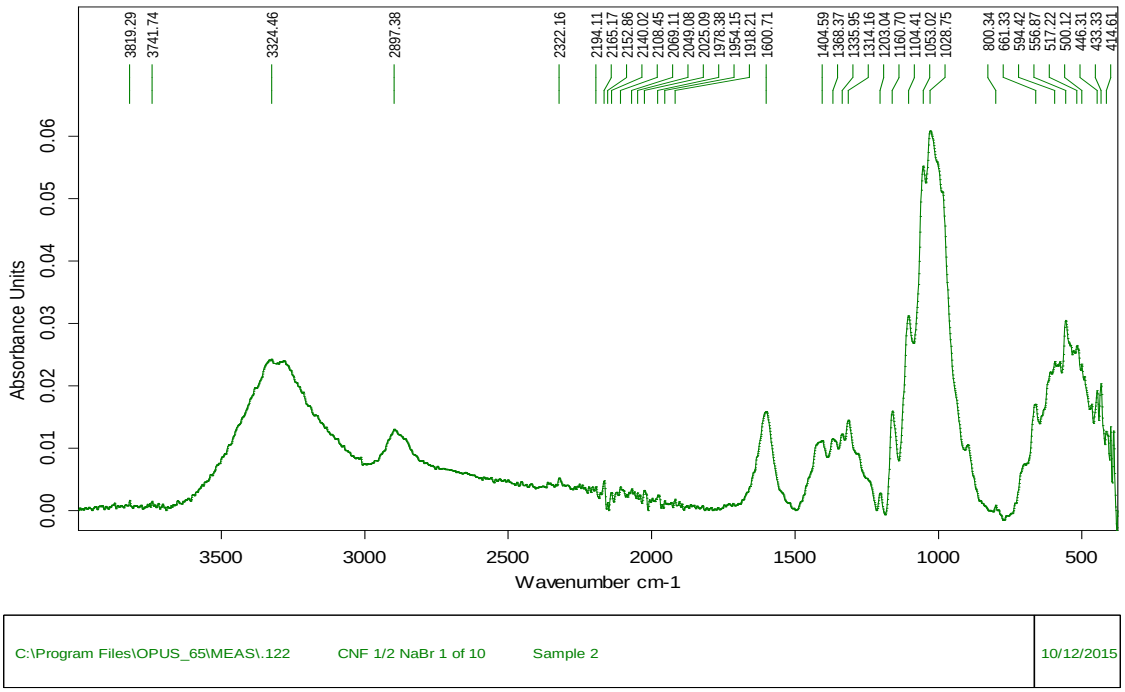


Figure B.7: FTIR Spectra of halved NaBr concentration:

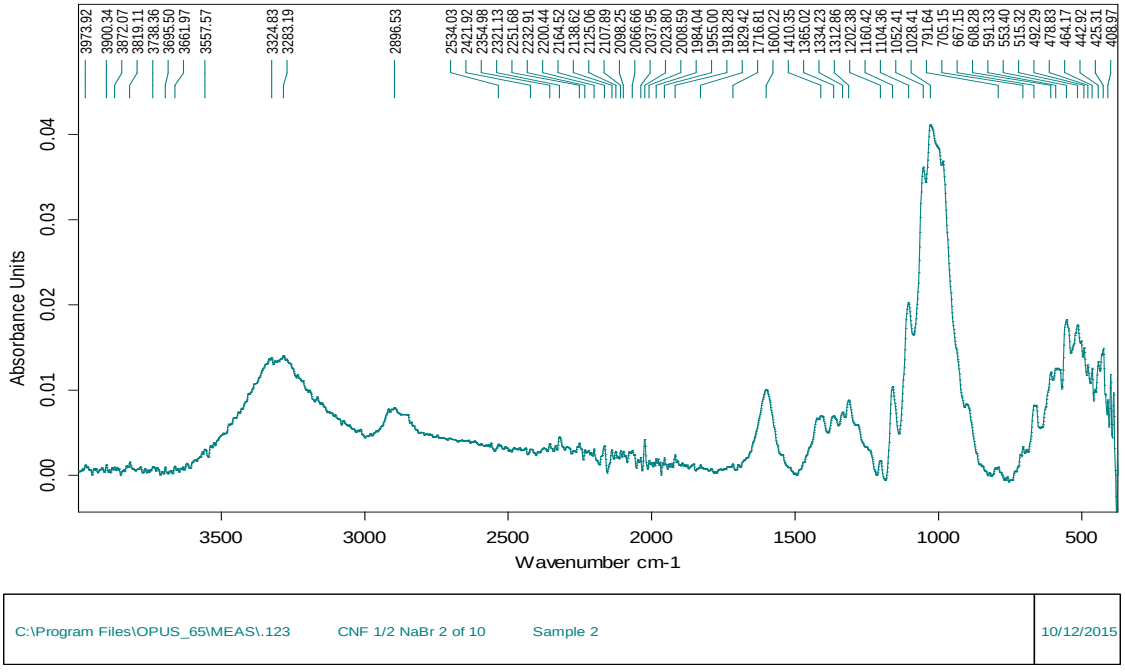


Figure B.8: FTIR Spectra of halved NaBr concentration

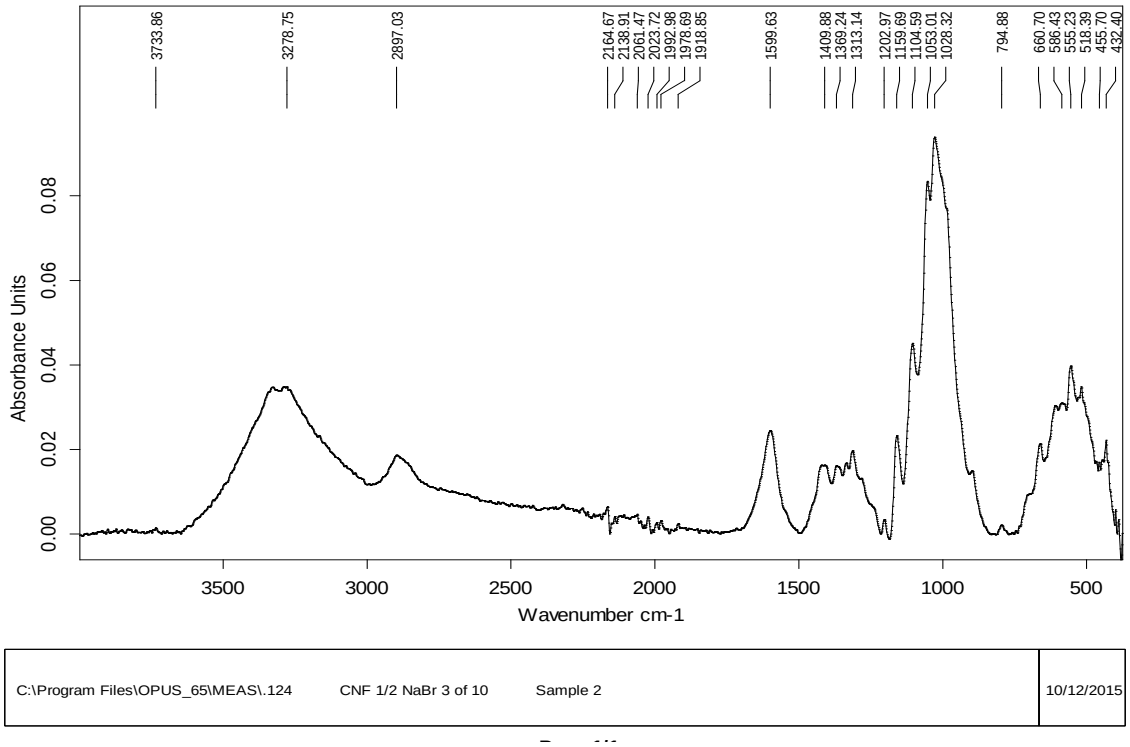


Figure B.9: FTIR Spectra of halved NaBr concentration

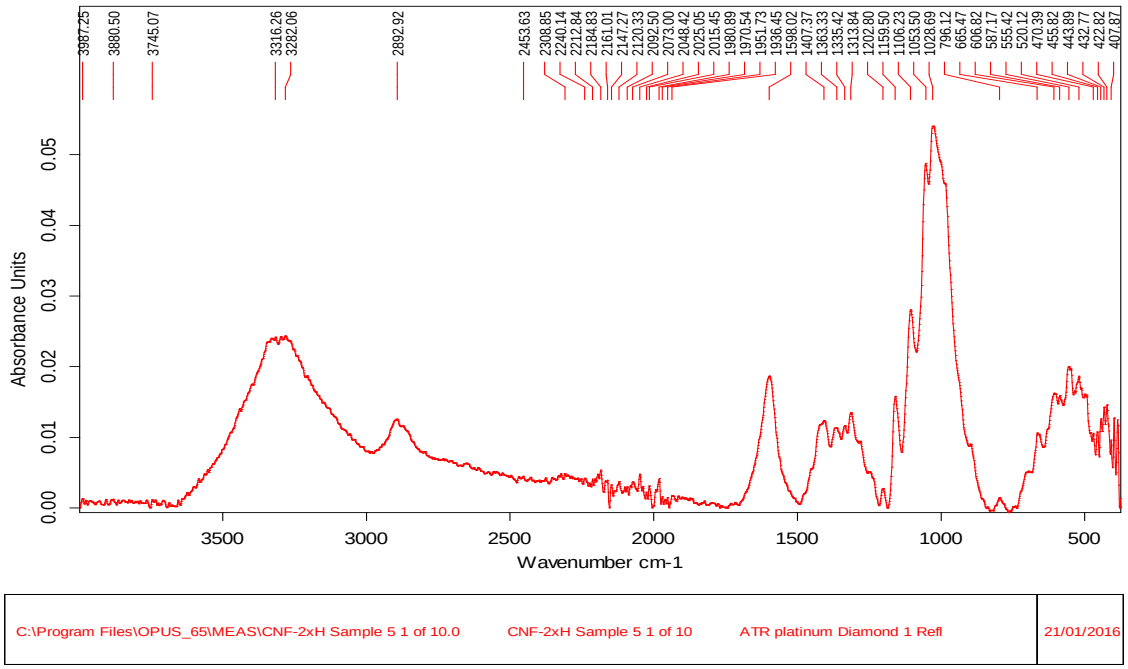


Figure B.10: FTIR of doubled NaOCl concentration

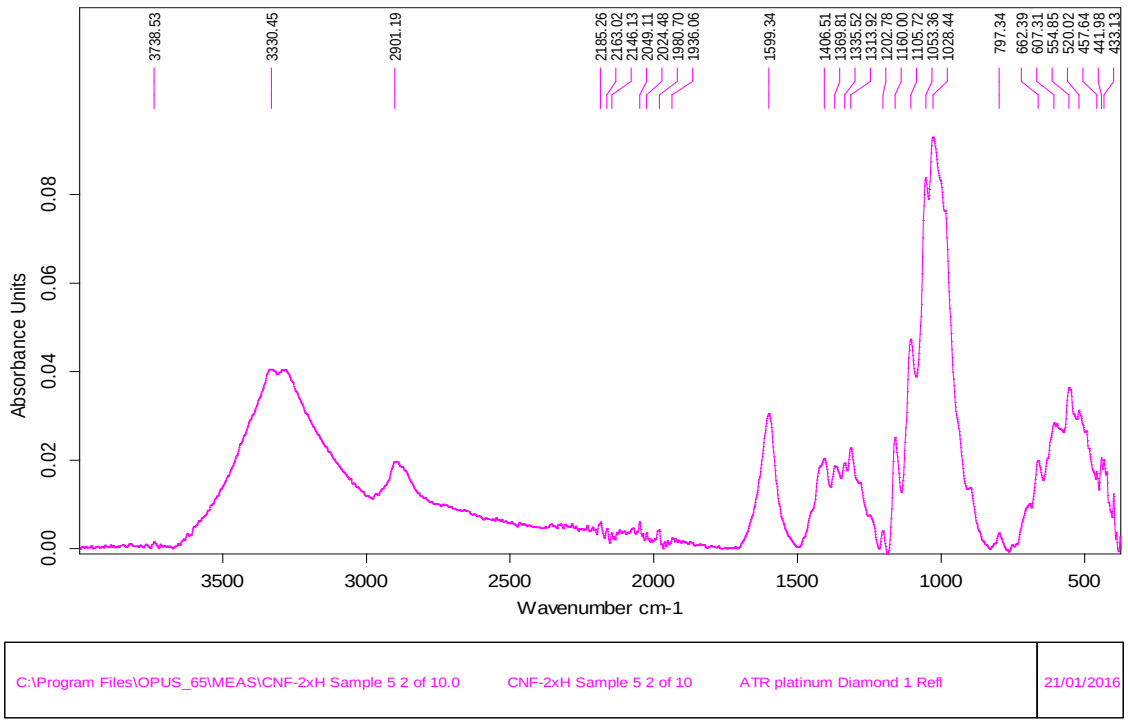


Figure B.11: FTIR of doubled NaOCl concentration

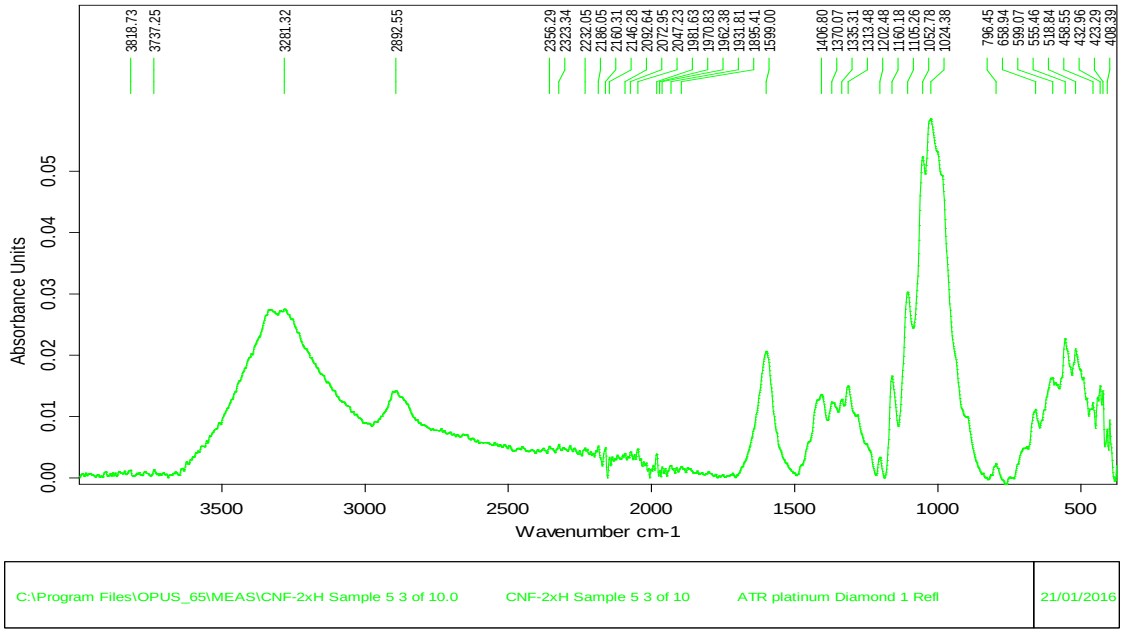


Figure B.12: FTIR of doubled NaOCl concentration

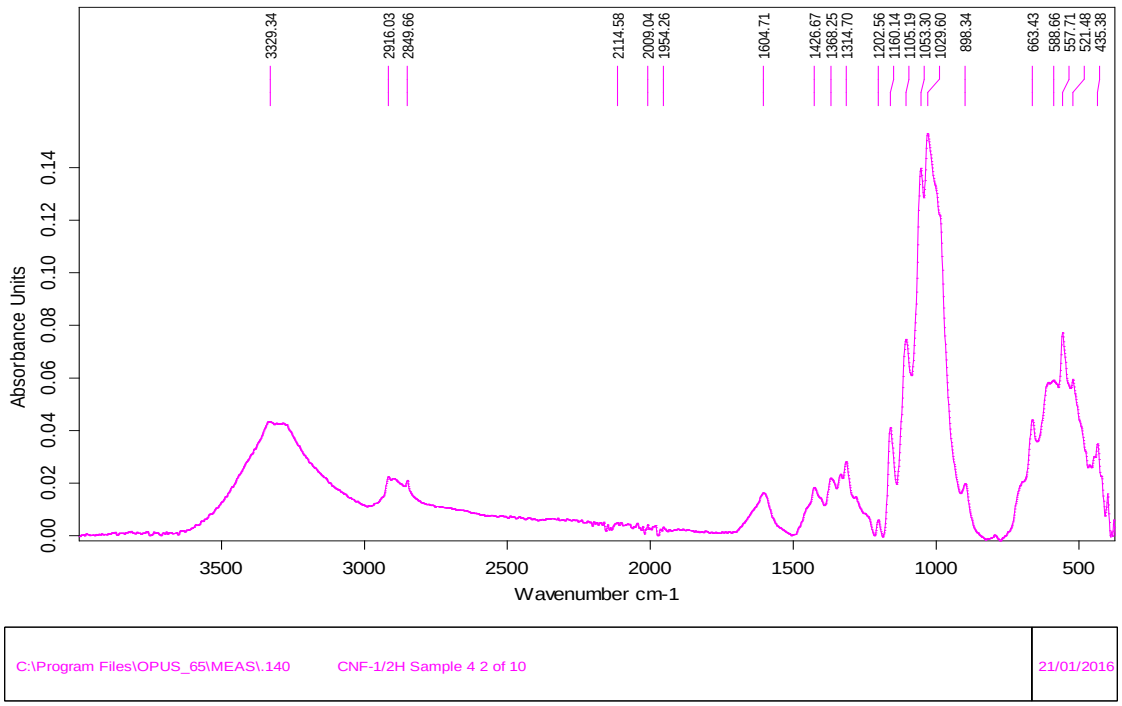


Figure B.13: FTIR Spectra of halved of NaOCl concentration

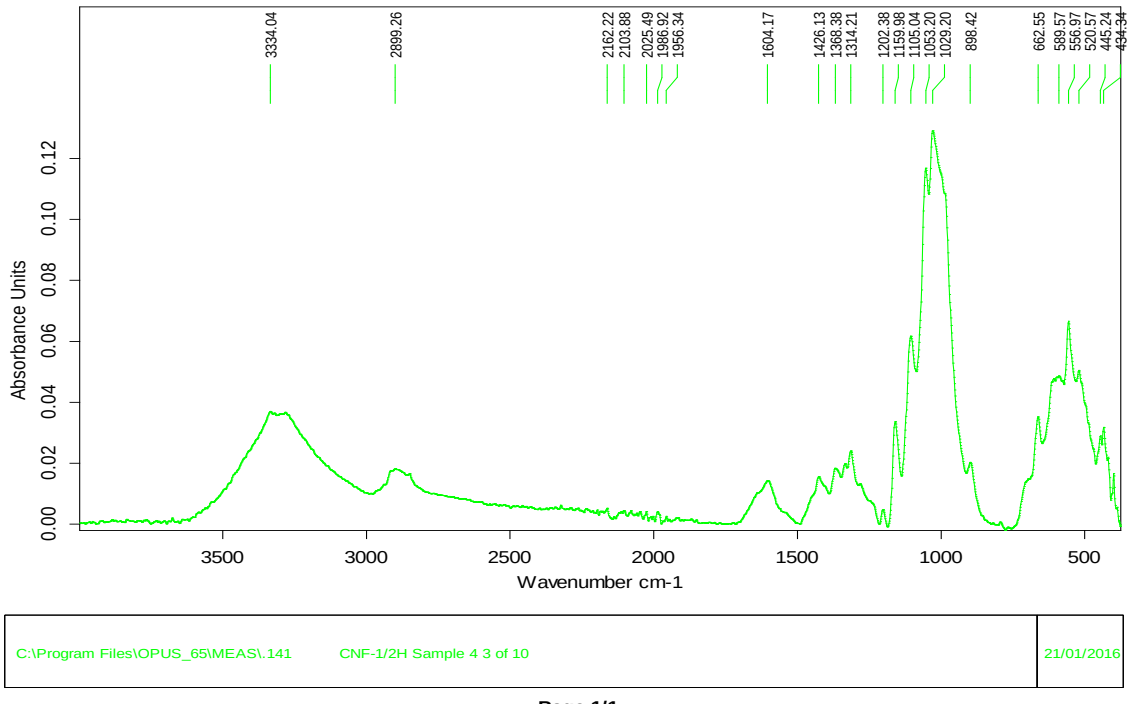


Figure B.14: FTIR Spectra of halved of NaOCl concentration

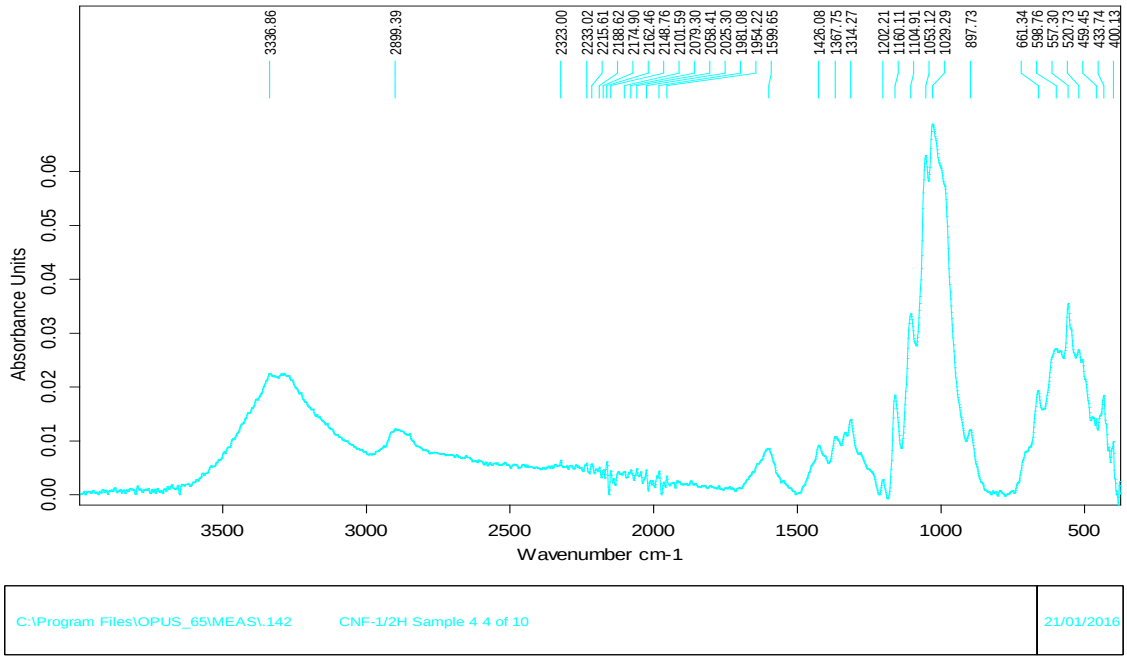


Figure B.15: FTIR Spectra of halved of NaOCl concentration

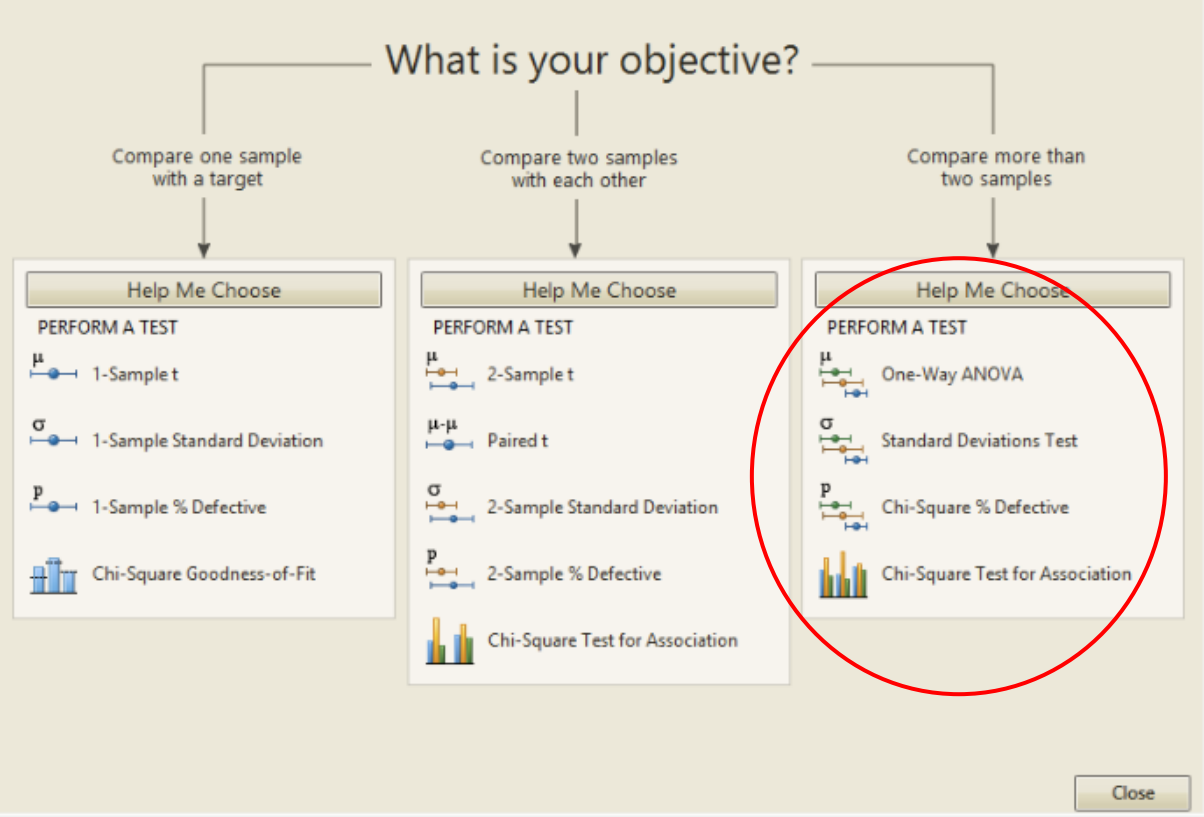


Figure B.16: Minitab Statistical Objective

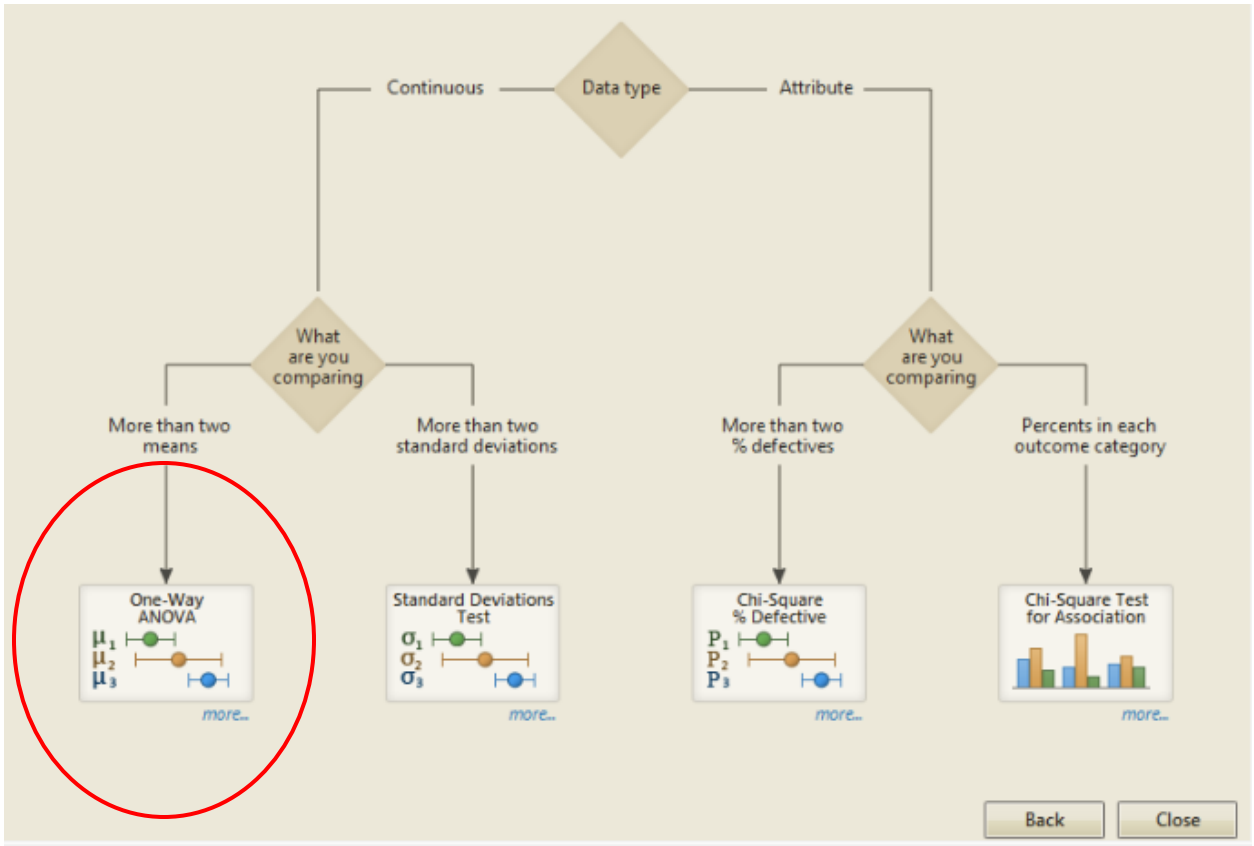


Figure B.17: Minitab Statistical Test One-Way ANOVA

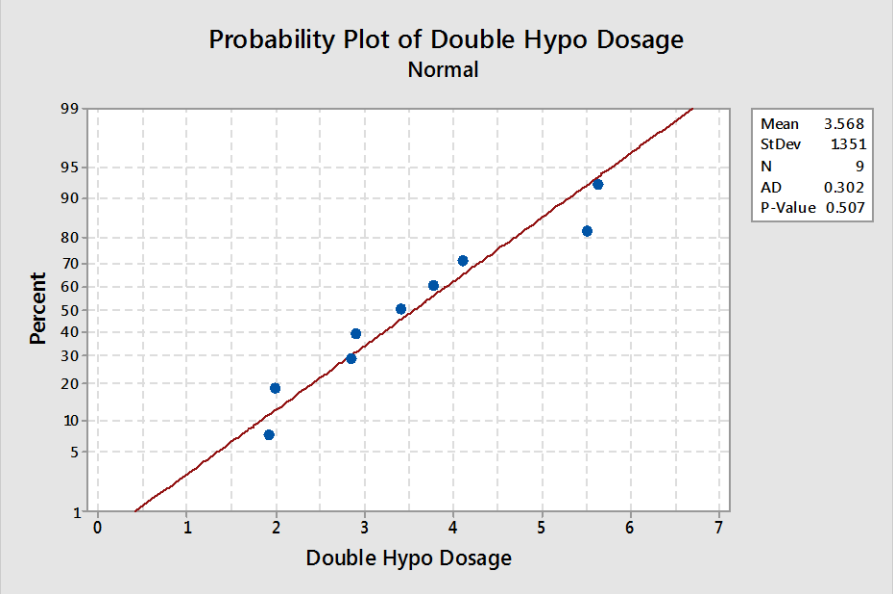


Figure B.18: Normality test for doubled NaOCl concentration

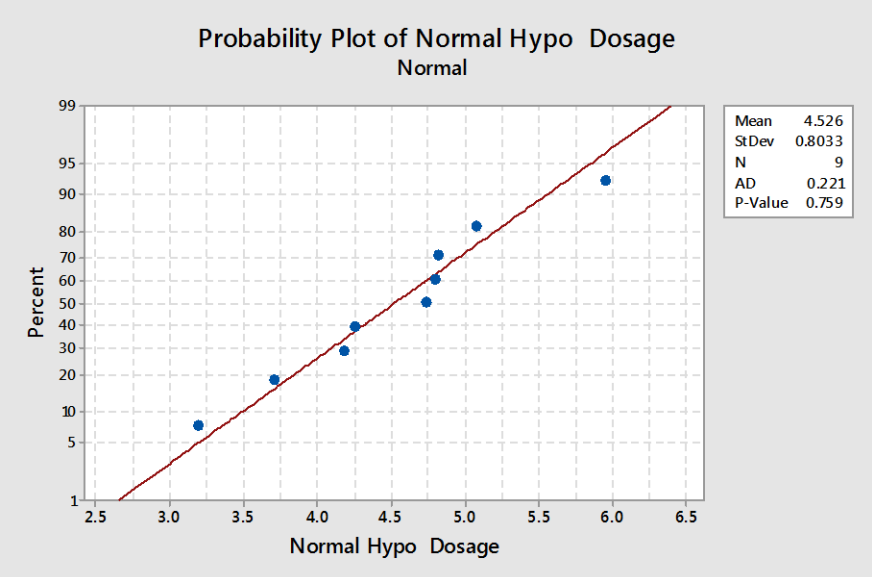


Figure B.19: Normality test for normal NaOCl concentration

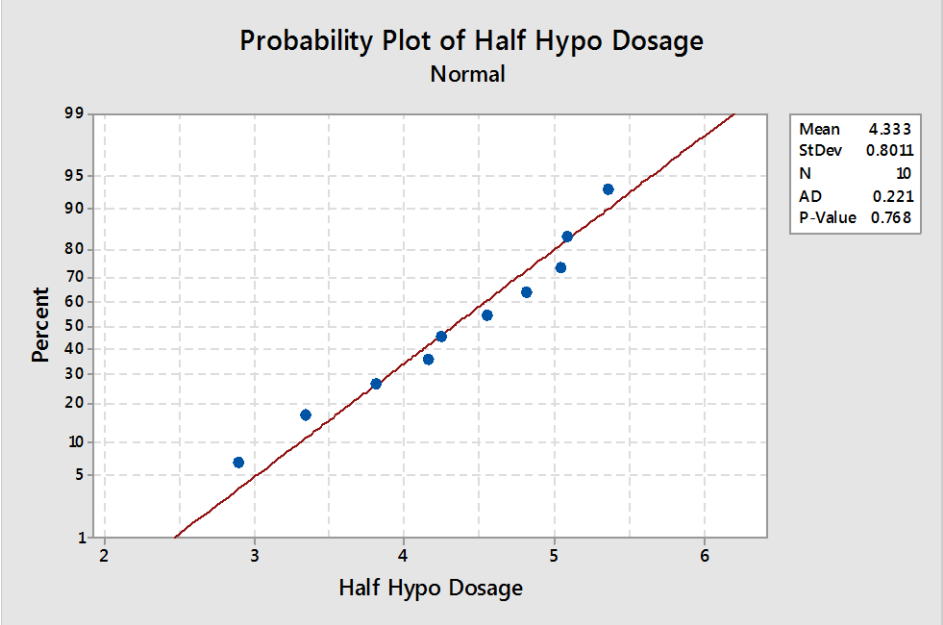


Figure B.20: Normality test for halved NaOCl concentration

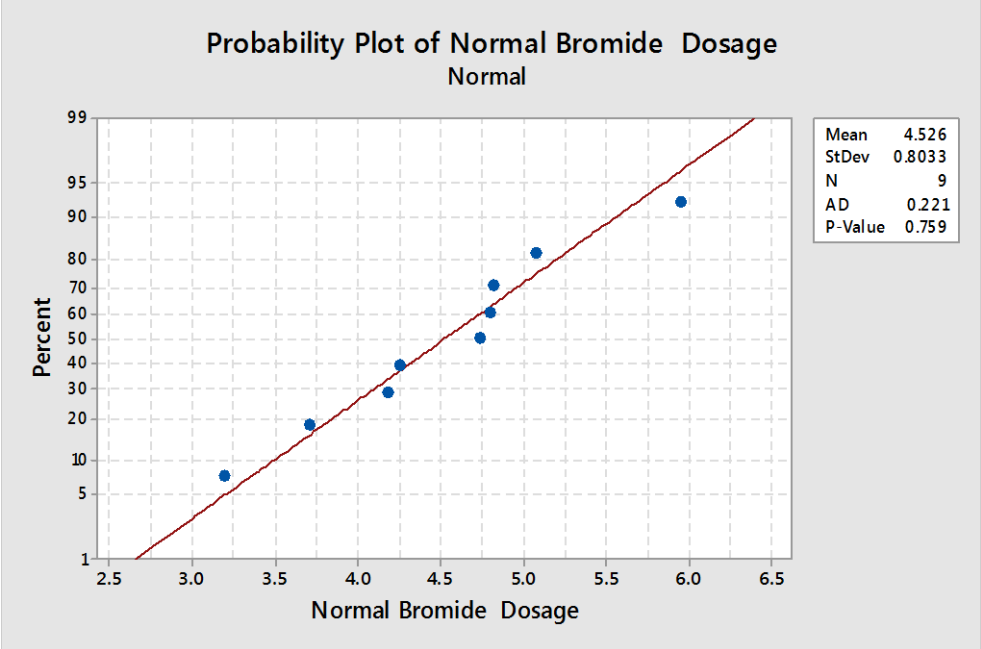


Figure B.21: Normality test for normal NaBr concentration

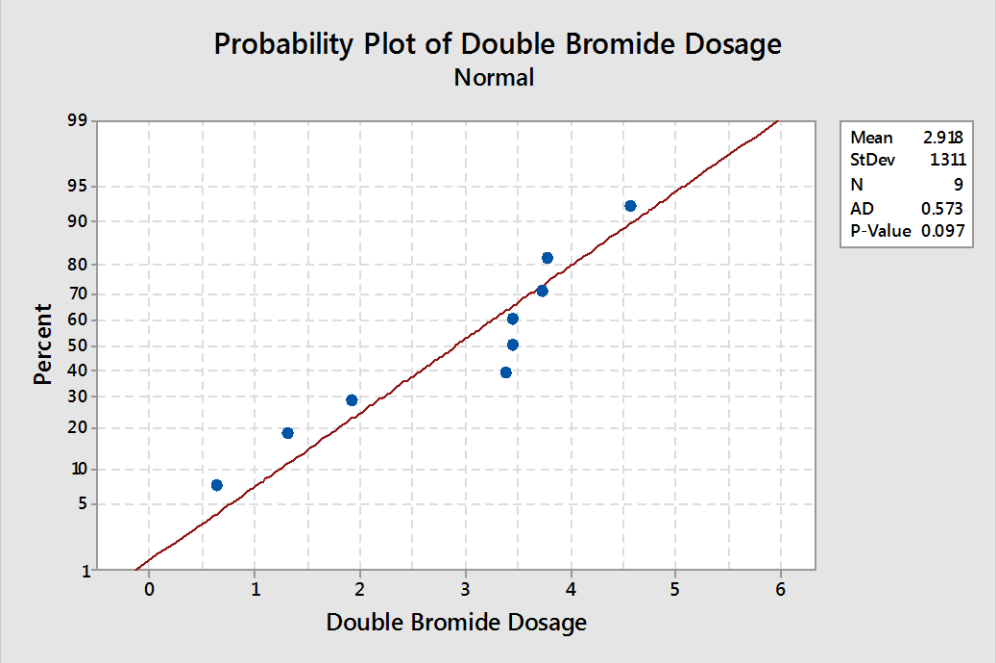


Figure B.22: Normality test for doubled NaBr concentration

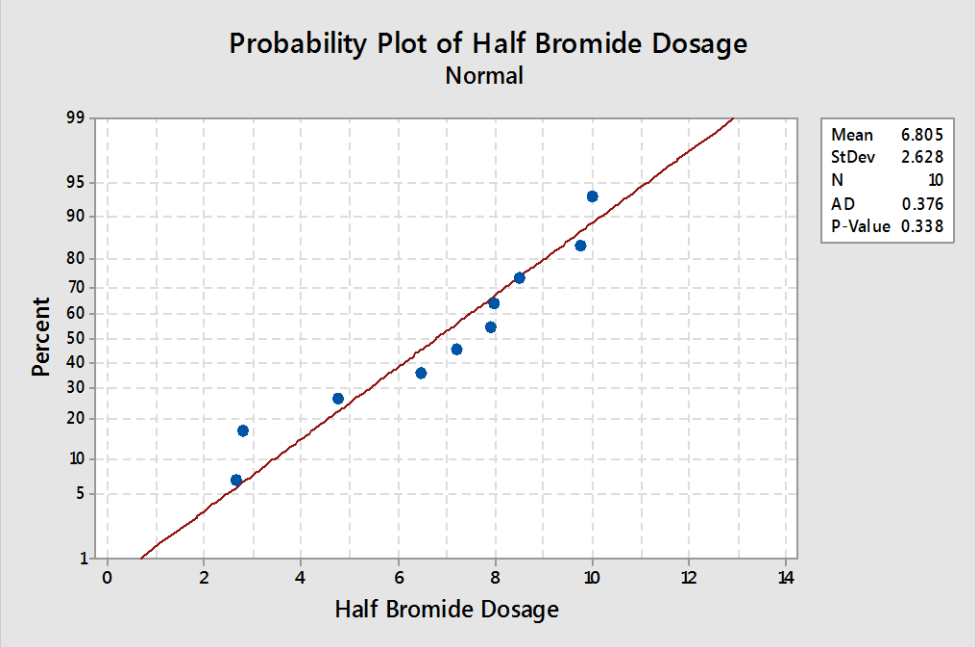


Figure B.23: Normality test for halved NaBr concentration

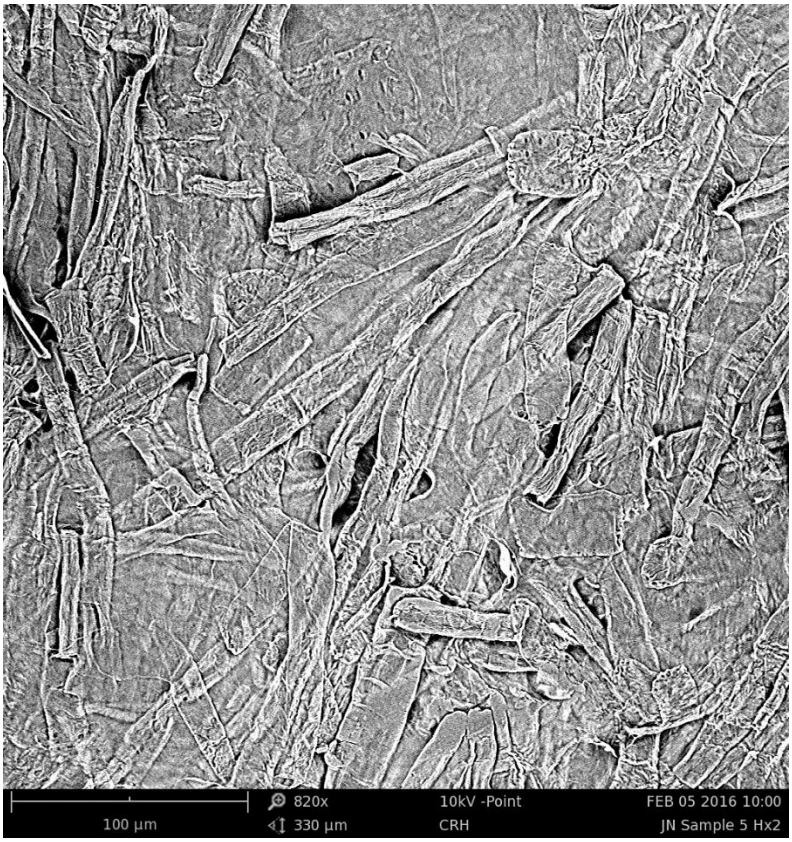


Figure B.24: SEM image of doubled NaOCl resolution 820x

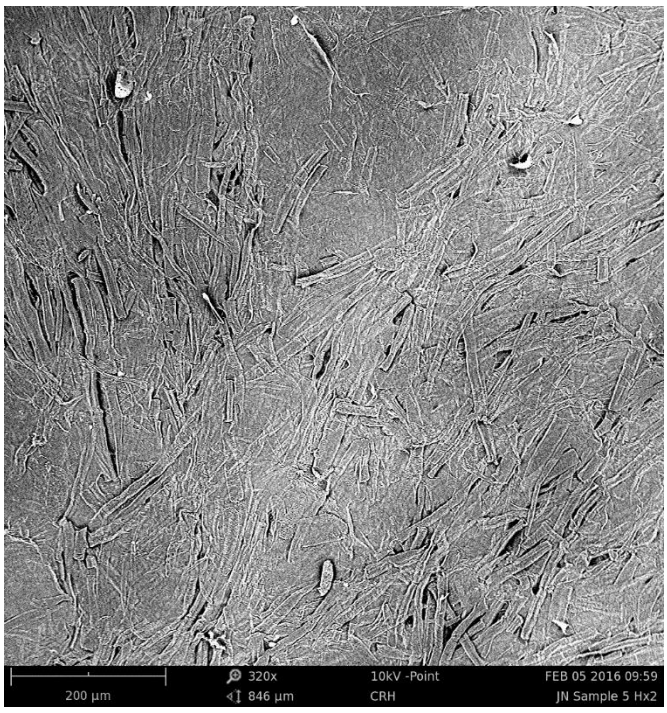


Figure B.25: SEM image of doubled NaOCl resolution 320x

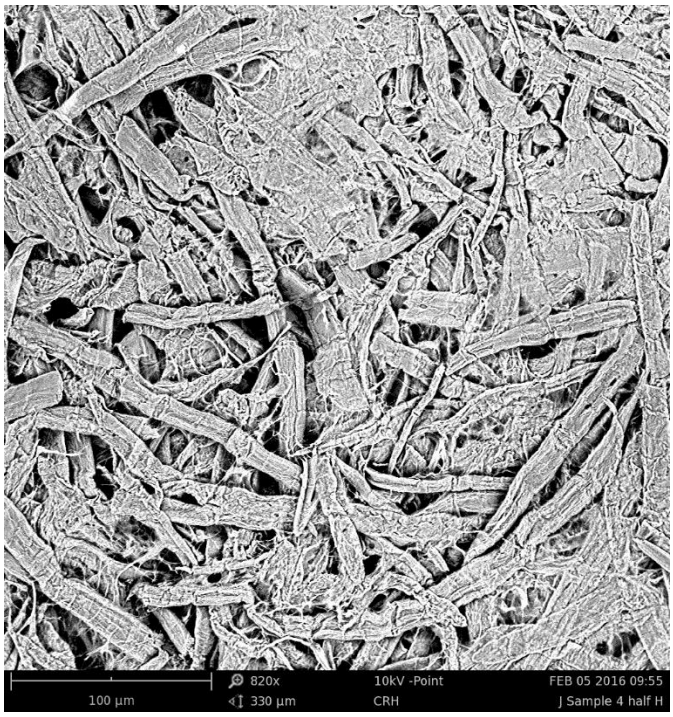


Figure B.26: SEM image of halved NaOCl resolution 820x



Figure B.27: SEM image of halved NaOCl resolution 265x



Figure B.28: SEM image of doubled NaBr resolution 790x



Figure B.29: SEM image of doubled NaBr resolution 300x

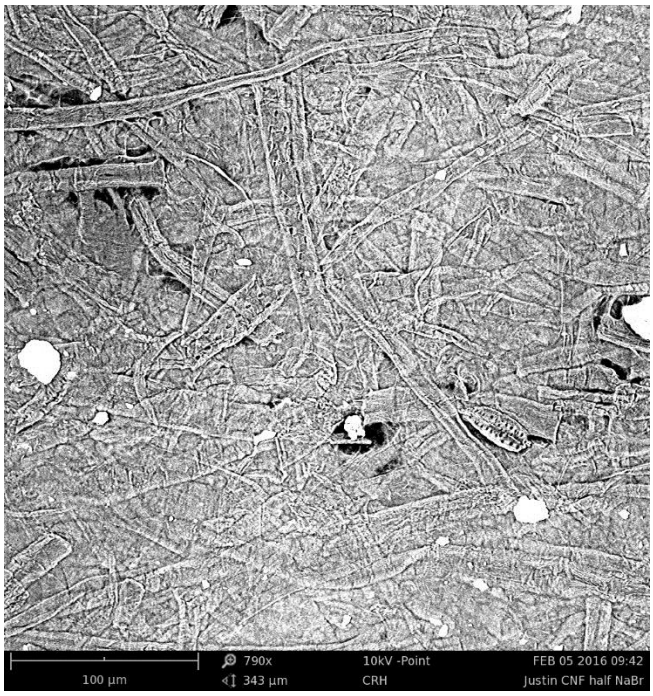


Figure B.30: SEM image of halved NaBr 790x

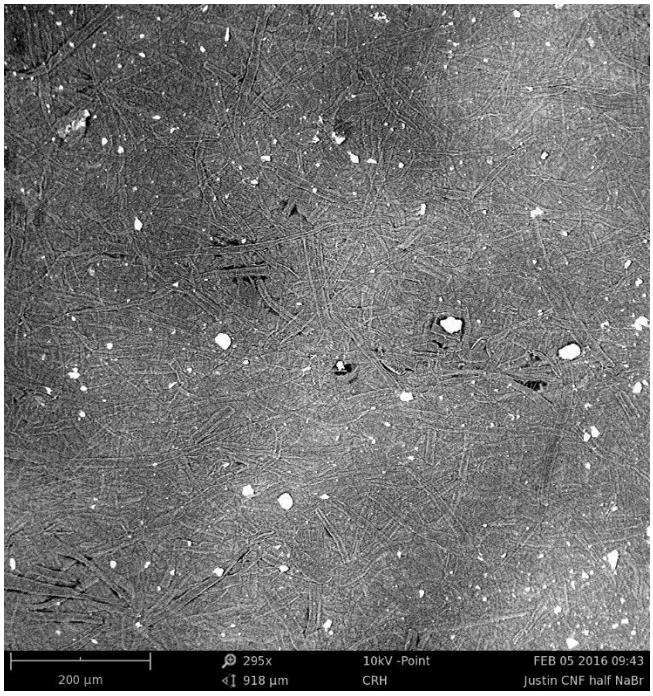


Figure B.31: SEM image of halved NaBr resolution 295x